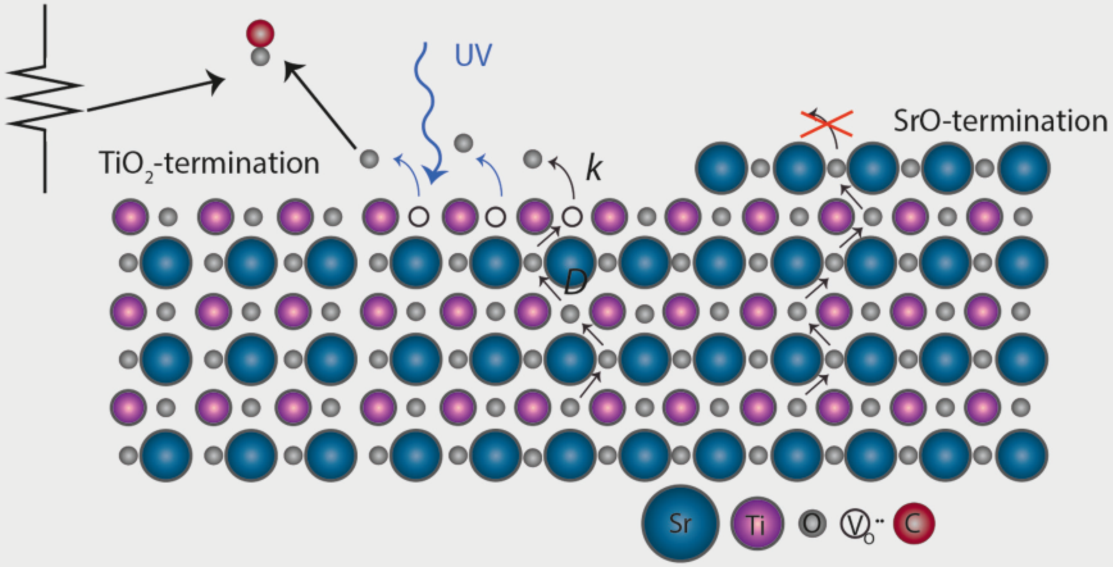

Defect engineering in oxide thin films

Felix V. E. Hensling

Information
Band / Volume 59
ISBN 978-3-95806-424-9

Mitglied der Helmholtz-Gemeinschaft

JÜLICH
Forschungszentrum

Schriften des Forschungszentrums Jülich
Reihe Information / Information Band / Volume 59

Forschungszentrum Jülich GmbH
Peter Grünberg Institut (PGI)
Elektronische Materialien (PGI-7)

Defect engineering in oxide thin films

Felix V. E. Hensling

Schriften des Forschungszentrums Jülich
Reihe Information / Information Band / Volume 59

ISSN 1866-1777 ISBN 978-3-95806-424-9

Bibliografische Information der Deutschen Nationalbibliothek.
Die Deutsche Nationalbibliothek verzeichnet diese Publikation in der
Deutschen Nationalbibliografie; detaillierte Bibliografische Daten
sind im Internet über http://dnb.d-nb.de abrufbar.

Herausgeber und Vertrieb:
Forschungszentrum Jülich GmbH
Zentralbibliothek, Verlag
52425 Jülich
Tel.: +49 2461 61-5368
Fax: +49 2461 61-6103
zb-publikation@fz-juelich.de
www.fz-juelich.de/zb

Umschlaggestaltung: Grafische Medien, Forschungszentrum Jülich GmbH

Druck: Grafische Medien, Forschungszentrum Jülich GmbH

Schriften des Forschungszentrums Jülich
Reihe Information / Information, Band / Volume 59

D 82 (Diss. RWTH Aachen University, 2019)

ISSN 1866-1777
ISBN 978-3-95806-424-9

Vollständig frei verfügbar über das Publikationsportal des Forschungszentrums Jülich (JuSER)
unter www.fz-juelich.de/zb/openaccess.

I dedicate this work to my precious son Tristan and my beautiful wife Alina

Abstract

Transition metal oxides constitute one of the most interesting material classes due to their wide variety of interesting and unusual properties. Often these properties are closely related to their defect structure. Within the transition metal oxide community $SrTiO_3$ is often referred to as a model material due to its well known defect chemistry. Therefore, in this work the possibilities of defect engineering are considered for this model material and the resulting properties are utilized for a highly interesting application: Resistive switching of $SrTiO_3$ in a metal insulator metal structure, a field of research where defects are key for the basic operation principle. The interest in transition metal oxides has been accompanied by an increased use of pulsed laser deposition, since it is a powerful and versatile method to achieve epitaxial complex metal oxide thin films.

Usually pulsed laser deposition is performed in ultra-high vacuum systems with the substrate being heated. Often oxygen is applied for the process as a method to compensate possible oxygen loss. The pressure applied in this manner is referred to as oxygen pressure, not considering the influence of residual gases. This thesis presents evidence that this pressure in reality does not correspond to the oxygen partial pressure. The ionization based measurement devices applied to the vacuum chamber can shift the equilibrium of the residual gases, which, for low pressure, cannot be neglected. The result is a markedly lower oxygen partial pressures than the applied oxygen pressure suggests, resulting in an increased oxygen vacancy formation. Within this thesis further a method to inhibit the formation of oxygen vacancies in the considered temperature and pressure regimes is presented. It is found that the formation of oxygen vacancies in $SrTiO_3$ is dependent on its termination. As the termination of $SrTiO_3$ can easily be controlled, this constitutes a practical possibility to engineer the oxygen vacancy formation.

Pulsed laser deposition itself is a non-equilibrium growth technique, thus deviations from the equilibrium defect concentration and types are expected. An influence on this non-equilibrium process that was up to now not considered is the radiation resulting from the plasma plume. In this work it is shown that the plasma plume present during $SrTiO_3$ depositions emits UV-radiation, which in turn enhances the oxygen vacancy formation. Besides this, a the possibility to control the cation stoichiometry of the film by a change of the laser fluence is investigated. This method

is employed to modify the Sr/Ti-ratio and a Sr-surplus is identified to be highly advantageous for the switching performance of $SrTiO_3$ devices. Two main accommodation mechanisms for Sr-excess are identified, namely Ruddlesden-Popper-type anti phase boundaries and SrO surface segregation. This work presents methods to engineer both defect scenarios in nominally stoichiometric thin films. Ruddlesden-Popper-type anti phase boundaries can be achieved by the stabilization of additional SrO on the substrate surface, which acts as a seed for their formation. SrO surface segregation can be achieved by depositing additional SrO on top of the thin film.

These defect engineered thin films are subsequently investigated with respect to their switching properties. It is found that Ruddlesden-Popper-type anti phase boundaries in $SrTiO_3$ result in forming free switching, a highly desirable property for resistive switching devices. Additional SrO on top of the film is shown to form $SrCO_3$, which in turn is a main influence factor on all resistive switching properties. Its heat confinement is shown to determine the memory window and the variability; its high diffusion barrier for oxygen is shown to determine the memory's time stability and the forming step.

Summarizing, this works elucidates the sources of defect formation for the model material $SrTiO_3$, shows methods to control the formation of these defects and explains their role for the properties of the material. The presented results in principle apply to other resistive switching oxides in the same fashion and provide a guideline on how to improve the device performance by defect engineering.

Kurzfassung

Auf Grund ihrer ungewöhnlichen und interessanten Eigenschaften, die oftmals in engem Zusammenhang mit ihrer Defektstruktur stehen, ist die Erforschung von Übergangsmetalloxiden von höchstem Interesse. Innerhalb der Übergangsmetalloxide gilt $SrTiO_3$ gemeinhin als Modellmaterial, da es den Vorteil einer wohlbekannten Defektchemie besitzt. Daher wird im Zuge dieser Arbeit das Maßschneidern von Defekten anhand dieses Materials untersucht und angewendet. Eine geeignete Anwendung für diese Untersuchungen findet sich im resistiven Schalten von $SrTiO_3$; ein Prozess der maßgeblich abhängig von der Defektstruktur der Dünnschicht ist. Das wissenschaftliche Interesse an Übergangsmetalloxiden geht einher mit einer gesteigerten Beachtung der gepulsten Laserdeposition, da diese Methode die Abscheidung komplexer epitaktischer oxider Dünnschichten ermöglicht.

Gepulste Laserdeposition findet in der Regel in Ultrahochvakuumsystemen statt. Hierbei wird das Substrat geheizt und oftmals Sauerstoff eingelassen, um einen etwaigen Verlust auszugleichen. Der so eingestellte Druck wird gemeinhin als Sauerstoffdruck bezeichnet, ohne dabei jedoch den Einfluss der Restgase zu berücksichtigen. Im Verlaufe dieser Arbeit stellt sich jedoch heraus, dass es sich hierbei nicht um den realen Sauerstoffpartialdruck handelt. Messgeräte, die an der Kammer angeschlossen sind und auf Ionisationsprozessen beruhen, können vielmehr das Gleichgewicht der bei niedrigen Drücken nicht vernachlässigbaren Restgase beeinflussen. Auf diese Weise wird der effektive Sauerstoffpartialdruck vermindert, was letztendlich zu einem vermehrten Einbau von Sauerstoffleerstellen führt. Darüber hinaus wird in dieser Arbeit eine Möglichkeit präsentiert den Einbau von Sauerstoffleerstellen in den betrachteten Druck- und Temperaturbereichen zu unterdrücken. Das Ergebnis, dass der Einbau von Sauerstoffleerstellen in $SrTiO_3$ terminierungsabhängig ist, ermöglicht ein Maßschneidern des Sauerstoffleerstelleneinbaus, da die Terminierung präzise einstellbar ist.

Da es sich bei der gepulsten Laserdeposition um eine Wachstumsmethode handelt, die nicht im thermodynamischen Gleichgewicht stattfindet, erwartet man grundsätzlich, dass die Defektdichte und -typen vom Gleichgewicht abweichen. Ein Einfluss auf dieses Ungleichgewicht, der bis dato keine Beachtung gefunden hat, ist die Strahlung des Plasmaplumes. In dieser Arbeit wird gezeigt, dass das Abscheiden

von $SrTiO_3$ UV-Strahlung mit sich bringt, die wiederum den Einbau von Sauerstoffleerstellen beschleunigt. Des Weiteren wird die Möglichkeit der Kationenstöchiometrieeinstellung anhand der Energiedichte des Lasers genützt, um das Sr/Ti-Verhältnis einzustellen. Es stellt sich heraus, dass Schichten mit einem Sr-Überschuss hervorragende Schalt-eigenschaften aufweisen und dass dieser Sr-Überschuss hauptsächlich durch zwei Mechanismen ausgeglichen wird: das Bilden von Ruddlesden-Popper-artigen Antiphasengrenzen und die Segregation von SrO an die Oberfläche. In dieser Arbeit werden Möglichkeiten präsentiert, um beide Defekte in nominell stöchiometrischen Schichten nachzuahmen. Ruddlesden-Popper-artige Antiphasengrenzen können mit Hilfe der Abscheidung sowie Stabilisierung von SrO an der Substratoberfläche eingebracht werden. Die Segregation von SrO kann durch das Abscheiden zusätzlichen SrOs auf der Dünnschichtoberfläche nachgeahmt werden.

Schichten mit auf diese Weise eingebrachten Defekten wurden anschließend bezüglich ihrer Schalteigenschaften untersucht. Es stellt sich heraus, dass Ruddlesden-Popper-artige Antiphasengrenzen zu formierfreiem Schalten führen, eine Eigenschaft, die als äußerst erstrebenswert für resistives Schalten gilt. Weiterhin wird gezeigt, dass SrO auf der Filmoberfläche zu $SrCO_3$ reagiert, welches wiederum einen Haupteinflussfaktor auf die Schalteigenschaften darstellt. Seine Eigenschaft als schlechter Wärmeleiter legen das Speicherfenster sowie die Variabilität fest, außerdem führt seine hohe Sauerstoffdiffusionsbarriere zu einer besseren Langzeitstabilität und einem ausgeprägtem Formierschritt.

Insgesamt klärt diese Arbeit den Ursprung von Defekten im Modellmaterial $SrTiO_3$ auf, zeigt Möglichkeiten auf, diese Defekte zu kontrollieren und erklärt den Einfluss dieser Defekte auf die Eigenschaften des Materials. Grundsätzlich lassen sich die hier präsentierten Ergebnisse auf andere resistiv schaltende Oxide übertragen und stellen daher einen vielversprechenden Weg zur Verbesserung der Schalteigenschaften mittels Defektmaßschneiderns dar.

Contents

1 Introduction

Over the last decade the field of transition metal oxides has received extensive attention from research. This is due to their manifold interesting and unusual properties, which are connected to their outer *d*-electrons. This especially results in noteworthy electronic and magnetic properties. Their electronic properties reach from metallic conducting e.g. $LaNiO_3$ to highly insulating e.g. $LaAlO_3$. Their magnetic properties reach from ferromagnetic e.g. $La_{0.5}Sr_{0.5}MnO_3$ to antiferromagnetic e.g. $LaCrO_3$. Other related interesting properties include the formation of a two dimensional electron gas in heterostructures, e.g. at the $LaAlO_3/SrTiO_3$ interface, superconductivity, e.g. $LaCuO_3$, or ferroelasticity, e.g. $Gd_2(MoO_4)_3$.[1] The increased interest in transition metal oxides has been accompanied by an increased use of pulsed laser deposition (PLD), since PLD is a powerful and versatile method to achieve epitaxial complex metal oxide thin films.[2–4]

The properties of these oxide thin films are highly dependent on their defect structure. Examples are the oxygen vacancy induced conduction[5–8] and the suppression of donor doping by cation vacancies[9–16]. In order to achieve high quality epitaxially oxide thin films one usually uses single crystal substrates with a similar crystal structure. The defects of the substrate can equally influence the properties of the resulting material system. These defects can e.g. be induced during annealing or growth. PLD, in particular since it is a non-equilibrium process, generally results in material systems with defect densities strongly differing from the expected equilibrium.[17] The conductivity of the system can for example be dominated by the substrate, if a significant amount of oxygen vacancies is generated during growth.[18–20]

$SrTiO_3$ is considered as a model material for perovskite transition metal oxides as it offers the advantage of a well known chemical equilibrium defect chemistry and is frequently used as a substrate. Nevertheless, prior to this work a contradiction existed in literature with regard to the oxygen pressure necessary to reduce $SrTiO_3$. While chemical equilibrium experiments suggested an oxygen pressure of $p_{O_x} \leq 10^{-17}$ mbar,[5, 6, 8, 21] physical annealing experiments suggested an oxygen pressure of $p_{O_x} \lesssim 10^{-7}$ mbar.[22–24] In this work the source of this marked ten orders of magnitude difference in reported p_{O_x} will, besides other influences on the formation of oxygen vacancies during growth and annealing, be unrevealed.

The parasitic influence of oxygen vacancies in $SrTiO_3$ will be considered more closely for $LaAlO_3/SrTiO_3$ heterostructures. Since its discovery by Ohtomo *et al.*[25] the two dimensional electron gas (2DEG) at the interface between the two otherwise insulating materials $LaAlO_3$ and $SrTiO_3$ has drawn a lot of attention. Due to the outstanding properties of the 2DEG, e.g. a controllable electron density, its possible applications include, but are not limited to an all-oxide field effect transistor.[26–33] In the scope of this work the interest in $LaAlO_3/SrTiO_3$ is based on its sensitivity to oxygen vacancies. Two different conduction mechanisms can be distinguished for $LaAlO_3/SrTiO_3$ based on the drastically different resulting carrier densities, bulk conductivity and interface conductivity. While interface conductivity is based on the evasion of a polar catastrophe[34], bulk conductivity is only observed, if significant oxygen vacancies are present in the $SrTiO_3$ substrate[35]. This makes $LaAlO_3/SrTiO_3$ an outstanding candidate to identify and understand the role of oxygen vacancies.

One of the most exciting field where defects are even crucial for the underlying working principle is the field of resistive switching. The interest in resistive switching is a result of the ever continuing search for faster, smaller and more energy efficient non-volatile memory devices. It has shifted into the focus of industry and research as it additionally allows multi-bit operation, logic-in-memory applications, and neuromorphic computing architectures.[36–41] It has been shown for a wide range of resistive switching materials that the defects present in the insulating thin film play a crucial role for the resulting switching behavior.[42–47] However the commonly used binary oxides in a polycrystalline or amorphous form make it impossible to understand the details of the impacts of defects on the device performance. Using epitaxial $SrTiO_3$ metal-insulator-metal (MIM) structures in this work it will be shown that it is possible to single out defect types and consequently link them to specific switching properties. Previous results of this group have shown that epitaxial $SrTiO_3$ MIMs are highly sensitive to deviations from the perfect cation stoichiometry.[48] A focus of this work will be to identify the defects resulting from a deviation from the perfect cation stoichiometry and to investigate their influences on the switching properties.

Chapter 2 will describe the background of this work in more detail and in chapter 3 the experimental details will be presented.

In chapter 4 different influences on the defect structure of $SrTiO_3$ will be investigated. First influences on the formation of oxygen vacancies will be considered. Besides the known equilibrium influences like pressure and temperature,[5–7] additional influences during mere thermal annealing are revealed, such as the role of contaminations and measurement devices. Furthermore influences during PLD are considered, in particular the influence of the UV-radiation of the plasma plume. While both of these influences are based on the process, finally an influence on the oxygen vacancy formation based on the substrate is presented, namely it is demonstrated that termination control allows for a tailoring of the formation of oxygen vacancies. The role of oxygen vacancy formation in $SrTiO_3$ will be demonstrated by the use of $LaAlO_3/SrTiO_3$ heterostructures.

In the second part of chapter 4 the possibility of influencing the cation stoichiometry of $SrTiO_3$ thin films during PLD by a change of the laser fluence will be elaborated. By changing the cation stoichiometry one does also change the defect type and concentration of the resulting $SrTiO_3$ thin film. Considering the following chapters a main emphasis will be on the defects resulting from an accommodation of Sr-excess, i.e. SrO islands and Ruddlesden-Popper type anti phase boundaries.

Chapter 5 will provide insights on the role of these defects for resistive switching of $SrTiO_3$ MIMs. This calls for the development of a method to engineer said defects, which is also presented in this chapter. Being able to engineer both, Ruddlesden-Popper type anti phase boundaries and SrO islands, allows us to distinguish their influences on the switching properties of $SrTiO_3$ devices, eventually allowing to derive design rules for devices based on the impact of specific defects.

As chapter 5 will prove a marked influence of SrO at the $SrTiO_3$/Pt interface for resistive switching, chapter 6 will intensify the investigations of this interface. The supposed SrO islands are identified to in fact form $SrCO_3$. In this context carbon will be presented as a central influence parameter. Different scenarios for the influence of carbon will be considered and its role as a lateral heat confinement layer will be identified as most probable. Based on this new gained knowledge a possibility to utilize the central role of carbon, namely introducing a carbon pattern, will be investigated.

Finally chapter 7 will summarize the results of the previous chapters and put them into an overall context. It will further give an outlook on possible future experiments.

2 Background

In the following $SrTiO_3$ will be introduced with regard to its crystal, defect and electronic structure. Further, the two applications considered in this work, namely $LaAlO_3/SrTiO_3$ heterostructures and resistive switching, will be introduced.

2.1 $SrTiO_3$

2.1.1 Crystal structure

At room temperature $SrTiO_3$ is a cubic ionic crystal perovskite in the Pm3m space group with a lattice constant of a = 0.39 nm. Figure 2.1 a) shows its structure, where Sr^{2+} is located on the A-site and Ti^{4+} on the B-site. The Ti^{4+} on the B-site forms a framework of TiO_6 octahedra and the Sr^{2+} on the A-site is anticuboctahedrally coordinated in the respective interstices.[49, 50] In the [001] direction this results in non-polar alternating layers of SrO and TiO_2. The surface of $SrTiO_3$ can thus exhibit a TiO_2-, a SrO- or a mixed termination.[51] Usually $SrTiO_3$, as delivered, exhibits a mixed termination with 5 to 25% SrO and 95 to 75% TiO_2, respectively.[51, 52]

2.1.2 Defect chemistry

The properties of all solid state materials are heavily influenced by their defect structure.[53] Defects in the $SrTiO_3$ crystallinity can, as for all other materials, be categorized by their dimension:

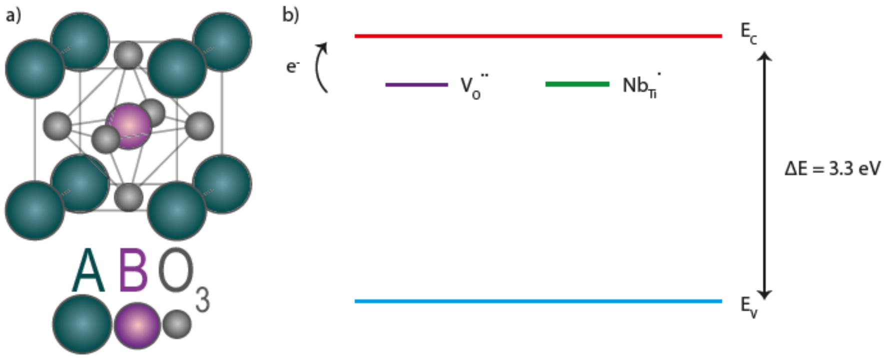

Figure 2.1: a) Structure of a perovskite, for $SrTiO_3$ the A-site is Sr^{2+} and the B-site Ti^{4+}, for $LaAlO_3$ the A-site is La^{3+} and the B-site Al^{3+}. b) Illustration of the electronic band structure of $SrTiO_3$ with a schematic portrayal of oxygen vacancy and Nb doping.

0D Vacancies and interstitials

Within this work the Kroeger-Vinck notation is used to describe point defects.[54] For the densely packed structure of $SrTiO_3$ the formation of interstitials can be excluded,[6] thus in the following only the role of vacancies will be discussed.

For $SrTiO_3$ two basic types of vacancies exist, oxygen vacancies ($V_O^{\bullet\bullet}$) and cationic vacancies. In case of thermodynamic equilibrium, the two main influence factors on these vacancies are, as given by the mass action law, temperature and oxygen pressure.[5–7] Generally these vacancies have to fulfill the charge neutrality law. In the case of $SrTiO_3$ this means, that $V_O^{\bullet\bullet}$, which, as indicated, are double positively charged with respect to the lattice, need to be compensated by either $2e^-$ or by cation vacancies, forming a Schottky pair. A Ti vacancy (V_{Ti}'''') is four times negatively charged with respect to the lattice and a Sr vacancy (V_{Sr}'') double positively charged. The cation vacancies can consequently be compensated either by the appropriate number of $V_O^{\bullet\bullet}$ or $h^\bullet$. The particular concentration of these defects and their compensation can be differentiated by temperature and oxygen pressure regime as will be discussed below.[55]

In order to adjust the thermodynamical equilibrium, the involved species need to be mobile. For $SrTiO_3$ this results in three different temperature regimes, where the low temperature regime is dominated by the immobility of all ionic species, the intermediate temperature regime is dominated by mobile anions and the high temperature regime by the mobility of all involved species.[55, 56]

As ionic species are largely immobile $\lesssim$ 750 K in SrTiO$_3$, the vacancy concentration is frozen and determined by the sample's history. This can be used to investigate frozen defect equilibria of higher temperatures at room temperature. For as received SrTiO$_3$ this implies acceptor doping, as impurities incorporated during manufacturing (typically Fe, Al, Mn) are omnipresent and negatively charged with respect to the lattice.[55] In this regime electron hole pairs can be generated by extrinsic influences like thermal excitation or irradiation.[57, 58] Further in this temperature regime ionization reactions are observable. Due to their low ionization energy barrier oxygen vacancies are e.g. usually double ionized donating two electrons:[6]

$$\mathrm{V_O^{x}} \rightleftharpoons \mathrm{V_O^{\bullet\bullet}} + 2\mathrm{e}^- \tag{2.1}$$

This is also the principle of extrinsic doping of SrTiO$_3$ with e.g. Nb, which is discussed in section 2.1.3.

As described above, in the intermediate temperature regime $\gtrsim$ 750 K and $\lesssim$ 1250 K the anions of SrTiO$_3$ become mobile. This results in a oxygen defect chemistry heavily dependent on the oxygen partial pressure p_{Ox}. For high p_{Ox} oxygen is incorporated and for low p_{Ox} oxygen vacancies are incorporated into the SrTiO$_3$ lattice. The incorporation of oxygen vacancies can be described by eq. 2.2

$$\mathrm{O_O^{x}} \rightleftharpoons \frac{1}{2}\mathrm{O_2} + \mathrm{V_O^{\bullet\bullet}} + 2\mathrm{e}^- \tag{2.2}$$

and the incorporation of oxygen by eq. 2.3:[5–7, 59]

$$\frac{1}{2}\mathrm{O_2} + \mathrm{V_O^{\bullet\bullet}} \rightleftharpoons \mathrm{O_O^{x}} + 2\mathrm{h}^{\bullet} \tag{2.3}$$

Finally $\gtrsim$ 1250 K all species become mobile. Thus, the Schottky equilibrium describing the formation or removal of a complete SrTiO$_3$ formula is activated, as described by eq. 2.4:

$$\mathrm{Sr}_{\mathrm{Sr}}^{x} + \mathrm{Ti}_{\mathrm{Ti}}^{x} + \mathrm{O}_{\mathrm{O}}^{x} \rightleftharpoons \mathrm{V}_{\mathrm{Sr}}^{\prime\prime} + \mathrm{V}_{\mathrm{Ti}}^{\prime\prime\prime\prime} + 3\mathrm{V}_{\mathrm{O}}^{\bullet\bullet} + \mathrm{SrTiO_3} \tag{2.4}$$

Considering the two formation energies of Sr-vacancies and Ti-vacancies, the formation of Sr-vacancies is more likely, as energetically favorable.[60] Their formation can be described by eq. 2.5:

$$\mathrm{O}_{\mathrm{O}}^{x} + \mathrm{Sr}_{\mathrm{Sr}}^{x} \rightleftharpoons \mathrm{V}_{\mathrm{O}}^{\bullet\bullet} + \mathrm{V}_{\mathrm{Sr}}^{\prime\prime} + \mathrm{SrO} \tag{2.5}$$

The formation of the Sr-vacancy is accompanied by the formation of an oxygen vacancy or two holes. The resulting SrO can either result in 2D or 3D defects, which are described below.[20, 61] A good indication for significant amounts of cation vacancies in $\mathrm{SrTiO_3}$ is the accompanying lattice expansion, which results from the high electrostatic repulsion of the vacancies.[10, 60, 62]

Following the influence of the oxygen pressure on the thermodynamical equilibrium will be described. As mentioned before $\mathrm{SrTiO_3}$ is inherently acceptor-type doped and the interaction of $\mathrm{SrTiO_3}$ with the p_{Ox} is activated for temperatures $\gtrsim$ 750 K. Thus, these conditions will be implied for below explanations. The p_{Ox} dependent equilibrium of $\mathrm{SrTiO_3}$ can be divided into three regimes as shown in figure 2.2 a).

In the lowest p_{Ox} regime (extrinsic) more oxygen vacancies are created than inherent acceptor type impurities are available. The charge of the oxygen vacancies exceeding the concentration of inherent acceptor dopants is thus compensated by electrons. This results in eq. 2.6:[55]

$$n \approx 2\mathrm{V}_{\mathrm{O}}^{\bullet\bullet} \tag{2.6}$$

If the temperature is high enough to activate the Schottky equilibrium the concentration of the Sr-vacancies on this regime is anti-proportionally coupled with the electron concentration resulting from the oxygen vacancies due to their negative charge.

Upon increasing the p_{Ox} the charge of the decreasing concentration of oxygen vacancies can be compensated by the acceptors. Ultimately the oxygen vacancy concentration is pinpointed by the acceptor concentration resulting in eq. 2.7.[55]

$$V_O^{\bullet\bullet} = \frac{A'}{2} \tag{2.7}$$

Nevertheless, the electron concentration n and hole concentration p in this regime are still p_{Ox} dependent. Due to their orders of magnitude lower concentration they are massively influenced even by the smallest changes in the oxygen vacancy concentration, which are still possible, namely the electron concentration further decreases with the increasing p_{Ox} and the hole concentration increases.[55] For a high enough oxygen pressure the hole concentration exceeds the electron concentration.[55]

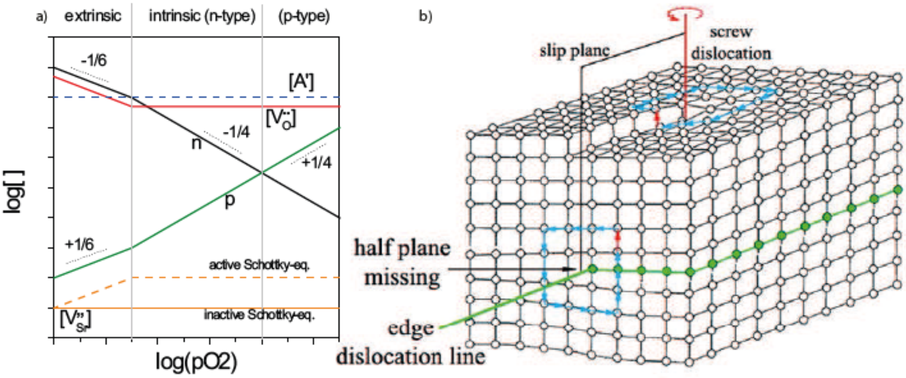

Figure 2.2: a) Schematic illustration of the defect concentrations in acceptor doped $SrTiO_3$ in dependence of the p_{Ox}, courtesy of Dr. rer. nat. Felix Gunkel b) Illustration of edge and screw dislocations from reference [63].

1D Dislocations

Two types of dislocations can be differentiated: Screw and edge dislocations. Both types are illustrated in figure 2.2 b). Edge dislocations are defined by an extra or missing plane of atoms within the crystal. Screw dislocation on the other hand can best be described by a helical insertion of such an additional plane. Opposite to vacancies these defects are non-equilibrium defects, meaning they do not occur in unstrained crystals in thermodynamic equilib-

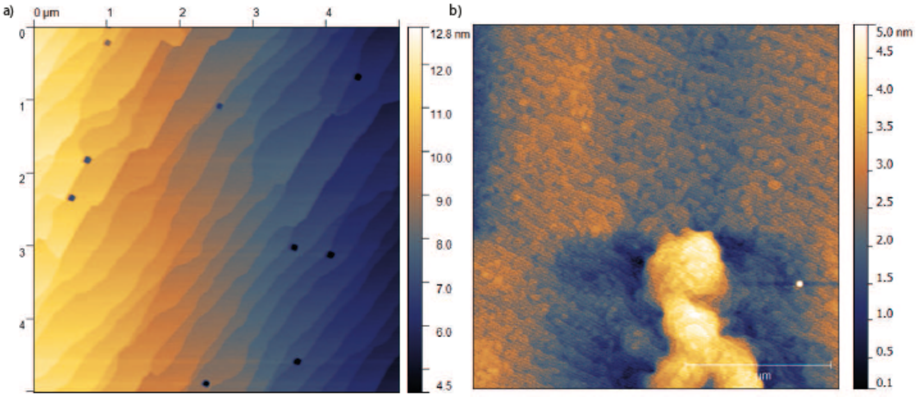

Figure 2.3: a) Etch pits and b) screw dislocation at the surface of a $SrTiO_3$ single crystal substrate.

rium conditions.[53] Nevertheless, both types are commonly observed, not only in thin films but also in $SrTiO_3$ single crystals. Figure 2.3 shows the effect of both types of dislocations for the $SrTiO_3$ single crystal surface. Figure 2.3 a) displays the etch pits, which can be observed after the TiO_2-termination process of these substrates, which will be described in chapter 3.1. These etch pits mark the point an edge dislocation meets the surface.[64, 65] Figure 2.3 b) shows the topography resulting from a screw dislocation meeting the surface.[66, 67] The reason behind the formation of dislocations is stress. This stress can result e.g. from processing steps during crystal growth and polishing.[65, 68]

2D Grain boundaries and anti phase boundaries

In the case of single crystals and epitaxial thin films grain boundaries do not play a role. Anti phase boundaries are very common defects in thin films and Ruddlesden-Popper type anti phase boundaries are one possibility in $SrTiO_3$ to accommodate the additional SrO resulting from eq. 2.5. They are best described by a SrO stacking fault as depicted in figure 2.4. Instead of the alternating TiO_2 and SrO layers, two or more SrO layers in direct succession disrupt the periodicity of the crystal. While anti phase boundaries are naturally also non-equilibrium defects they often occur during non-equilibrium growth conditions. Non-stoichiometry and kinetic limitation typically promote their

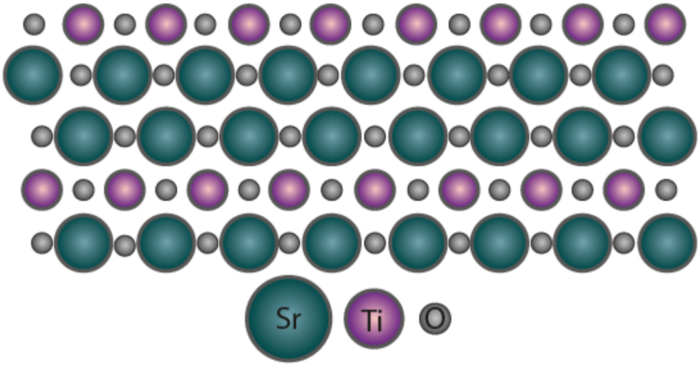

Figure 2.4: Schematic depiction of a Ruddlesden-Popper type anti phase boundary.

formation.[20, 61, 69]

3D Bulk defects

Typical 3D defects are e.g. cracks, pores and precipitates.[53] SrO precipitates typically have a rock salt structure and are the second possibility for $SrTiO_3$ to accommodate the additional SrO resulting from eq. 2.5. If the additional SrO is not kinetically limited, it was shown that the accommodation by precipitation on the surface is preferable in comparison to the above described formation of Ruddlesden-Popper type anti phase boundaries.[61]

2.1.3 Electronic Structure

In its undoped equilibrium state, $SrTiO_3$ is a wide band gap insulating oxide with $\Delta E = 3.3$ eV (figure 2.1 b)).[70] As already described above, the formal oxidization states of the ions in $SrTiO_3$ are Sr^{2+}, Ti^{4+} and O^{2-}. These result from a transfer of the valence electrons of Ti 3d, Ti 4s and Sr 5s into the O 2p orbital. The valence band shown in figure 2.1 b), thus, is formed by the O 2p states and the conduction band in figure 2.1 b) by the empty Ti 3d and Sr 5s states.[71]

As described in the above section one possibility to achieve electronic conductivity is the formation of oxygen vacancies. In the band model they can be described as shallow donors (figure 2.1 b)) and contribute two electrons to the conduction band, if in the extrinsic regime (eq. 2.6). This results in n-conductivity and can, as previously discussed, be described by eq. 2.2. Formally this changes the valence of Ti from Ti^{4+} to Ti^{3+}.

A second method to achieve n-type conductivity in $SrTiO_3$ is doping with Nb. Nb doping exchanges parts of the Ti^{4+} with Nb^{5+}. The additional positive charge can either be compensated by electrons or Sr-vacancies. In the moderately reducing regime electronic compensation is dominant, resulting in an electron in the conduction band (figure 2.1 b)).[72] By successive doping with Nb it is thus possible to change the $SrTiO_3$ properties from insulating to n-type semiconducting, and ultimately to metallic conducting.[73]

2.2 $LaAlO_3/SrTiO_3$

Similarly to $SrTiO_3$ $LaAlO_3$ is a wide band gap insulator with $\Delta E = 5.5-6.0$ eV.[74] $LaAlO_3$ has a rhomboedric crystal structure, which can be described as a distorted perovskite. Considering $LaAlO_3$ as such, the A-site is La^{3+} and the B-site Al^{3+} (compare figure 2.1 a)).[75] In contrast to $SrTiO_3$, which has, as described above, non-polar alternating layers of SrO and TiO_2in the [001] direction, $LaAlO_3$ consists of polar alternating layers of LaO^+ and AlO_2^- in the [001] direction.[76]

In 2004 Ohtomo *et al.*[25] discovered that, despite the insulating properties of both, $SrTiO_3$ and $LaAlO_3$, a deposition of $LaAlO_3$ on $SrTiO_3$ single crystals can result in the formation of a 2-dimensional electron gas (2DEG) at the interface.

The most prominent explanation is that the formation of a 2DEG results from the combination of the polar $LaAlO_3$ planes with the non-polar $SrTiO_3$ planes, which results in a polarity discontinuity at their interface as shown in figure 2.5 a). To evade a polar catastrophe half an electron is transfered to the TiO_2-terminated n-type interface, ultimately resulting in a 2DEG, as shown in figure 2.5 a).[34] In the same way, one would expect half a hole to be transfered into the p-type interface for a SrO-termination. The potential build-up is, however, in this case compensated by positively charged oxygen vacancies rather than by holes.[77] This results in an insulating interface for the SrO-termination.[34] The n-type conducting interface was

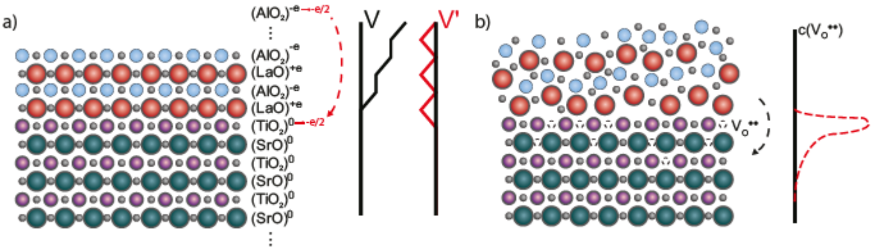

Figure 2.5: Schematic illustration of the origin of interface 2DEG conductivity for a) crystalline $LaAlO_3/SrTiO_3$ and b) amorphous $LaAlO_3/SrTiO_3$.

shown to prevail for interfaces with up to 83% SrO-termination, which can be explained by the formation of the 2DEG in the TiO_2-terminated areas and percolation paths in between those areas.[76, 78]

If $LaAlO_3/SrTiO_3$ heterostructures are grown at low oxygen pressures the conduction mechanism changes. This groups has shown that the growth of crystalline $LaAlO_3$ at oxygen pressures $\leq 10^{-3}$ mbar results in a shift from 2DEG conductivity to bulk conductivity, when quenching the sample immediately after growth.[35, 79] The appearance of bulk conductivity in crystalline $LaAlO_3/SrTiO_3$ can be explained by the incorporation of oxygen vacancies in the $SrTiO_3$ bulk, which contribute electrons to the conduction band as described above. During its low pressure growth, $LaAlO_3$ sucks oxygen from the underlying $SrTiO_3$ substrate resulting in the formation of oxygen vacancies in the $SrTiO_3$.[80] The shift towards bulk conductivity can easily be identified as it is accompanied by a shift towards lower resistivity. [18, 22, 25, 35, 76, 79, 81–86] The carriers resulting from a bulk reduction of $SrTiO_3$ described by eq. 2.6 easily excel the expected sheet carrier concentration $n_S = 10^{14}$ cm^{-2} for interface conduction.

Interestingly the observed carrier densities for amorphous $LaAlO_3/SrTiO_3$, figure 2.5 b), are in a similar regime as for the crystalline case ($n_S \approx 10^{14}$ cm^{-2}). The conductivity of the amorphous $LaAlO_3/SrTiO_3$ can in contrast to the crystalline case not be explained by the avoidance of the polar catastrophe, as the missing long range order already avoids the build up of a potential. Similar to the bulk conductivity of crystalline $LaAlO_3/SrTiO_3$ grown at low pressures, the 2DEG conductivity of the interface between amorphous $LaAlO_3$ and $SrTiO_3$ single crystals relies on the incorporation of oxygen vacancies into the $SrTiO_3$ lattice.[85, 87, 88] The main difference is their confinement to the interface in case of amorphous $LaAlO_3/SrTiO_3$, as shown in figure 2.5 b). The confinement is based on the kinetic limitation of the oxygen vacancies, as amorphous $LaAlO_3$ is usually deposited at room temperature.

2.3 Resistive Switching

Resistive switching is based on the reversible change of the resistance of an active material between two electrodes (MIM) by applying electrical stimuli. Typically the low resistance state (LRS) is defined as 1, while the high resistance state (HRS) is defined as 0. Resistive switching can be based on several mechanisms, prominent examples are phase change memories (PCMs) and valence change memories (VCMs). $SrTiO_3$ is an intensely investigated model material of the valence change memory class, i.e. for filamentary resistive switching transition metal oxides.[89–91]

Virgin MIM structures are usually in a highly insulating state, with a resistance comparable to the HRS.[92] The first transition into the LRS in most cases requires a forming step. The forming step is characterized by a higher necessary voltage than subsequent sweeps to change from the HRS into the LRS (SETs). As the low resistive state is characterized by the formation of a conductive oxygen vacancy rich filament, the limiting factors of eq. 2.2 can either be the diffusion of the oxygen vacancies or their generation by the release of oxygen gas. Two central parameters that were identified influencing these factors are Joule heating and the electrical field.[93, 94]

The polarity of the applied stimuli for forming, subsequent SETs and RESETs defines the switching polarity. Most prominently one differentiates 8-wise switching (8w) figure 2.6 a) and counter 8-wise switching (c8w) figure 2.6 b). Depending on the layout of the MIM and the structure as well as thickness of the insulating layer both of these polarities have been observed in $SrTiO_3$.[95, 96]

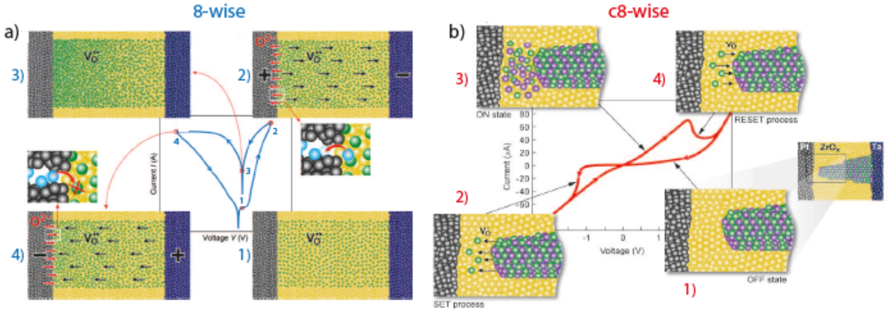

Figure 2.6: Switching mechanism for a) 8w resistive switching and b) c8w resistive switching. Adapted from [97, 98].

Among these switching polarities c8w is the one observable for the widest range of materials, besides for $SrTiO_3$ it was reported for multiple other oxides such as TaOx, HfOx, TiOx and ZrOx.[97, 99] As depicted in figure 2.6 b) for c8w switching the appliance of a negative voltage to the Schottky type interface results in the SET, while the appliance of a positive voltage results in the RESET. C8w switching is best explained by the disc-plug model, as depicted in the inlets of figure 2.6 b).[97] The fully oxidized material, ZrOx in this example, is represented by the yellow spheres. The metal forming the Schottky contact, in the depicted example Pt, is shown as silver spheres. The metal forming the Ohmic contact, here Ta, is represented by the blue spheres. The reduced Zr ions are represented by purple spheres and the oxygen vacancies by green spheres. The conducting plug, which is rich in oxygen vacancies and reduced Zr ions, results from the forming step. 1) In the OFF state the conducting plug is separated from the Schottky contact by a fully oxidized disc. 2) During the application of the negative SET voltage the double positively charged oxygen vacancies are driven into the disc resulting in formally reduced Zr ions in the disc and ultimately in conduction through the disc, 3) the ON state. 4) Applying an opposite voltage reverses the process, the oxygen vacancies are pushed back into the plug and the disc returns to its insulating state, 1) the OFF state. C8w switching can thus solely be explained by an internal rearrangement of oxygen vacancies, while an oxygen exchange with the electrodes or atmosphere are not regarded.

In $SrTiO_3$ of high crystal quality and sufficient low thickness the opposite switching polarity, 8w, is observed.[95, 96] The 8w polarity usually is observed for switching that is limited by oxygen diffusion instead of the exchange reaction. In contrast to the well known c8w switching mechanism, the 8w switching mechanism was only recently unrevealed by this group.[98, 100] For 8w switching, switching into the LRS is achieved by applying a positive voltage to the Schottky-type interface as shown in figure 2.6 a). 1) shows the state of the filament in the HRS. Applying a positive bias to the Schottky-type interface 2) results in a faster oxygen vacancy formation at this interface, than the oxygen vacancies are driven away in the direction of the negative bias. This process comes to a stop when the current compliance is reached as the oxygen vacancy rich filament is adequately conducting 2). Applying a negative bias to the Schottky-type interface reverses the process, as oxygen, either stored in the Pt or provided by the atmosphere, gets incorporated into the filament at this interface 4) until the HRS is reached 1). In contrast to c8w switching, 8w switching, thus, relies on the incorporation of oxygen vacancies and oxygen from the atmosphere or the electrode material and not on their internal rearrangement.

3 Experimental methods

3.1 Sample preparation

Mainly two kinds of substrates were used in this work, $SrTiO_3$ and 0.5 wt% Nb:$SrTiO_3$. Substrates were either acquired from *Shinkosha* or *Crystec*, both of which guarantee a miss-cut of below ±0.5°. This miss-cut is responsible for the typical step-edges observable for $SrTiO_3$.[101]

As described in the previous chapter $SrTiO_3$ is a perovskite of alternating layers of SrO and TiO_2, resulting, for as received substrates, in a mixed surface termination of SrO and TiO_2. In some cases in this work a more defined surface termination is desirable. A TiO_2-termination can easily be achieved by etching the as received $SrTiO_3$ or 0.5 wt% Nb:$SrTiO_3$ single crystals (figure 3.1 a)) in buffered HF[51, 102], *TECHNIC BOE 7-1*, for 2:30 min. The resulting substrate shown in figure 3.1 b) has a 100 % TiO_2-termination and shows, as described in the previous chapter, etch pits, which indicate edge dislocations meeting the sample surface. However, the step edges of as received substrates are irregular. To achieve smooth step edges as shown in figure 3.1 c) an annealing step is necessary. Terminated substrates are annealed for two hours and unterminated substrates for four hours at 950 °C, respectively.

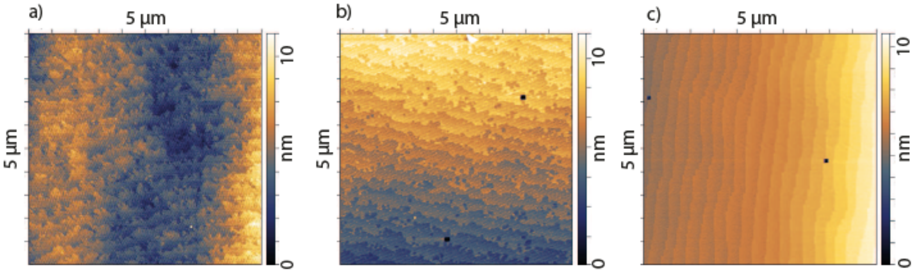

Figure 3.1: a) As received, b) terminated and c) annealed $SrTiO_3$ substrate.

3.2 The oxide cluster tool

The oxide cluster tool depicted in figure 3.2 offers the possibility of an *in situ* transfer between different deposition and analysis techniques. The central ones utilized within this work will be described below. The sample transport within the cluster is based on *Omicron* sample holders, which are slightly modified for some of the cluster tool stations. If not stated otherwise, these holders were used and the samples were fixed with Ag-paste for high temperature depositions and carbon tape for low temperature depositions.

3.2.1 Deposition techniques

Within this work different deposition techniques were used. Epitaxial oxide thin films were grown by pulsed laser deposition. The carbon, HfO_2 and Ta as well as Ta_2O_5 thin films were sputtered. The electrode materials were deposited by e-beam evaporation.

Pulsed laser deposition

Figure 3.3 a) shows the schematics of the PLD system integrated in the oxide cluster. To allow different deposition pressures and process gases it features a gas inlet with the possibility to apply O_2, CO, $^{18}O_2$, Ar and H_2. Pressures $\leq 10^{-3}$ mbar are controlled with a leak valve, while the turbo pump is running at full capacity. For

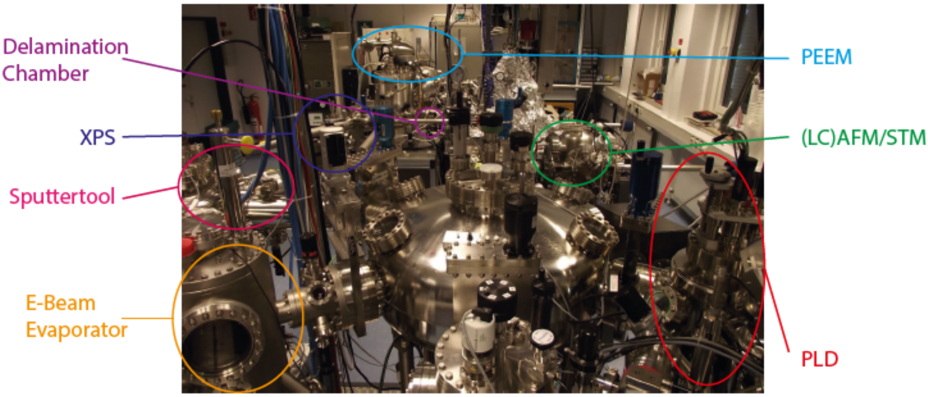

Figure 3.2: The oxide cluster tool including a PLD, an LCAFM/STM combination, a PEEM, a delamination chamber, an XPS, a sputter tool and an e-beam evaporator.

higher pressures a massflow controller is used and the cross section of the pumping valve is reduced using a bypass. The pressure inside the chamber is measured using the appropriate *Pfeiffer* pressure gauges, an *IKR 270* cold cathode gauge measures pressures up to 10^{-2} mbar, a *CCR 364* capacity gauge measures pressures between 1.33×10^{-4} and 1 mbar and a *TPR 280* Pirani gauge measures pressures between 5×10^{-4} and 10^{3} mbar. In case of mass analysis a *Pfeiffer Vacuum PrismaPlus* mass spectrometer is used.

A *Compex 205F - COHERENT* laser is used to obtain a 248 nm 25 ns pulse. Following the path of the laser beam, it first passes an aperture, which can be used to adjust the spot size. Next the attenuator is passed, that allows a precise adjustment of the laser fluence, which is measured using a *LEM 2420*. Subsequently the beam passes the focus lens, which projects the image of the aperture on the target, and finally passes the entry window. To obtain the actual laser fluence it is important to know the permeability of the entry window.

The laser hits the spinning (5 rpm) target on a 2 mm^2 area, ablating the target material. The resulting ablated species absorb the remaining laser pulse, increasing vapor pressure and thermal energy of the ablated material. This results in partial ionization and ultimately in the formation of a plasma. As the resulting plasma plume expands, its ionization and thermal energy convert into kinetic energy. Due to

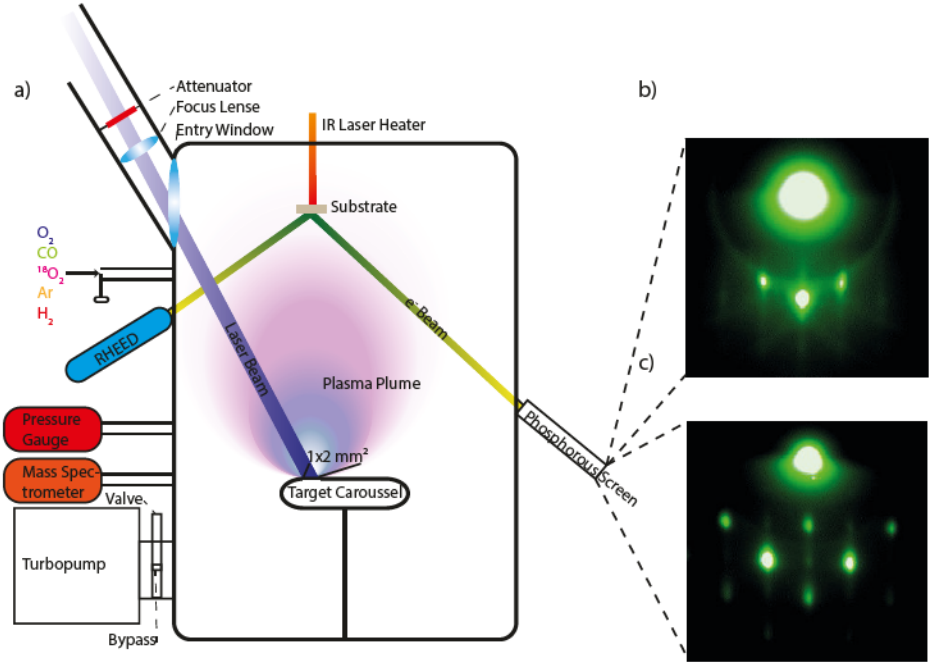

Figure 3.3: a) Schematics of the PLD system attached to the oxide cluster b) RHEED 2D pattern and c) RHEED island growth pattern.

the high energy and short length of the PLD pulses, the target material does not, as it would for the thermodynamical equilibrium, change into the liquid and gas phase, but is directly transfered into a plasma plume. PLD is, thus, a non-thermodynamical equilibrium technique.[3]

This non-equilibrium is influenced by various parameters. Besides the laser parameters as spot size,[103] fluence[17, 104–106] and repetition rate,[107] the interaction between substrate and plume is also influenced by the target substrate distance[104] and the background gas conditions[108]. All of these influence the kinetic energy of the plume and ionization as well as oxidization of the plume species. These in turn influence growth, stoichiometry and crystallinity of the film. The specific influence of each parameter will be discussed in the following.

The background gas conditions were shown to determine between two different expansion regimes of the plasma plume, namely the diffusive and ballistic regime. The plume is in the diffusive regime for high process pressures. Here the growth and resulting film properties are dominated by the oxidization state and the surface diffusivity of the species. In this regime small changes of the oxygen partial pressures p_{ox} significantly change the morphology and stoichiometry of the film, however, the below described influence of the laser fluence decreases. Lower process pressures result in a plume in the kinetic regime.[108] In this regime growth and film properties are predominately influenced by the kinetic energy of the plume species. The kinetic energy influences the scattering with the background gas species and can thus influence the film stoichiometry. Further high energy species can result in sputtering effects on the substrate and growing thin film. Further it can influence the adatom behavior. For all growth pressures used in this work, which can be found in table 3.1, the plume is in the ballistic regime. Although exclusively working in the ballistic regime, this work will within chapter 4.1 provide evidence of the, nevertheless, central role of the oxygen partial pressure.

The spot size was previously investigated for the model material $SrTiO_3$. It was shown that, premising a constant laser fluence, decreasing the spot size results in a decrease of the ionization within the plume and a decrease of its kinetic energy. This was shown to heavily influence the oxidization state of the resulting thin film, as decreasing the kinetic energy of the plume decreases the re-sputtering of oxygen species from film and substrate.[103] To minimize the influence parameters in this work, the spot size was constantly 1x2 mm^2, as shown in figure 3.3 a).

Previous works of this group have shown that the repetition rate influences the species of the adatoms. As different species can e.g. differ in volatility, the repetition rate can in this way directly influence the stoichiometry of the thin film.[107] To avoid influences of the repetition rate, it was as presented in table 3.1 kept constant for each material.

The influence of the fluence will following be discussed in detail, at it is of central importance to understand the fluence dependent stoichiometry of $SrTiO_3$ presented in chapter 4.2. It is thus also discussed exemplary for the model material $SrTiO_3$. In general, two sources of fluence induced non-stoichiometry are differentiated for PLD processes, influences on the target ablation and influences on the plume propagation.[17]

An incongruent ablation of the target usually is accompanied by a strong dependence of the cation stoichiometry on the laser fluence as it is observed for $SrTiO_3$ in chapter 4.2. There are two main reasons for an incongruent ablation of the target. It can on the one hand be the result of an incongruent melting of target materials with complex phase diagrams at low fluence.[17, 109] It can on the other hand be the result of different effective evaporation enthalpies of the involved components.[109, 110] As $SrTiO_3$ has a rather simple phase diagram and melts congruently,[17, 109] it is reasonable that latter is responsible for the fluence dependency.

For non-stoichiometry introduced by different effective evaporation enthalpies a linear dependency of the stoichiometry on the fluence is expected.[109, 110] However, the stoichiometry dependence on the fluence is non-linear for $SrTiO_3$.[17, 104–106] Thus, there has to be another influence factor on the cation stoichiometry by the laser fluence. As mentioned, growth at high pressures result in a low kinetic energy of the species. This is due to interactions with the oxygen. Considering the atomic masses of Sr (87.62 u) and Ti (47.87 u) it is obvious that Sr has the bigger impulse. It is thus less effected by the interaction with other species. The result is a non-linear decrease of the Ti content in dependence of the distance from the target and the time after plume breakdown.[17, 104] This further explains the influence of the target-substrate distance on the cation stoichiometry. In order to eliminate this influence factor the target substrate distance was constantly kept at 44 mm in this work. The fluence used in this work can be found in table 3.1.

Besides these influences another central parameter is the temperature of the substrate. The substrate in this system is, as shown in figure 3.3 a), heated by IR-diode laser. It allows a rapid heating and cool down of the substrate. The heating rate is typically 50 °C/min. A cool down from the typically applied 800 °C to below 250 °C can be achieved within ≈ 40 s. Such a rapid cool down allows the preservation of the non-equilibrium state of defects induced during the PLD growth.

The substrate temperature is a central parameter influencing the surface diffusivity. In case of non-equilibrium growth the surface diffusivity defines the growth mode.

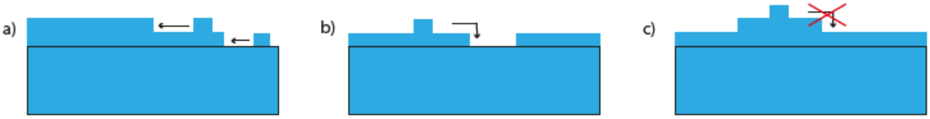

Figure 3.4: Epitaxial growth modes: a) step flow, b) layer by layer and c) second layer nucleation and island growth. The substrate is marked by black edges

Figure 3.4 shows the three growth modes observable for epitaxy. For high temperatures and short step lengths step flow growth can be observed, figure 3.4 a). For intermediate temperatures layer by layer growth is observed, figure 3.4 b), and for low temperatures second layer nucleation, ultimately resulting in islands, is observed, figure 3.4 c).[111, 112]

In order to obtain live information on the growth a RHEED system is applied to the chamber as shown in figure 3.3 a). Figure 3.3 b) shows a typical RHEED pattern for a smooth surface, as observable for 2D growth. The top bright spot is the direct beam. The reflection of the beam on the sample surface results in diffraction spots, which are located on the, in this case 1^{st}, Laue circle. These diffraction spots represent intersections of the Ewald sphere with the reciprocal lattice rods of the surface. This changes for the case of island growth. The formation of islands results in parts of the electron beam being transmitted instead of reflected. If the islands are epitaxial, their reciprocal lattice is the same as of the crystal, and thus a 3D-array of reciprocal points. The intersections of these points with the Ewald sphere result in a RHEED pattern as shown in figure 3.3 c).[113]

The intensity of the RHEED further gives information on the surface roughness. The principal behind this is depicted in figure 3.5. An increasing surface roughness results in an increase of scattering, which in turn results in a decrease of intensity. This principle can be used to monitor layer by layer growth as in figure 3.4 b). Species arriving on the surface will progressively increase the surface roughness until the coverage rate Θ is 50 %. Now additional species will decrease the surface roughness until the original roughness is recreated. This results in an oscillation of the RHEED signal tantamount to the deposition of one monolayer.[113]

This principle can also be used to differentiate between step flow growth and layer by layer growth. As depicted in figure 3.4 a), step flow growth is defined by the

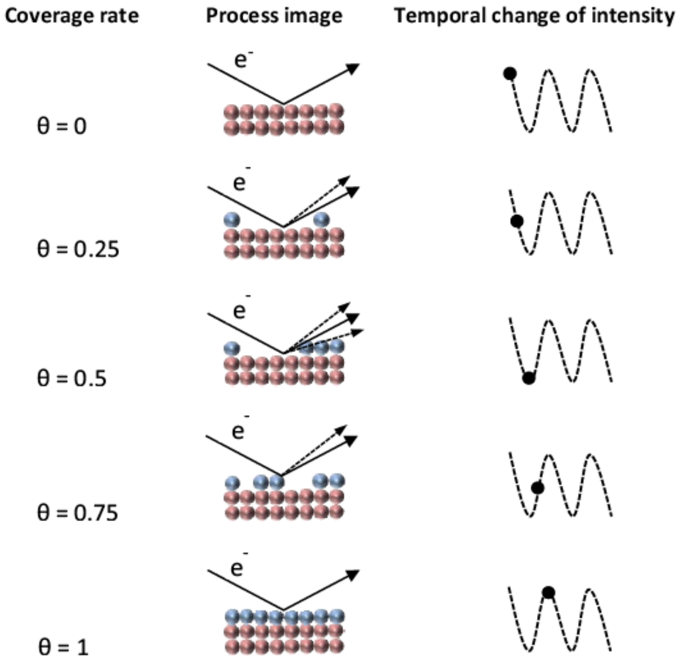

Figure 3.5: Intensity of the RHEED in dependence of the surface coverage. Figure courtesy of Moritz Weber.

intermediate agglomeration of the arriving species at the step edges, thus arriving species do not result in a roughening of the surface and in turn no oscillations of the RHEED intensity are observable.

Besides these more standard RHEED applications, it can also be used to identify the surface termination, which will be described in chapters 4 and 5.

Details of the specific growth parameters for the different target materials can be found in table 3.1. All used targets were single crystals except for SrO_2. A sintered SrO_2 target was used to achieve SrO films, as it has a superior stability in comparison to the desired thin film material.

Table 3.1: Growth parameters used for PLD in this work

	F_L [J/cm^2]	$p(O_2)$ [bar]	f [Hz]	T [°C]
$SrTiO_3$	0.63-1.58	0.01	5	800
crystalline $LaAlO_3$	1.3	$10^{-6/-5}$	1	800
amorphous $LaAlO_3$	1.3	10^{-5}	1	RT
SrO	0.81	10^{-8}	1	800

Sputter tool

The sputter tool, which is part of the cluster (figure 3.2), offers the possibility of DC magnetron and RF sputtering. Both techniques will be introduced in this section alongside the parameters used for the deposition of Ta, Ta_2O_5, HfO_2 and C.

The simplest sputter technique is DC sputtering. It is based on a glow discharge between two electrodes, where the substrate is the anode and the target is the cathode. To achieve a sputtering of the cathode material a process gas in form of a noble gas is necessary, usually Ar. After a first random ionization event, avalanching results in the formation of a plasma. The glow discharge created Ar^+ ions are accelerated in the direction of the cathode, where they cause a momentum transfer cascade resulting in ablation of the target material. The ablated material propagates to the substrate surface, where it nucleates. Sputtering in this fashion would result in a very low yield. The yield can substantially be increased by applying magnetron sputtering. Magnetron sputtering is based on the application of a magnetic field at the target material forcing the electrons to move in a spiral. This increases the probability of electrons ionizing Ar atoms. As a result of the increased ion density, more Ar^+ ions are accelerated towards the target ultimately increasing the sputter yield. As DC magnetron sputtering only allows for metallic targets, the deposition of oxide thin films demands the application of a reactive process gas, namely oxygen. Thus an oxygen argon mixture is used instead of pure argon. The precise mixture of this process gas allows for the tailoring of the thin film's oxidization state.[114, 115]

As mentioned a major drawback of DC magnetron sputtering is its limitation to conducting target materials. For insulating materials the accelerating field cannot be directly applied, as the target would charge upon bombardment. This can be circumvented by applying RF sputtering. For RF sputtering the applied field has a frequency that is high enough to only allow the light electrons to follow it, but not the much heavier Ar^+ ions, resulting in a charge neutralization on the target. A positive side effect of this method is the further improved collision probability between Ar atoms and electrons, improving as described above, the sputter yield.[116]

The sputter tool used in this work was build by *Surface*. Its base pressure is $\approx 10^{-9}$ mbar. The parameters applied in this work can be found in table 3.2. The growth rate (rate) was determined by X-ray reflectometry (see below); d_{ts} describes the distance between substrate and target.

Table 3.2: Growth parameters used for sputtering in this work

	method	p [bar]	O_2/Ar	P [W]	d_{ts}	rate [s/nm]
C	DC	10^{-3}	0	5	min.	200
C	RF	10^{-2}	0	50	min.	60
Ta_2O_5	RF	$5{\cdot}10^{-3}$	2/3	200	max.	64
Ta	RF	$5{\cdot}10^{-3}$	0	20	min.	14.57
HfO_2	RF	$5{\cdot}10^{-3}$	2/3	200	max.	25.71

E-beam evaporation

In this work two different e-beam evaporators are used. Additional to the custom one attached to the oxide cluster shown in figure 3.2, an *ex situ* custom e-beam evaporator is used. The *in situ* evaporator is based on an e-beam source by *Telemark*, the *ex situ* evaporator on a *Ferro Tec Carrera*. One central difference between the systems is, that the *ex situ* evaporator uses carbon crucibles, while the *in situ* one does not.

The basic working principle of an evaporator is rather simple. The target material is heated above its vaporization point and the substrate is placed at a defined distance from the target. As the substrates surface is cold, the vapor condenses on its surface and a thin film forms. In case of e-beam evaporation the target is heated by a electron beam, which is patterned to allow an even evaporation.[117]

Both systems used in this work utilize a quartz crystal oscillator to monitor the thickness of the deposited film. The deposition rate of the *in situ* system was set to ≈ 0.2 Å/s and of the *ex situ* to ≈ 1 Å/s. The electrode thickness generally is 30 nm, Au leads are 100 nm thick.

3.2.2 Analysis techniques

The analysis techniques within this work were either applied *in situ* utilizing the possibilities of the clusters or, if *in situ* processing was not necessary, *ex situ*. In the following the analysis techniques will be briefly described. More specialized analysis techniques that were performed by collaborators are introduced upon presentation of the properly results.

Atomic force microscopy

Within this work different AFMs were used. *In situ* measurements were performed with an *Omicron VT AFM XA* in static mode and analyzed using *Vernissage*. *Ex situ* measurements were made utilizing either a *SIS Pico Station UltraObjective* or a *Cypher AFM* or a *nanosurf Flex Axiom*, each in dynamic mode, and were analyzed using *Gwyddion*. A detailed complete description of atomic force microscopy can be found in reference [118].

X-ray photon spectroscopy

X-ray photon spectroscopy measurements and analysis were carried out with the help of Dr. ret. nat. Christoph Baeumer. The XPS is a *PHI 5000 Versa Probe*, the photoemission angle was 45°, if not stated otherwise, and the spectra were fitted using *Casa XPS* with a Shirley background and a convolution of Gaussian and Lorentzian line shape. The working principle of XPS analysis can be found in reference [119].

X-ray diffraction

X-ray diffraction was performed *ex situ* using a *Philips PW 3020 diffractometer* with a Cu-Kα X-ray tube in Bragg-Brentano geometry. X-ray reflectometry measurements were fitted using *GenX*. Θ-2Θ scans and rocking curves were fitted using *Fityk*. A detailed description of the working principles of X-ray diffraction can be found in reference [120].

3.3 Device Patterning

After deposition of a resistively switching insulator, its characterization and the deposition of the top metal layer, the next step is a patterning of this top layer. Two different patterning approaches were used in this work. The standard approach results in 10x10 μm^2 Pt pads as top electrode shown in figures 3.6 a), which are directly contacted by W-whiskers tips for below described electronic characterization. The second approach was developed to reduce the influence of the contact resistance between whisker tip and pad, which is necessary for the below described variability measurements. This is achieved by contacting a metal lead (Au) instead of the pad. To avoid switching at the metal lead, it is insulated from the film by a 70 nm insulator layer (HfO_2). The resulting MIM structure is shown in figures 3.6 b). Figure 3.6 shows the structure for the mostly used $SrTiO_3$ based MIMs in this work. In the case of Ta_2O_5 based MIMs the $SrTiO_3$ is interchanged with Ta_2O_5 and the bottom electrode is Ta. Below a step by step guide for the device patterning can be found.

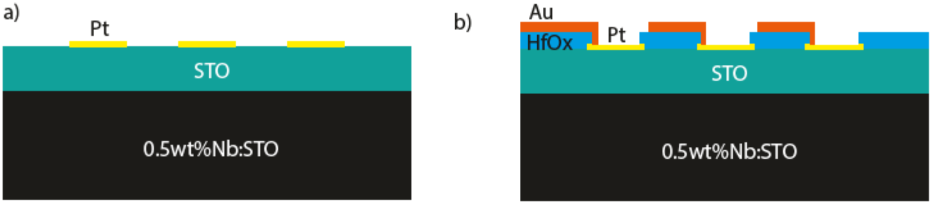

Figure 3.6: a) Schematic side view of the standard layout. b) Schematic side view of the layout developed for variability measurements.

1. The sample is cleaned by swiping in isopropyl alcohol, blow drying with N_2 and dehydrating at 180 °C for 3 min.
2. After the sample has cooled down to room temperature it is coated with *AZ5204* photo resist and heated for 3 min at 90 °C.
3. When the sample has reached room temperature once more, it is exposed to UV light for 15 s covering the future device areas utilizing a *Suss MicroTec MA6* mask aligner.
4. The photo resist is developed in *MIF326* until the devices become visible. This takes between 30 and 60 s.
5. Reactive ion beam etching using an *Oxford Instruments Ionfab 300plus* disposes of the spare top electrode material.
6. To lift the remaining photo resist the samples are stored in acetone over night. Subsequently they are cleaned by swiping in isopropyl alcohol.

At this step the standard approach allowing the direct contacting of the pads by W-whisker tips is finalized. A microscopic image of the finished devices is shown in figure 3.7 a). For MIMs with a metal lead additional steps as listed below are necessary. These additional steps were performed by Jan Rieck.

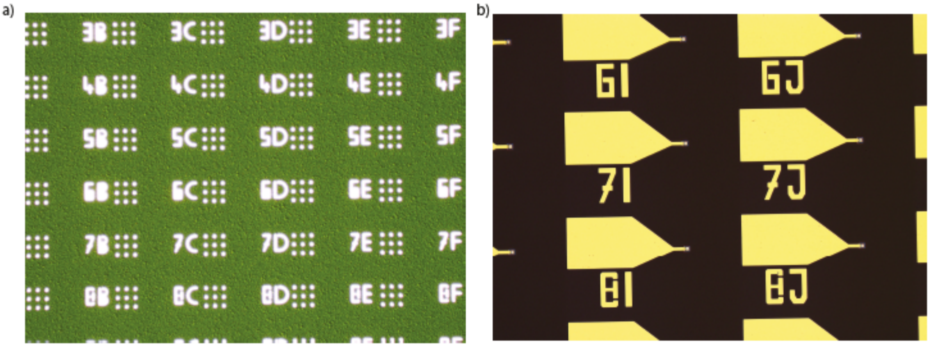

Figure 3.7: Microscopic images of the finished devices of a) a standard MIM and b) of a MIM with metal leads.

7. The sample is dehydrated at 180 °C for 3 min.

8. After cooling down to room temperature the sample is coated with *AZ5214* photo resist and heated for 3 min at 90 °C.
9. Again the sample cools down to room temperature and is then exposed to UV light for 25 s by the mask aligner, covering the center of the device areas.
10. Step 4 is repeated.
11. After depositing the 70 nm HfO_2 layer as described before, the sample is heated to 80 °C in dimethyl sulfoxide (DMSO) for 2 hours to lift the photo resist. Subsequently the sample is swiped in acetone, cleaned in isopropyl alcohol and blow dried with N_2.
12. Step 7 is repeated.
13. After cooling down, the sample is coated with *AZnLof*, baked at 90 °C for 3 min and cooled down to room temperature.
14. The areas of the future metal leads are concealed while exposing the sample to UV light with help of the mask aligner for 10 s.
15. The photo resist is baked out at 110 °C for 1 min.
16. The photo resist is developed in *MIF726* for 45 s.
17. After depositing the ≈ 100 nm metal leads by e-beam evaporation (see above), the photo resist is removed by *MicroChemicals TechniStrip Ni555* at 80 °C for 2 h. Subsequently the sample is swiped in acetone, cleaned in isopropyl alcohol and blow dried with N_2.

A microscopic image of the resulting structure can be found in 3.7 b).

3.4 Electronic characterization

Hall measurements

The electronic transport properties of $SrTiO_3$ single crystals and $LaAlO_3/SrTiO_3$ heterostructures were investigated utilizing two different setups. For both setups the samples were bonded with Al wire. Low temperature electronic transport measurements were performed in the Hall bar geometry by Marc Rose using a physical property measurement setup. Detailed information on temperature dependent electronic transport measurements can be found in reference [121].

Room temperature Hall measurements were performed with a *Lake Shore 8400 Series* in the van der Pauw geometry in two different operating modes, AC and DC. In the DC mode the magnetic field is steady, in the AC mode it is sinusoidal, allowing measurements for lower mobilities. When samples showed no detectable conductivity the detection limits of the *Lake Shore 8400 Series* were assumed. These are 10^{10} cm^{-2} for the sheet carrier concentration, 0 $\mathrm{cm}^2/\mathrm{Vs}$ for the Hall mobility and $10^8\Omega/\square$ for the sheet resistance. The principal of Hall measurements and van der Pauw geometry can be found in references [122] and [123], respectively.

I(V)-measurements

To characterize the devices that were fabricated as described in section 3.3 the Pt pads or Au leads were contacted using W-whisker tips. The bottom electrode was contacted by Al wire bonding. The *I(V)*-characteristics and resistance read outs were performed by a *Keithley 2611A SourceMeter* with a a step size of 20 mV and a holding time of 5 ms. A typical characterization starts with the read out of the virgin state. For the read out 0.5 and -0.5 V are applied. The resulting linear *I(V)*-slope is fitted between -0.1 and 0.1 V to obtain the resistance. For the forming of the device 3 V are applied with a current compliance of 10 mA or 30 mA. After another read out the device is switched OFF using -4 V. Once more a read out is preformed before switching the device in the ON state again using 3 V and performing time dependent read outs for retention time measurements. The retention time measurements were exclusively performed om MIMs patterned as in figures 3.6 a) and 3.7 a).

Variability measurements were solely performed on the MIM layout presented in 3.7 b), as it was observed that the influence of the variability by the W-whisker tip's contact to the Pt pad can shadow the device variability. For the variability measurements the current compliance always was 10 mA, as the metal lead structure was destroyed for higher compliances. Instead of performing time dependent read outs, 2000 cycles were performed per device, with each cycle being followed by a read out. This number of cycles largely prevents influences of the device endurance. The resulting resistances are, within this work, presented in Weibull plots, with the Weibull slope β given as a variability parameter.[124] All variability measurements were performed by Jan Rieck.

4 Influences on the defect structure

As described in chapter 2.1.2 a broad variety of defects can be observed in $SrTiO_3$. The aim of this chapter is to gain control over the formation of such defects. Section 4.1 focuses on various influences on the oxygen vacancy formation in $SrTiO_3$. This will be accomplished considering crystalline and amorphous $LaAlO_3$ grown epitaxially on $SrTiO_3$. Two heterostructures which are highly sensitive to the formation of oxygen vacancies as described in chapter 2.2. The subsequent section 4.2 sheds light on the influence of actively changing the cation stoichiometry on the defect formation during PLD growth.

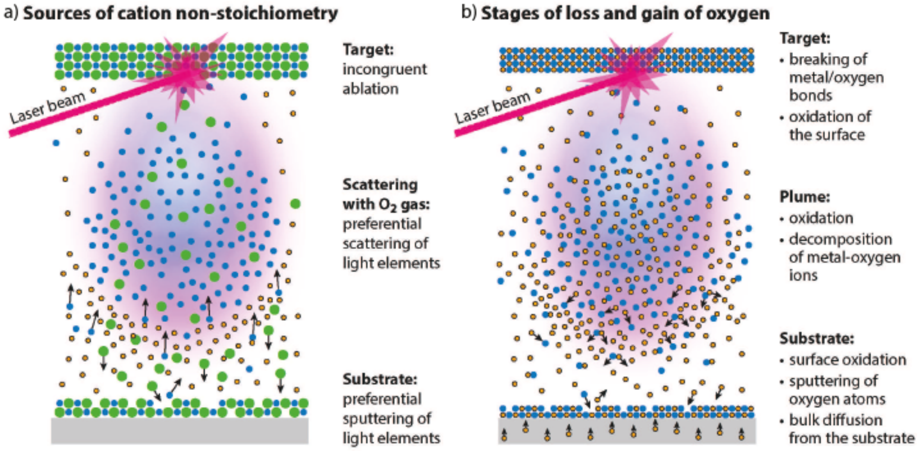

Figure 4.1: Influences on the stoichiometry during PLD growth: a) influences on the cation stoichiometry and b) influences on the anion stoichiometry equivalent to the oxygen stoichiometry. Figure modified from reference [125]

4.1 Anion stoichiometry

In this section influences on the anion stoichiometry during PLD processes will be discussed. As described in chapter 2.1 the formation of ample oxygen vacancies in $SrTiO_3$ results in conductivity. Oxygen vacancies thus play a central role for the properties of $SrTiO_3$ and have to be avoided or introduced for certain applications. The central role of oxygen vacancies for all $SrTiO_3$ applications has resulted in intense research efforts to understand and control their formation.[5–8, 35, 79, 80, 85, 103, 126–128] Apart from the classic influence factors such as temperature and pressure[5–7] specific influences occur during PLD: the oxidization of the oxygen deficient thin film *via* the substrate resulting in the formation of oxygen vacancies in the substrate[85, 103, 127] and impinging species of the plasma plume resulting in an oxygen removal.[80, 88, 128] (compare Figure 4.1 b)) Although a wide variety of influence factors on the oxygen stoichiometry during PLD is already investigated, open questions remain. Some of these questions will be addressed in this chapter. The oxygen sensitive heterostructure $LaAlO_3/SrTiO_3$ (compare chapter 2.2) will be utilized for this, where applicable. The results presented in this section have been published in part in references: [126, 129]

4.1.1 Enhanced oxygen vacancy formation at low pressures

One of these open questions occurs when comparing the existing literature regarding the reduction of $SrTiO_3$. It is conspicuous that one finds different oxygen pressures required to achieve reduction for vacuum annealing and for chemically controlled reducing atmospheres. The unraveling of this discrepancy is of high interest for low pressure PLD to gain further understanding of the reduction of the $SrTiO_3$.

Numerous examples can be found in literature for the reduction of $SrTiO_3$ substrates during pulsed laser depositions for physical oxygen pressures below 10^{-5} mbar.[22, 35, 85, 86, 130–134] This opposes the results of chemically controlled reducing atmosphere annealing experiments ($H_2/Ar/O_2$ mixtures), for which the sample is, in opposite to vacuum annealing, under a physical pressure of 1 bar. These experiments determined that $SrTiO_3$ reduction, in case of inherent acceptor-type impurity content, will only take place at oxygen partial pressures below 10^{-17} mbar even at elevated temperatures.[5, 6, 21, 59] The contradiction is often explained by the influence of the laser plume during growth.[85, 103, 132] Lee *et al.* e.g. have recently found that an increased ion bombardment *via* the laser plume results in an increased reduction.[103] Another explanation often found in literature is the oxidization of the growing thin film by the $SrTiO_3$ substrate, eventually resulting in the reduction of the substrate.[80, 88, 135] However, as soon as the plume is turned off one would expect the oxygen content of the sample to approach the equilibrium value and thus to re-oxidize at a certain rate within the PLD chamber .[35]

The reduction of $SrTiO_3$ in PLD vacuum chambers, however, is not only observed during deposition, but also observed when annealing at physical oxygen pressures below $\approx 7 \cdot 10^{-7}$ mbar [22–24], which is in contradiction to the thermodynamic equilibrium measurements performed in chemically controlled gas mixtures or with oxygen pumps [5, 6, 59]. No prior work sufficiently explained this contradiction between physical oxygen pressure and chemically controlled oxygen pressure. The oxygen pressures used for vacuum annealing ($\approx 10^{-6}$ mbar) are considered as low pressure growing conditions. However, the oxygen pressure is comparably high considering the thermodynamical equilibrium of $SrTiO_3$. In other words, a chemical oxygen partial pressure of 10^{-6} mbar is not reducing at all. Understanding the reduction mechanism of $SrTiO_3$ in vacuum chambers at comparably high oxygen pressures as a first step may subsequently improve the understanding of the low pressure growth of oxides by PLD. Based on this understanding it may be achievable to grow at low physical pressures, but at the same time to avoid a reduction of the substrate.

The influence of some of the most common procedures typically involved in PLD processing were investigated. First the influence of contaminations, which originate on the one hand from adsorbates on the holder as well as the sample and on the other hand from the gluing of samples on holders with Ag-paste, are investigated. Second the influence of measurement devices attached to the PLD chamber, namely a cold cathode gauge for pressure measurement and a mass spectrometer, is investigated. Being able to explain the reduction of $SrTiO_3$ during annealing, the reduction of $SrTiO_3$ during depositions is disentangled using $LaAlO_3$ growth on $SrTiO_3$ due to its oxygen pressure sensitivity (compare chapter 2.2).[22, 35, 59, 131] The influences induced by the plume are separated from influences of an insufficient supply of oxygen and influences of the measurement devices.

Influence of contaminations

A first hint to a possible reason for the reduction of $SrTiO_3$ at comparably high oxygen pressures are the findings of Frederikse *et al.*, who observed the presence of oil of their forepump in their vacuum chamber to accelerate the reduction process of $SrTiO_3$.[23] Based on this observation, one may surmise that the gas mixture present when annealing in vacuum chambers may actually contain only small partial pressures of oxygen, p_{ox}, resulting in a discrepancy between the measured total pressure p inside the chamber and the actual p_{ox}, due to contaminations.

Thus, in a first step, the gas mixture present during a typical annealing process in a vacuum chamber is investigated. For this $SrTiO_3$ single crystals glued on the holder using Ag-paste are heated for 1 h in the PLD chamber with a rate of 20 °C/min to 800 °C. Utilizing the diffusion constant by de Souza *et al.*[7] the diffusion length of oxygen vacancies is determined to be 8 mm, when annealing at 800 °C for 1 h, and, therefore, to exceed the sample dimensions. Furthermore a surface reaction limitation can be excluded for high temperatures.[136] Therefore, it can be assumed that the samples are in thermodynamical equilibrium.

Some samples were treated with an additional pre-annealing step at 400 °C. This temperature is high enough to evaporate most of the organic solvents and adsorbates, but at the same time no detectable reduction on the chosen time scales appears for $SrTiO_3$.[7] At the end of the experiment, the samples are quenched reaching a temperature ≤ 350 °C within 65 s, what circumvents further changes in the samples. The background pressure before the start of the experiment is $\approx 3 \cdot 10^{-8}$ mbar. During the experiment the pressure is set to 10^{-6} mbar with the help of a constant oxygen flow. It is measured using a cold cathode gauge throughout all experiments of figure 4.2. Further a mass spectrometer was running during these experiments to analyze the gas composition.

Figure 4.2 shows the obtained mass spectrometry data for annealing a sample 1 h at 800 °C without a) and with b) an additional pre-annealing step (0.5 h). In both cases

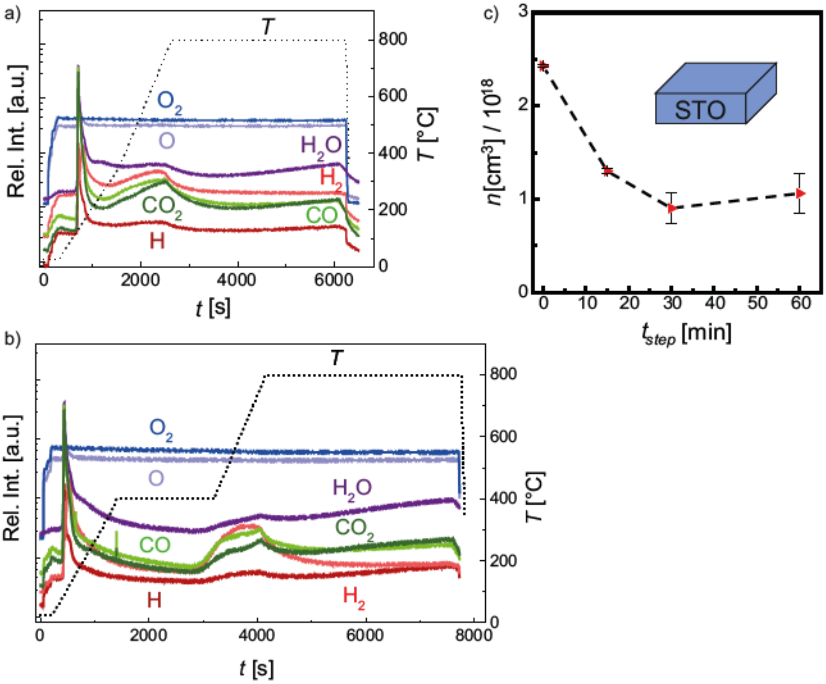

Figure 4.2: a) Mass spectrometry data during thermal annealing of $SrTiO_3$ crystals inside a PLD chamber at 10^{-6} mbar without pre-annealing. The mass spectrometry graphs show the relative intensity of the measured ions (y-axis) over time (x-axis). b) mass spectrometry data obtained for two-step annealing ($T = 400$ °C for 0.5 h pre-anneal followed by $T = 800$ °C for one hour). c) Carrier concentration (y-axis) for different durations of the pre-annealing step (x-axis). The error bars indicate the standard deviation of the carrier concentration measured for at least two equally treated samples, verifying the reproducibility of our results. The dashed line is a guide to the eye. Mass spectrometer and cold cathode gauge were running for all acquired samples.

starting with the appliance of the oxygen flow, the masses of O_2 and O become the dominantly detected ones (dark blue and light blue, respectively). The simultaneous increase of the other measured species can be explained by the imperfect degree of purity of the oxygen inlet gas (purity: 99.995 %). In particular contaminations of H (dark red), H_2 (light red), H_2O (violet), CO/N_2 (light green) and CO_2 (dark green) are detected. Shortly after starting heating (black dotted line) a strong increase of all detected species except O and O_2 is observed. CO and N_2 are hard to distinguish as they have similar molecular masses. Analysis of the CO/CO_2 ratio, however, indicates that mainly CO is present. We associate this strong increase on the one hand with the evaporation of the organic solvents of the Ag-paste, as it is less distinct for samples fixed without Ag-paste (Figure 4.3 a)), on the other hand evaporating adsorbates on the sample holder are responsible as well. The sample holder is the main source of adsorbates, as it is the only part that is transfered in and out of the chamber. The temperature of the chamber itself never exceeded 60 °C and it is thus unlikely that adsorbates situated at the chamber wall play a significant role.

After the initial heavy evaporation, the amount of contaminations decreases to a local minimum and oxygen becomes the dominating species again. When heating without an additional pre-annealing step (Fig. 4.2 a)) the signal slowly increases again with increasing temperature. The additional pre-annealing step at 400 °C (Fig. 4.2 b)) shifts the local minimum to a later point in time as the amount of contaminations keeps decreasing. The additional pre-annealing step, however, cannot prevent an increase of the contaminations shortly before reaching 800 °C. After reaching 800 °C (dashed lines) there is a transient decrease of contaminations towards a nearly constant value. The amount of contaminations, especially H_2 during the annealing step at 800 °C is lower for the case of an additional pre-annealing step. Although a significant amount of contaminations is measurable, O_2 and O are the dominant species with and without an applied pre-annealing step.

After remaining one hour at 800 $°C$, the samples are quenched and a Hall measurement is carried out subsequently. The resulting carrier concentration (n) for samples annealed without an additional annealing step is $\approx 2.4 \cdot 10^{18}$ cm^{-3} assuming homogeneous doping within the entire crystal (Fig. 4.2 c)). Remarkably, this carrier concentration corresponds to heavily reduced $SrTiO_3$[5]. To investigate whether the contaminations are responsible for the reduction of $SrTiO_3$ the duration of the additional pre-annealing step at 400 °C is varied. The resulting n values for different durations of the 400 °C annealing step are depicted in Figure 4.2 c). A 15 minute annealing step results in a almost two times lower n ($\approx 1.3 \cdot 10^{18}$ cm^{-3}). While still achieving a slight decrease in carrier concentration with an increase of the time towards 30 minutes ($\approx 0.9 \cdot 10^{18}$ cm^{-3}) a further increase of the pre-annealing time towards 60 minutes does not change the carrier density further.

The observed behavior is surprising, because the reduction behavior of the $SrTiO_3$ single crystals indicates a local oxygen partial pressure that is well below the physical pressure of 10^{-6} mbar. This however, seems to contradict the results of the mass spectrometry experiments revealing that oxygen is the dominant component of the gas mixture. A possible explanation for O_2 and O being the dominant species and at the same time reducing the sample is that the origin of the contaminations. The sample and its holder are the main source of contaminations, as only the sample holder is transferred from outside the chamber and the silver paste, used to fix the sample, outgasses. However, both, mass spectrometer and oxygen inlet, are not in the direct vicinity of the sample. It is thus conceivable that contaminations react with the sample before reaching the mass spectrometer. The decrease in contaminations, achieved by the additional annealing step, results in a less reduced substrate. Thus, the contaminations play a role in the enhanced oxygen vacancy formation during vacuum annealing. H and H_2[5, 6, 59] as well as CO[137] are identified as species responsible for this effect. The equilibria describing their oxidation behavior in the gas atmosphere are the following (Kroeger-Vinck-notation)[54]:

$$\mathrm{CO} + \frac{1}{2}\mathrm{O_2} \rightleftharpoons \mathrm{CO_2} \tag{4.1}$$

$$\mathrm{H_2} + \frac{1}{2}\mathrm{O_2} \rightleftharpoons \mathrm{H_2O} \tag{4.2}$$

Applying those to $SrTiO_3$ under consideration of chapter 2.1 results in:

$$\mathrm{CO} + \mathrm{O}_\mathrm{O}^{x} \rightleftharpoons \mathrm{CO_2} + \mathrm{V}_\mathrm{O}^{\bullet\bullet} + 2\mathrm{e}^- \tag{4.3}$$

$$\mathrm{H_2} + \mathrm{O}_\mathrm{O}^{x} \rightleftharpoons \mathrm{H_2O} + \mathrm{V}_\mathrm{O}^{\bullet\bullet} + 2\mathrm{e}^- \tag{4.4}$$

,which then describes the oxidation of carbon monoxide and hydrogen in the vicinity of an oxide surface. In this case, these molecules tend to remove oxygen from the solid in order to get oxidized.

At this point it was found that the contaminations present in the PLD chamber play an important role for the reduction of $SrTiO_3$. It is possible to decrease the amount of contamination present during annealing by applying an additional annealing step resulting in a less reduced $SrTiO_3$ substrate. The pre-annealing temperature of 400 °C is high enough to enable the evaporation of most adsorbates, at the same time it is, according to literature, low enough to prevent significant release of oxygen from the substrate at the chosen time scales.[7] However $SrTiO_3$ is still reduced to a greater extend than would be expected considering chemically controlled reducing atmospheres.[5, 6, 59] Thus other possible influences have to be considered.

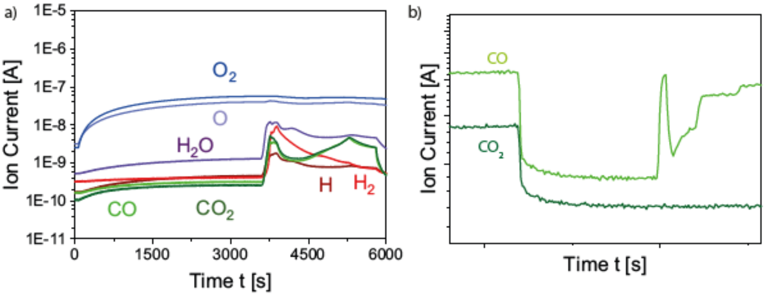

Figure 4.3: a) Mass spectrometry data during thermal annealing of $SrTiO_3$ crystals inside a PLD chamber at 10^{-6} mbar using a holder without Ag-paste. b) Mass spectrometry of the purposely induced CO mimicking the CO induced by the cold cathode gauge

Influence of measurement devices

A hint to another possible influence on the enhanced oxygen vacancy formation was recently published by Scheiderer *et al.*[138] They found an influence of the cold cathode gauge on the reduction state of $LaAlO_3/SrTiO_3$ heterostructures in H_2O rich atmospheres. They identified the cold cathode gauge to influence the ratio of H_2O and its ionic derivatives.[138] Thus the influence of similar measurement devices applied to our vacuum chamber, namely a cold cathode gauge and a mass spectrometer, was investigated.

Figure 4.4 a) depicts the carrier concentration of different $SrTiO_3$ single crystals annealed for one hour at 800 °C and 10^{-6} mbar without pre-annealing step in comparison to chemically controlled thermodynamic equilibrium data from our earlier work (black squares)[59]. The thermodynamic equilibrium data is acquired in chemically controlled reducing atmospheres. As the pressure for these experiments is constantly 1 bar neither a cold cathode gauge nor a mass spectrometer are used. In order to draw this comparison, the equilibrium conductivity data[59] is converted into the corresponding carrier concentration utilizing the mobility formula provided by Moos *et al.*[5]. These data serve as reference for the carrier density expected for $SrTiO_3$ in chemically controlled thermodynamic equilibrium. The data points represent the carrier concentration of the sample with a running cold cathode gauge and mass spectrometer (blue dot), a running cold cathode gauge (red triangle), a running mass spectrometer (green triangle), and without any of both devices running (crossed pink square).

The highest sheet carrier concentration is achieved when both measurement devices are running ($\approx 3 \cdot 10^{18}$ cm^{-3}). With only one measurement device running n is considerably smaller ($\approx 1 \cdot 10^{18}$ cm^{-3}), but, considering the equilibrium data, still in the magnitude of highly reduced $SrTiO_3$. Remarkably, when no measurement device is running during annealing, n is lower than the detection limit of the Hall probe (10^{11} cm^{-3}). The fact that the carrier concentration is even lower than the equilibrium data is easily explainable considering the measurement methods. The equilibrium conductivity data is measured at elevated temperatures, while our measurements are performed at room temperature. Considering the temperature dependence of small carrier concentrations, the corresponding data is below the threshold for n-type conduction in the quenched state (about 10^{15} cm^{-3}).[139] Therefore, it can be concluded that the sample is not reduced.

These results are surprising as they prove the attached measurement devices as being responsible for the reducing atmosphere in the vacuum chamber. A possible reason can be extracted from Figure 4.4 b). It shows again the mass spectrometry data for CO_2 (dark green), CO (light green), H_2 (light red) and H (dark red) obtained at 10^{-6} mbar. These species were identified as responsible for the reduction of $SrTiO_3$ (Eq. 4.3 and Eq. 4.4). When the cold cathode gauge is turned off (dashed line), the signals of CO_2 and CO decrease. Noticeably, the amount of CO decreases to a stronger extend than the amount of CO_2, while there is no change observable for H_2 and H. Thus the cold cathode gauge shifts the CO/CO_2 equilibrium towards the reducing CO (Eq. 4.3). This differs from the findings of Scheiderer *et al.* as

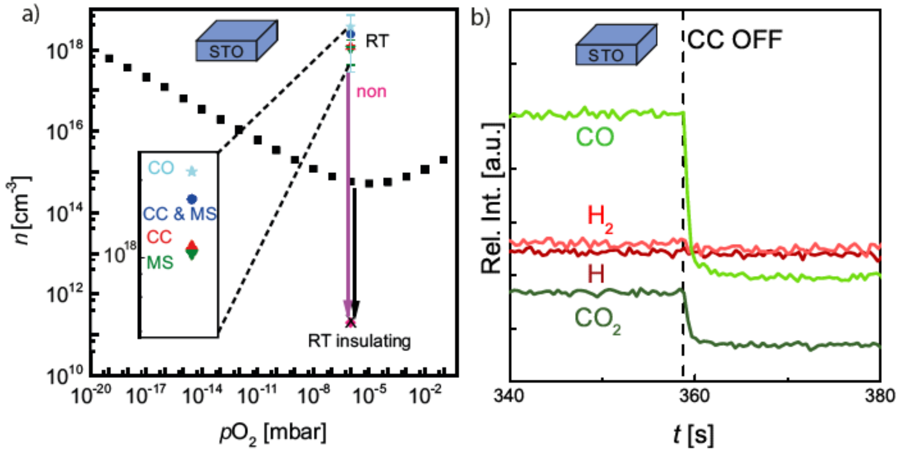

Figure 4.4: a) Resulting carrier concentrations (y-axis) for annealing one hour at 10^{-6} mbar and 800 °C with different measurement devices running. CC meaning cold cathode gauge and MS mass spectrometer, CO representing a CO/O_2 atmosphere. The error bars indicate the standard deviation of the carrier concentration measured for at least two equally treated samples, verifying the reproducibility of our results. The carrier concentration is plotted into a chemically controlled thermodynamic equilibrium graph[59] with the pO_2 as x-axis for better comparability. The inset shows details of the resulting sheet carrier concentration for different running measurement devices without the error bars. The pink arrow indicates the change for switched off measurement devices, the black arrow indicates the change for measuring at room temperature.[139] The crossed out data point indicates a sheet carrier concentration below the measurement limit. b) Relative intensity of selected ions (y-axis) over the time (x-axis) measured via mass spectrometry in the moment of the cold cathode gauge turn off (dashed line) measured at the same parameters. Dark red representing H, light red H_2, light green CO and dark green CO_2.

they found a shift in the ratio of H_2O and its derivatives. However, in contrast to this experiment they worked in H_2O rich atmospheres, which explains the different observations.[138]

To verify CO as the contamination mainly responsible for the reduction samples were annealed in a CO/O_2 mixture (turquoise star). Figure 4.3 b) shows a constant flux of CO, which is applied matching the amount of CO originating from the cold cathode gauge identified in figure 4.4 b). During the annealing the mass spectrometer and the cold cathode are switched off. Samples annealed this way show a carrier concentration in the same regime as samples with both the measuring devices switched on ($\approx 3 \cdot 10^{18}$ cm^{-3}). The surplus of CO originating from the cold cathode gauge is thus likely to be responsible for the reduction of $SrTiO_3$ at comparably high oxygen pressures.

Both measurement devices work based on ionization. This working principle is likely to be responsible for the shift of the CO/CO_2 ratio towards CO. According to Eq. 4.1 this results in a lowered effective oxygen partial pressure $pO_2 \sim \frac{pCO_2}{pCO}$. As a result of Eq. 4.3 one then expects a stronger reduction of the $SrTiO_3$ crystal when exposed to this atmosphere. Additionally it is conceivable that the ionization can influence the kinetics of the redox reaction at the sample surface in a way that the removal of oxygen from the sample gets favorable.[56] In conclusion the cold cathode and mass spectrometer are primarily responsible for the unexpected reduction of $SrTiO_3$ at relatively high oxygen pressures; probably due to their working principle, which is based on ionization. Their influence outweighs the influence of the contaminations found in figure 4.2, as it is possible to avoid reduction even without an additional annealing step. This is perspicuous considering the contaminations change the carrier concentration by a factor of three, while the measurement devices eventually change the carrier concentration by at least 6 tens of magnitude.

Reduction during PLD

After having addressed the reduction behavior of $SrTiO_3$ upon vacuum annealing, here the possible implications for actual PLD growth processes are discussed. For this $LaAlO_3$ is grown on $SrTiO_3$ as this results in a very p_{ox} sensitive system (see chapter 2.2). To unravel whether the reduction of the $SrTiO_3$ substrate during $LaAlO_3$ growth is triggered by the measurement devices, as it is for mere thermal annealing, or by the deposition itself[80, 85, 103, 132, 135] 8 monolayers of $LaAlO_3$ are deposited on $SrTiO_3$ with and without an applied cold cathode gauge. The mass spectrometer was not applied in any case. The black squares in the left panel of Figure 4.5 a) represent the resulting sheet carrier concentration of the $LaAlO_3/SrTiO_3$ heterostructure quenched after deposition with and without applied cold cathode gauge. For both cases the sheet carrier concentration is $\approx 6.1 \cdot 10^{16}$ cm^{-2} and thus in the regime of bulk contribution (compare chapter 2.2).

As the application of the cold cathode gauge does not influence the resulting sheet carrier concentration for samples quenched directly after deposition its influence during depositions is neglectable. The influence of the plasma plume and the oxidization of the grown film *via* the substrate, respectively, dominate the reduction of the $SrTiO_3$ substrate.

In an earlier work it was shown that it is possible to re-oxidize the $SrTiO_3$ substrate reduced during growth by annealing after deposition for a sufficient time at growth conditions for pressures $\geq 10^{-4}$ mbar (Figure 4.5 b)).[35] Until now this was not possible for lower pressures. As it was shown in this chapter that the cold cathode gauge has a crucial influence on the reduction state of $SrTiO_3$ for thermal annealing, its influence during the post-annealing process is investigated and the re-oxidization of the $SrTiO_3$ substrate at lower pressures is attempted.

The red squares in the left panel of Figure 4.5 a) represent the resulting sheet carrier concentration when annealing for 1 h at deposition conditions with and without applied cold cathode gauge. The annealing time of 1 h ensures, as before, a diffusion length exceeding the sample dimensions.[7] The temperature of 800 °C further allows the exclusion of a surface reaction limitation.[136] While there is no change of the sheet carrier concentration when the cold cathode gauge is applied ($\approx 6.1 \cdot 10^{16}$ cm^{-2}), post-annealing without an applied cold cathode gauge results in a decrease of the sheet carrier concentration ($\approx 1.6 \cdot 10^{16}$ cm^{-2}). This value, however, still corresponds to a contribution from the bulk conduction of the reduced $SrTiO_3$ substrate.[130, 131]

To elucidate the extend of reoxidization the sheet carrier concentrations are compared to the prior annealing experiments in Figure 4.5 b).[35] Although reoxidization takes place to certain extend at 10^{-5} mbar, when the cold cathode gauge is not applied, the $SrTiO_3$ substrate is far from complete reoxidization. Working with pressures $p \geq 10^{-4}$ mbar, however, eventually results in a complete reoxidization.[35] The explanation for this discrepancy is that for $p \leq 10^{-5}$ mbar reoxidization is hindered by a lack of oxygen species reaching the sample surface. In opposite to oxidation in chemically controlled atmospheres, where oxygen is constantly delivered *via* an

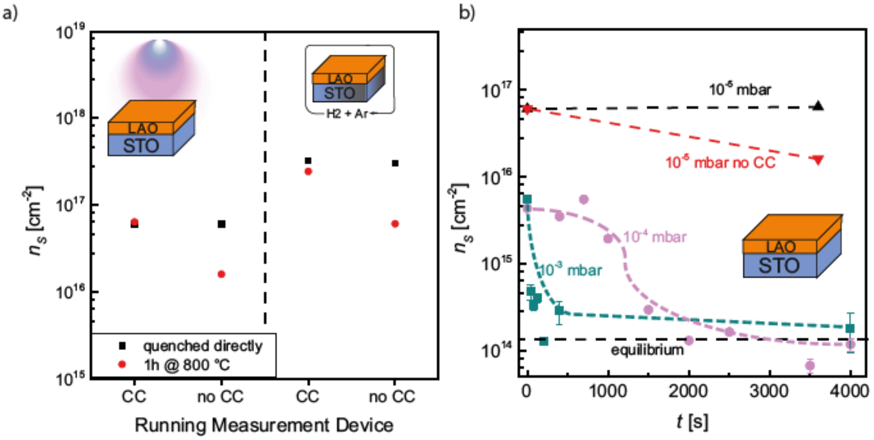

Figure 4.5: a) Sheet carrier concentration of $LaAlO_3/SrTiO_3$ heterostructures for the case of a running cold cathode gauge (CC) and a turned off one, respectively. The left panel shows the sheet carrier concentration (n_S) of $LaAlO_3/SrTiO_3$ grown at 10^{-5} mbar, when quenched directly after deposition (black) and subsequently annealed for one hour (red). The right panel shows n_S of $LaAlO_3/SrTiO_3$ samples, which were ex situ reduced in equilibrium experiments (black) and subsequently annealed in the PLD chamber under the same conditions as the grown ones (red). b) depicts the annealing experiments at 10^{-3} mbar (turquoise) and 10^{-4} mbar (pink), respectively. The results of our annealing experiments at 10^{-5} mbar with cold cathode (CC) (black) and without cold cathode (red) are included for comparison. The dashed black line marks the expected sheet carrier concentration for 2D interface conduction.

equilibrium, the oxygen consumption of the reoxidization of the $SrTiO_3$ in vacuum chambers is not compensated adequately.

To verify that oxidization is hindered by a lack of oxygen species reaching the sample surface *ex-situ* reduced samples were annealed. This allows us to exclude lasting influences of the deposition on the substrate like induced cation defects or the creation of a chemically broad interface.[103, 140, 141]

For this purpose $LaAlO_3$ thin films were grown on $SrTiO_3$ at oxidizing conditions ($p = 10^{-2}$ mbar) to avoid a reduction of the $SrTiO_3$ substrate.[22, 35] Subsequently the samples were reduced in *ex-situ* equilibration experiments for 90 minutes at 1000 °C and $p_{\mathrm{Ox}} \leq 10^{-20}$ mbar. The p_{Ox} for *ex-situ* reduction is adjusted by a 4 % H_2/Ar mixture resulting in a shift of the equilibrium described by Eq.4.2 and Eq.4.4. This shift, eventually, results in a highly reducing atmosphere.

The sheet carrier concentration resulting from the *ex-situ* reduction is represented by the black squares in the right panel of Figure 4.5 a) ($3.1 \cdot 10^{17}$ cm^{-2}). The *ex-situ* reduced samples are subsequently annealed inside the PLD chamber for 1 h at 10^{-5} mbar and 800 °C with and without applied cold cathode gauge. These parameters ensure comparability with the prior experiments. The resulting sheet carrier concentration is represented by the red dots in the right panel of Figure 4.5 a). While, again, there is nearly no change for the sample with an applied cold cathode gauge ($\approx 2.4 \cdot 10^{17}$ cm^{-2}), reoxidization is observed for the sample annealed without an applied cold cathode gauge ($\approx 0.6 \cdot 10^{17}$ cm^{-2}).

The sheet carrier concentrations of the *ex-situ* ($\approx 6.1 \cdot 10^{16}$ cm^{-2}) and *in-situ* ($\approx 1.6 \cdot 10^{16}$ cm^{-2}) reduced samples, which were subsequently annealed for 1 h without an applied cold cathode gauge, differ significantly. This proves that the reached state is not the result of lasting deposition effects, but the result of a lack of oxygen species reaching the sample surface during post-annealing and thus hindering a complete reoxidization. These experiments also underline the severe influence of the cold cathode on the reduction state of the $SrTiO_3$ substrate, as annealing for 1 h with an applied cold cathode gauge leads to no reoxidization at all.

Discussion and conclusion: Enhanced oxygen vacancy formation at low pressures

To summarize, the discrepancy of the oxygen pressure required to achieve reduction of $SrTiO_3$ single crystals found in literature, when comparing vacuum annealing and annealing in chemically controlled reducing atmospheres, was unraveled. The residual gases present in vacuum processes play a minor role, as it is possible to decrease the level of reduction by decreasing the amount of contaminations. More important, the reduction of $SrTiO_3$ mainly originates from the attached measurement devices, namely a cold cathode pressure gauge and a mass spectrometer. Both devices are based on ionization. The ionized species on the one hand shift the CO/CO_2 equilibrium to the reducing CO and on the other hand accelerate the surface redox reaction. These effects in combination enable the reduction of $SrTiO_3$ at pressures as high as 10^{-6} mbar. As soon as the devices are not attached no reduction takes place.

However, during depositions the attached measurement devices lose in importance as the reduction triggered by the deposition dominates the reduction state of the $SrTiO_3$ substrates. During post-annealing at pressures $\leq 10^{-5}$ mbar samples are only reoxidized, if no measurement device is attached. The $SrTiO_3$ substrate is, however, not completely reoxidized, even without an attached cold cathode gauge due to a lack of oxygen species reaching the sample surface and thus hindering a complete reoxidization.

Thus further understanding of oxidization/reduction during PLD processes at low oxygen pressures was provided and the contradiction concerning the reduction of $SrTiO_3$ substrates during deposition and its well known defect equilibrium was eliminated. The recommendation is to consider the role of the cold cathode, when post-annealing samples during PLD processes. Moreover it should also be considered for other thermal annealing processes carried out in vacuum chambers.

4.1.2 UV-radiation of the plasma plume

In this section another parameter with an influence on the formation of oxygen vacancies in $SrTiO_3$, that has up to this point been neglected will be investigated: the UV-radiation of the plasma plume during PLD. While the effect of impinging species from the PLD plasma plume has been studied,[80, 88, 128] the possible effect of UV-radiation emitted by the plume has not been considered, although the plasma plume is known to emit UV-radiation.[4] Further UV radiation is known to induce persistent photo conductivity,[57, 58] as well as to enhance the oxygen incorporation rate,[56, 142–145] in $SrTiO_3$.

One obstacle with respect to evaluate the influence of UV-radiation during PLD growth is the problem of separating its influence from that of the impinging species within the plume. In order to allow such a separation, a new sample holder was designed, allowing UV-radiation to reach the sample, but not the impinging species.

$SrTiO_3$ samples are processed in this new holder at typical low pressure PLD conditions, one sample with an ignited plume and, as a reference, one without. Hall measurements show an increase in charge carrier concentration in $SrTiO_3$ samples exposed to the plume UV-radiation, compared to the reference sample. Cross sectional scanning Kelvin probe microscopy (SKPM) measurements revealed a difference in the carrier concentration profile between the two samples. Variable energy positron annihilation lifetime spectroscopy (VEPALS) measurements detect Ti vacancy - oxygen vacancy complexes ($V_{Ti}V_O$) in the near-surface region of both types treated $SrTiO_3$ samples.

The first step towards an understanding of the role of UV radiation during PLD processes is to determine, whether UV radiation is emitted. The UV-spectrum of the plasma plume resulting from the PLD ablation of a $SrTiO_3$ target is simulated using *Saha-LTE* by collaborators at the *Chair for Technology of Optical Systems, RWTH Aachen University*. To obtain the ionization levels from the *NIST* atomic spectra database needed for this simulation the electron temperature and density in the plasma plume are required.[146] The electron temperature (kT) in the plasma plume can be derived from the power density of the used ablation laser, $(1 \pm 0.5) \times 10^8 \frac{\mathrm{W}}{\mathrm{cm}^2}$, using the corresponding equation by Schriever *et al.*[147], to be 0.885 ± 0.135 eV. The electron density in the plasma plume is estimated to be $\approx 1 \times 10^{18}$ cm^{-3} as given by Gilgenbach *et al.*[148]. The simulated UV-radiation spectrum of the plasma plume resulting from ablation of an $SrTiO_3$ target is shown in Figure 4.6 a). Strong emission lines at $\approx$ 215 nm due to strontium are observed, and will contribute considerable intensity to the emitted UV radiation.

The sample holder designed for this study is shown in Figure 4.6 b), the laser plume is blocked by a sapphire window which is transparent to UV-radiation $\geq$ 150 nm.[149] The $SrTiO_3$ sample is separated from the window by four 1 x 1 x 0.5 mm^3 $SrTiO_3$ spacers, this exposes the sample surface to a gas exchange volume. The $SrTiO_3$ sample is mounted into the holder with a Ni-foil placed between the rear of the sample and a second sapphire window. The foil acts as an absorber for the infrared diode laser heater which provides precise control of the sample temperature. The back sapphire window enables transmission of the IR-radiation and prevents the ablation of the Ni-foil. Finally a spacer is placed between the second window and the holder frame to tighten the whole stack and improve heat transfer.

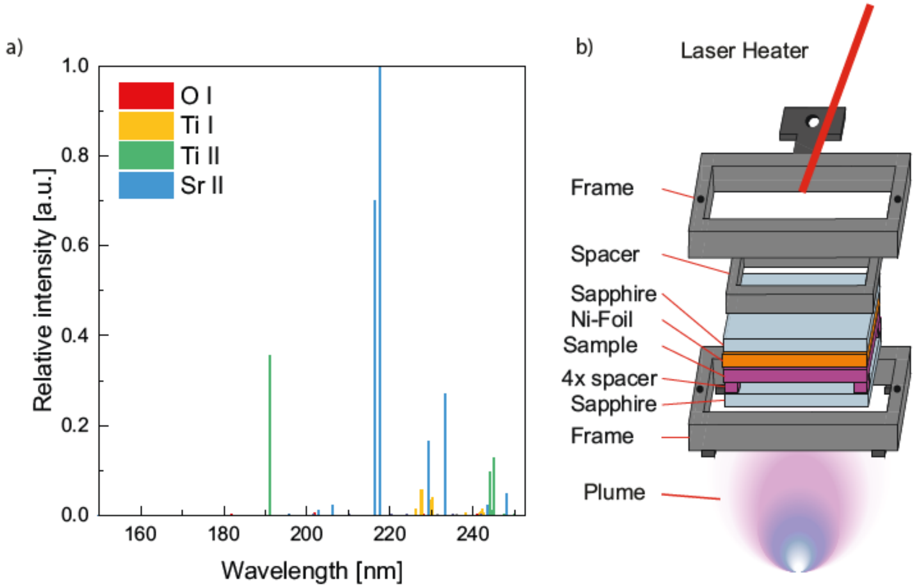

Figure 4.6: a) Simulated spectra in the UV regime for a $SrTiO_3$ plasma plume. b) Sample holder designed to separate the influence of the UV-radiation and the impinging species from the plasma plume during PLD. The front sapphire window is transparent to UV-radiation, but prevents the ablated atomic and molecular species of the plume from reaching the $SrTiO_3$ sample.

Experiments were performed on TiO_2-terminated $SrTiO_3$ samples heated to 800 °C and in chamber pressure of 10^{-5} mbar oxygen for one hour. The sample temperature is rapidly quenched to room temperature by switching off the laser heater (cool down time $\approx$ 65 s). These are typical conditions for low pressure growth of oxide thin films, for which was shown in section 4.1.1 that no reoxidization appears even after one hour.[79] At the same time, quenching preserves as best as possible the defect state obtained immediately after the growth, and, hence allows to decouple growth phenomena from thermodynamic phenomena, such as re-oxidation kinetics.[35] The effect of the UV-radiation from the plasma plume was then investigated by ablating the $SrTiO_3$ single crystal target with a 5 Hz pulse repetition rate. Laser ablation was maintained for the 1 h period. Samples were prepared with and without the presence of the laser plume.

Table 4.1: Sheet carrier concentration calculated from Hall effect measurements for low pressure annealed UV-irradiated and non-UV-irradiated $SrTiO_3$ single crystal samples. The samples were measured immediately after processing and after a further 50 day storage in air. The error indicates the standard deviation obtained from measuring at least four equally treated samples.

Sample	n_S (immediate)	n_S (50 d)
UV irradiated	$(5 \pm 1) \times 10^{17}$ cm^{-2}	$(5 \pm 1) \times 10^{17}$ cm^{-2}
Non UV irradiated	$(2 \pm 0) \times 10^{17}$ cm^{-2}	$< 10^{10}$ cm^{-2}

The sheet carrier concentration, n_S, of the processed $SrTiO_3$ samples, with and without exposure to UV-irradiation, were measured using a Hall measurement system (compare chapter 3.4). Measurements were performed immediately following processing and after 50 days of storage in air for at least four equally treated samples. The averaged results including the standard deviation are shown in Table 4.1. Both the UV-irradiated and the non-irradiated samples exhibit a high sheet carrier concentration immediately after preparation. It is well known that annealing of $SrTiO_3$ at 10^{-5} mbar can result in the reduction of the samples, as shown in section 4.1.1.[22–24, 79] The sheet carrier concentration of the UV-irradiated samples, however, is approximately twice that of the non-irradiated samples immediately after processing. More strikingly, after 50 days the difference between the two types of samples becomes marked. The sheet carrier concentration of the UV-irradiated samples is unchanged, while the concentration in the non-irradiated samples has fallen below the measurement limit ($< 10^{10}$ cm^{-2}).

A similar behavior was observed for samples treated at different oxygen pressure. Samples processed at 10^{-4} mbar oxygen showed the same behavior as samples processed at 10^{-5} mbar with a 50 % lower sheet carrier concentration. Samples processed at 10^{-6} mbar showed an increased carrier concentration and no time dependence during storage in air. It can thus be assumed that their whole bulk was reduced. Samples processed at 10^{-3} mbar, however, showed no signs of reduction, which is in accordance with previous results.[35] In the following exemplary the samples processed at 10^{-5} mbar will be discussed as they show the most pronounced differences between irradiated and non-irradiated samples, while having a high initial sheet carrier concentration.

In order to deliminate the results from conductivity contributions generated by photo-induced carriers only, reference experiments were carried out at room temperature and 10^{-5} mbar, where photo-induced carriers may be generated by UV irradiation, while the kinetics of ionic defect formation limits the photo-induced formation of oxygen vacancies to the very-surface region. This is of high interest, as a reduction of $SrTiO_3$ is commonly also observed for room temperature depositions.[88, 150] However no reduction of the substrates was observed without the presence of impinging species.

The higher sheet carrier concentration and its persistence after 50 days storage provide evidence that the $SrTiO_3$ sample's defect structure, in particular the oxygen vacancy concentration, is altered significantly by the UV-irradiation from the plasma plume during low pressure processing.

The question arises, whether the carrier concentration is homogeneously distributed through the volume of the sample, or if a concentration gradient exists.

To investigate the depth dependence of the carrier concentration cross-sectional SKPM measurements were performed 10 days after processing by collaborators at the *University of Massachusetts*. The results are shown in Figure 4.7. Figure 4.7 a) shows the topography image for orientation (top) and the surface potentials for the UV irradiated sample (center) and the non-UV-irradiated sample (bottom). With the help of the surface potentials the local carrier concentration can be determined, Figure 4.7 b).[151] The carrier concentrations near the surface for the UV-irradiated and non-irradiated samples are comparable, however, while the UV-irradiated sample exhibits a very shallow depth profile, the non-irradiated sample exhibits a rapid decrease within the first 4 μm. In consequence, it can be inferred that the oxygen vacancy concentration profile resulting from low pressure annealing with UV-irradiation is markedly different from that for the samples similarly annealed but not exposed to UV-irradiation.

The observation from the non-UV-irradiated samples that the sheet carrier concentration decreased below the measurement limit after 50 days (Table 4.1) is consistent with the restriction of the initial carrier profile to the top few microns (Figure 4.7 b)). Using the oxygen-vacancy diffusivity determined for $SrTiO_3$ by De Souza *et al.*[7], it is found that after 50 days at room temperature the diffusion length of oxygen vacancies is ≈ 10 μm. In consequence, the low pressure annealed sample not exposed

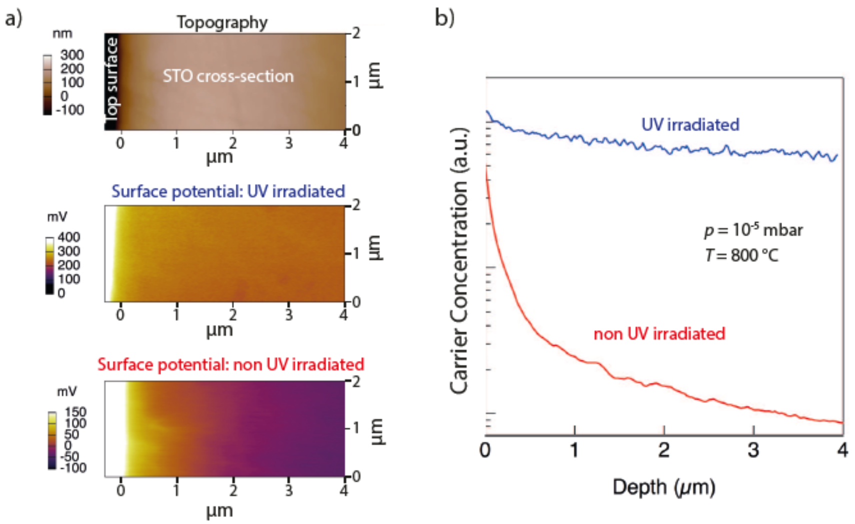

Figure 4.7: a) The surface potentials below the $SrTiO_3$ surface (0 μm) measured by cross sectional SKPM including a topography image for orientation. b) The local carrier concentration with depth below the $SrTiO_3$ surface determined *via* the surface potential. Samples exposed to UV-irradiation during low pressure anneal (blue), and samples low pressure annealed but without UV exposure (red).

to UV-irradiation can re-oxidize, returning to the insulating state, while the near constant depth dependent concentration of the UV-exposed sample is not detectably altered.

To gain further insight on the defect content of the near surface region of the samples VEPALS measurements were performed by a collaborator from the *University of Dundee* using the *PLEPS instrument* on the neutron induced positron source (NEPOMUC) beamline at the *Heinz Maier-Leibnitz Zentrum Munich* research reactor.[152, 153] The spectra were best fitted using three positron lifetime components, a reduced bulk lifetime and two vacancy-related defect components. The defect component results for positron implantation energies between 10 keV and 18 keV, which correspond to mean implantation depths varying between approximately 300 to 800 nm, are shown in Figure 4.8. The first lifetime component corresponds to the

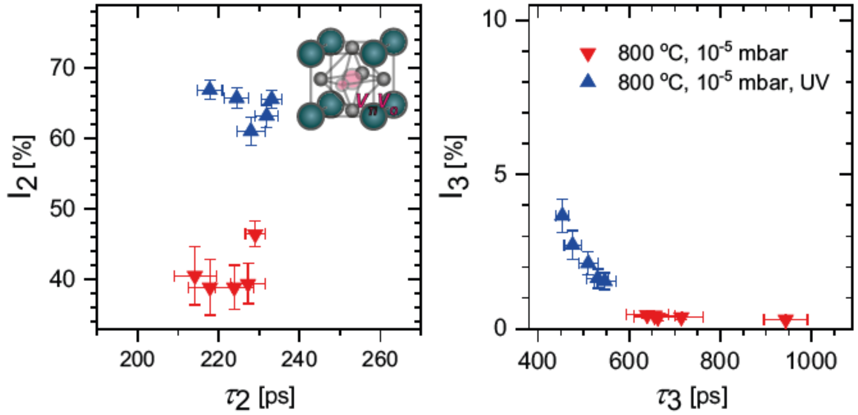

Figure 4.8: The two defect components obtained from three lifetime component free fits of the PALS spectra for positron implantation energies between 10 and 18 keV for a sample exposed to UV-irradiation during low pressure anneal (up triangle, blue), and a sample annealed but without UV exposure (down triangle, red). The inset shows a $V_{Ti}V_O$ vacancy complex.

bulk and is thus not further considered. The second lifetime component was found to be approximately 225 ± 6 ps, this is in good agreement with the density functional theory (DFT) calculated value for the Ti-vacancy oxygen vacancy complex, $V_{Ti}V_O$, of 225 ps.[154] A significant increase in trapping to this defect was observed for the UV-irradiated low pressure annealed sample, compared to the sample annealed without UV-irradiation (samples stored in air for > 50 days). The oxygen monovacancy is normally expected to be positively charged and hence not to trap positrons.[155] The lifetime of the Ti vacancy in $SrTiO_3$ is approximately 180 ps, while that for the Sr vacancy is 280 ps.[155] The increase in the intensity of the $V_{Ti}V_O$ lifetime component observed here (Figure 4.8) can only result from either an increase in the defect trapping coefficient, which would require a change of the charge state of the defect to a more negative value, or from an increase in the concentration of defects in the low pressure annealed sample exposed to UV-irradiation compared to the non-UV-irradiated sample. An increase in the concentration of $V_{Ti}V_O$ defects is thus consistent with an increase in the oxygen vacancy concentration in the UV-exposed sample.

Figure 4.8 also shows the results for the third lifetime component, this has negligible value for the non-UV-irradiated sample, but there is evidence of trapping to a vacancy cluster defect with an approximate lifetime of 500 ± 40 ps in the UV-exposed sample. Positron trapping vacancy cluster defects involved on the order of 10-20 vacancies have been previously observed in $SrTiO_3$ thin films.[106] Trapping to vacancy cluster defects in the UV-exposed sample supports the presence of an increase in oxygen vacancy defects compared to the non-UV-exposed sample.

Discussion and conclusion: UV-radiation of the plasma plume

Considering all the results described above a mechanism by which the UV radiation of the plasma plume influences $SrTiO_3$ is proposed. The VEPALS measurements observe an increase in positron trapping to oxygen vacancy containing vacancy complexes providing indirect evidence that an increase in oxygen vacancy concentration is responsible for the increase in conductivity. The very different depth dependent carrier concentration profiles obtained from the cross sectional SKPM provide further evidence for the presence of much higher concentration of oxygen vacancies within the volume of the UV irradiated sample compared to the non-UV-irradiated sample. The temperature and pressure environment for both samples was equal. Further the formation of interstitials in $SrTiO_3$ can be excluded restricting the formation of oxygen vacancies to the surface.[6] Hence it is concluded that the UV irradiation enhances the oxygen vacancy incorporation rate at the surface. The oxygen vacancy incorporation can be described by Equation 4.5[5–7, 59] in the Kroeger-Vink notation[54] as already described in chapter 2.1.

$$\mathrm{O}_\mathrm{O}^{x} + 2\mathrm{h}^{\bullet} \rightleftharpoons \frac{1}{2}\mathrm{O}_2 + \mathrm{V}_\mathrm{O}^{\bullet\bullet} \tag{4.5}$$

In the same way the incorporation of oxygen can be described by Equation 4.6[5–7, 59] in the Kroeger-Vink notation[54].

$$\frac{1}{2}\mathrm{O}_2 + \mathrm{V}_\mathrm{O}^{\bullet\bullet} + 2\mathrm{e}^{-} \rightleftharpoons \mathrm{O}_\mathrm{O}^{x} \tag{4.6}$$

The incorporation of oxygen (Equation 4.6) in reality is a multi step reaction including the adsorption of molecular oxygen, electron transfer, O-O bond dissociation and incorporation of atomic oxygen into oxygen vacancies. However, in the case of sufficient oxygen vacancies being present the electron transfer is considered as the rate limiting step.[17, 56] Considering this, the known UV-enhanced oxygen incorporation rate for $SrTiO_3$ is under consideration of Equation 4.6 explained by additional electrons provided by the electron hole generation of the UV radiation (Equation 4.7).[56, 142–144]

$$nil + hv \rightarrow \mathrm{e}^{-} + \mathrm{h}^{\bullet} \tag{4.7}$$

In a similar fashion the hole transfer can be considered the rate limiting step for the incorporation of oxygen vacancies (Equation 4.5) in case of sufficient lattice oxygen being present. Considering Equation 4.7 the enhanced oxygen vacancy incorporation can be attributed to the generation of additional holes by the UV radiation. Consequently the persistent photo conductivity in $SrTiO_3$, which has been discussed in literature controversially,[58] can be explained by an increased oxygen vacancy incorporation rate triggered by the generation of additional holes. Considering Equations 4.5, 4.6 and 4.7 not only the oxygen vacancy incorporation can be explained by the UV irradiation of the plasma plume, observed in our experiments, but equally the enhanced oxygen incorporation in presence of the plasma plume reported in literature can be explained.[156, 157] This in turn explains, why no UV induced reduction was observed at 10^{-3} mbar. The absence of conductivity for samples processed at room temperature may be explained by the reoxidization of the UV induced oxygen vacancies upon air exposure, as they are restricted to the surface due to the limited kinetic at such temperatures.[158] It further shows that the holes and electrons generated by the UV radiation of the plume are not persistent and thus do at best introduce perishable conductivity. Only if they participate in the chemical reduction of the sample persistent photo conductivity seems observable.

In this section the influence of the UV-irradiation accompanying the PLD laser plume on the oxide sample was investigated. UV-exposed samples exhibited a high carrier concentration that was nearly constant with both depth and time. By contrast the non-UV-exposed $SrTiO_3$ samples showed a carrier concentration that decreased strongly with depth and time. The results suggest that the oxygen vacancy concentration is higher and that the profile with depth is markedly shallower in the UV-exposed samples compared to the non-UV-irradiated samples. The depth dependent positron lifetime measurements detect an increase in trapping to $V_{Ti}V_O$ divacancies in the UV-exposed sample consistent with an increased oxygen vacancy concentration. It was shown that the UV radiation emitted by the plasma plume during pulsed laser deposition of oxide thin films plays a key role for their properties. The mechanism behind this was identified as a UV enhanced oxygen vacancy incorporation rate, thus also providing an explanation for persistent photo conductivity in $SrTiO_3$ reported in literature. The UV radiation of the plasma plume was identified as a key influence factor on the redox-processes relevant for the oxidization state of oxide thin films and the underlying substrate during PLD.

4.1.3 The termination layer

Besides the mentioned influence of the oxygen vacancy concentration on $SrTiO_3$, a second central parameter is its termination. As mentioned in chapter **??** $SrTiO_3$ can either be TiO_2- or SrO-terminated. In this chapter the interplay of these two influences, oxygen vacancies and termination, will be investigated. The termination of $SrTiO_3$especially plays a key role for applications, which rely on interfaces. Examples are the properties of magnetic heterojunctions,[159] interface dependent superconductivity,[160] and the formation of a two dimensional electron gas (2DEG), as observed at the interface of the model system $LaAlO_3/SrTiO_3$.[18, 22, 25, 34, 76, 78, 83, 86, 88]

Although a strong termination dependence of the oxygen exchange kinetics has been demonstrated for other perovskites,[161–163] it has only been scarcely considered for $SrTiO_3$(100).[7, 164] In this section the role of the $SrTiO_3$ termination on the oxygen exchange kinetics will be thoroughly investigated and a new method to control the oxygen exchange will be presented. This new method will be applied to amorphous and crystalline $LaAlO_3/SrTiO_3$. In the course of this the ambient stability of the $SrTiO_3$termination will be investigated.

Interplay of termination and oxygen vacancy incorporation

In order to investigate the termination dependent oxygen vacancy incorporation, $SrTiO_3$ single crystals were SrO- and TiO_2-terminated selectively. Details on the termination process can be found in chapter 3. For the *in situ* annealing process samples were annealed under oxidizing conditions after termination to minimize adsorbates. Subsequently the annealing experiment was performed for 1 h at an oxygen pressure of 10^{-6} mbar at 800 °C with subsequent quenching (cool down time to below 400 °C was about 40 s). The *ex situ* samples were stored at room temperature under ambient conditions for 60 h before being exposed to the same annealing conditions.

Figure 4.9 a) shows the resulting carrier concentration n, which is a measure for the oxygen vacancy concentration, for TiO_2 and SrO terminated $SrTiO_3$ (red square). The resulting carrier concentration for the TiO_2 terminated sample is 5×10^{18} cm^{-3}, a typical value observed for the applied conditions.[23, 79] The carrier concentration of the SrO terminated sample after the same treatment is, however, below the measurement limit ($< 10^{10}$ cm^{-3}). This is a first hint to a termination dependency of the oxygen vacancy formation.

The observed behavior, however, changes drastically after SrO terminated $SrTiO_3$ was exposed to ambient conditions for 60 h. The annealing of *ex situ* samples results in high carrier densities independent of the termination (blue triangles). Ambient storage thus affects the reduction of SrO-terminated $SrTiO_3$, while the carrier concentration of TiO_2-terminated $SrTiO_3$ remains unchanged.

Concomitant to the reduction behavior of SrO-terminated $SrTiO_3$, also the topography changes, when exposed to ambient conditions . Figure 4.9 c) shows the topography of an *in situ* annealed sample and figure 4.9 b) shows the topography of the same sample, but stored 60 h in ambient. While the vicinal surface is atomically flat in the beginning, features of about 0.2 nm height decorating the unit cell step terraces after ambient storage can be observed. The topography of TiO_2-terminated $SrTiO_3$ showed no change after ambient storage.

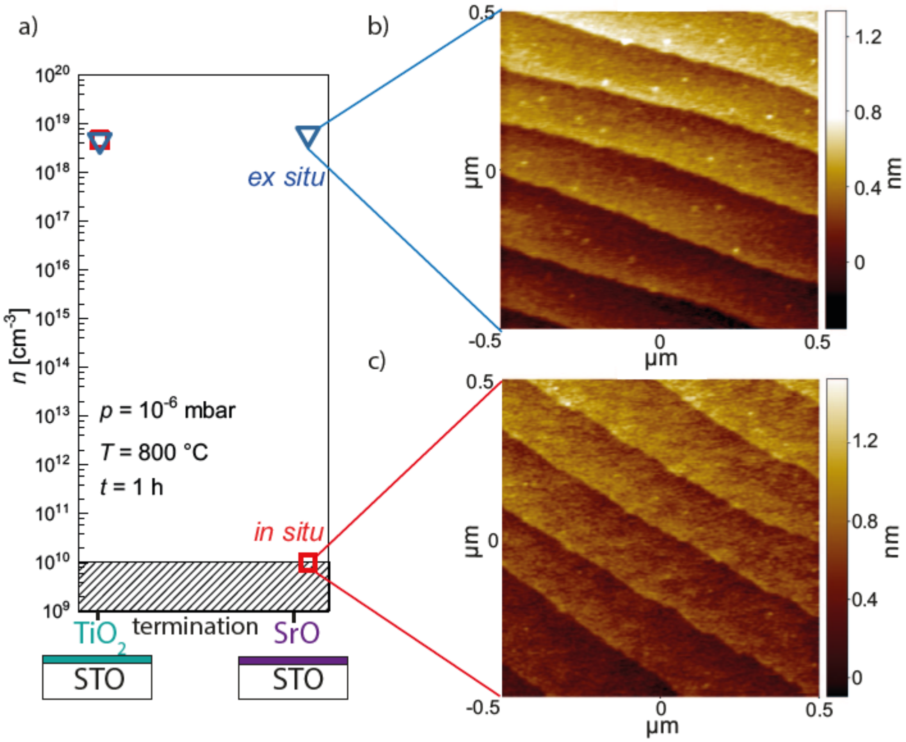

Figure 4.9: a) Carrier concentration of TiO_2 terminated (left) and SrO terminated (right) $SrTiO_3$ after 1 h of annealing at 10^{-6} mbar oxygen pressure and 800 °C for an *in situ* sample (red) and a sample stored 60 h in air (blue). b) the topography of the SrO terminated sample after 60 h of air storage and c) the topography of a SrO terminated sample measured *in situ* before storage in air. The topography in b) was measured for the sample presented in c), after that sample was exposed to air for 60 h.

Stability of the SrO termination

The changes of the surface configuration during exposure to ambient conditions were further investigated using *in situ* and *ex situ* XPS in order to investigate the surface chemistry before and after ambient exposure. The C 1s (Figure 4.10 top), O 1s (Figure 4.10 center) and Sr 3d spectra (Figure 4.10 bottom) were recorded. The C 1s spectrum is of interest as exposure to ambient is expected to give significant rise to adventitious carbon.[165, 166] The O 1s and Sr 3d spectra are of interest to probe chemical changes in the SrO termination layer. The center and right column show the comparison of the spectra before (*in situ*) and after (*ex situ*) exposure to the ambient for a SrO and a TiO_2-terminated sample, respectively.

The fits in the left column of Figure 4.10 are representatively depicted for the SrO-terminated sample and were obtained in the same manner for the TiO_2-terminated sample. The chemical information is gained from these fits. The comparisons in the center and right column elucidate the differences occurring for both terminations before and after exposure to the ambient. The C 1s spectra (Figure 4.10 a)) are fitted with a carbonate component for the highest binding energy (E_B) and a hydrocarbon component ($E_B \approx 286$ eV). The O 1s spectra are fitted using 4 components (Figure 4.10 b)). The lowest E_B component represents metal oxide bonds in the $SrTiO_3$ bulk. The highest E_B component represents carbonates.[167–169] Both of the intermediate E_B can be ascribed to hydroxides and other non-carbonate contaminations, and are referred to as contaminations peaks. The Sr 3d spectra are composed of a doublet from the $SrTiO_3$ bulk and a second, surface-related doublet at higher binding energies, as is typically observed for $SrTiO_3$ (Figure 4.10 c)).[170]

In order to estimate changes of the surface stoichiometry, the peak areas of the different core-levels are compared. In case of the C 1s spectra the area ratio of the C 1s and Sr $3p_{3/2}$ peaks (Figure 4.10 d) and g)) are used to obtain a C/Sr ratio. Further the area of the carbonate and the hydrocarbon peak are used to obtain a relative carbonate contribution. For the O 1s spectra, the areas of the carbonate and the contamination peaks in relation to the metal oxide peak are used to obtain a relative carbonate contribution and a non-carbonate contamination concentration, respectively. The relative contribution of the Sr related surface component to the Sr 3d signal is obtained from the ratio of the doublet at high binding energy and the doublet from the bulk $SrTiO_3$.

These ratios can be found in Table 4.2 for SrO and TiO_2-terminated samples, measured *in situ* and after 60 h of ambient exposure (*ex situ*). After air exposure, the C/Sr ratio increases markedly, to 40%, for both, TiO_2- and SrO-termination. For both samples there is no discernible C 1s carbonate component, when measuring *in situ*. Ambient exposure gives rise to this component, 3.0% for the TiO_2-termination

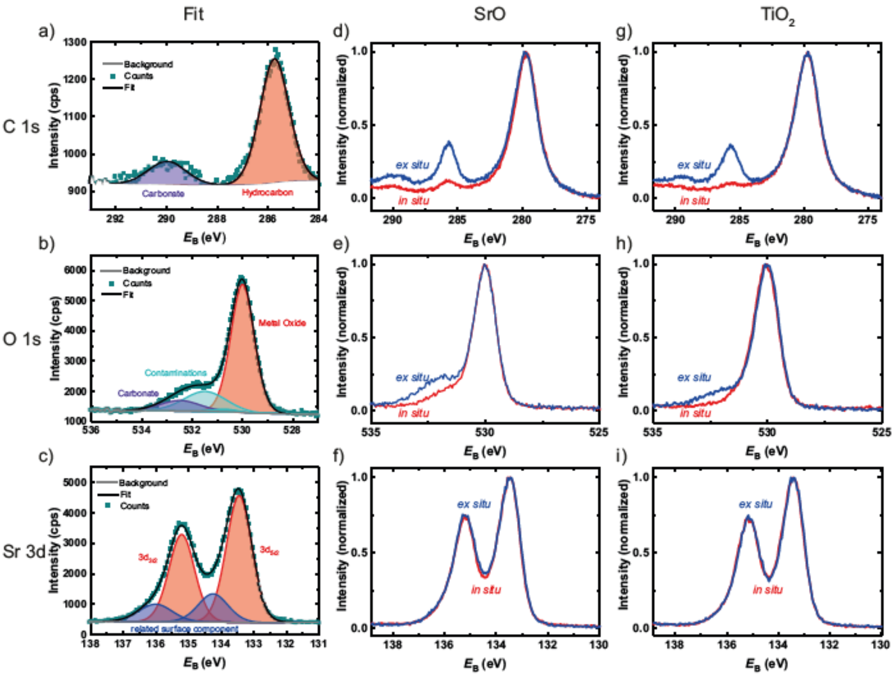

Figure 4.10: Left column shows the fits for a) the C 1s, b) O 1s and c) Sr 3d spectra. The center column shows the comparison of normalized spectra before (*in situ*), blue, and after (*ex situ*), red, ambient exposure for a SrO-terminated sample, the right column for a TiO$_2$-terminated sample, respectively. For the C 1s spectrum the change by ambient exposure is more significant for the d) SrO-terminated sample than the g) TiO$_2$-terminated sample. The same is observed for the SrO- e) and TiO$_2$-termination h) for the O 1s spectrum and the Sr 3d spectrum, f) and i), respectively.

and 6.5% for the SrO-termination. The carbonate component is thus markedly the highest for an ambient exposed SrO-termination. Similarly, the O 1s spectra do not exhibit a carbonate component when measuring *in situ*, but after exposure to ambient, this component is 7.5% for the TiO$_2$-termination and 9.5% for the SrO termination. Again the carbonate component is thus the most pronounced for an ambient exposed SrO-termination. The 3d surface component of the Sr 3d spectra is 18% for the TiO$_2$-termination *in* and *ex situ* and for the *in situ* SrO-termination. Ambient exposure of the SrO-termination increases this spectral weight (21%). This means that the 3d surface component of the Sr 3d spectra only changes after ambient exposing the SrO-terminated $SrTiO_3$.

Table 4.2: Ratios obtained from XPS fits for *in situ* and *ex situ* samples, for both TiO_2- and SrO-termination, respectively.

	in situ		*ex situ*	
termination	TiO_2	SrO	TiO_2	SrO
C/Sr ratio (C 1s)	2.1 %	8.6 %	40 %	40 %
Carbonate contribution (C 1s)	-	-	3.0 %	6.5 %
Contamination concentration (O 1s)	24 %	21 %	28 %	30 %
Carbonate contribution (O 1s)	-	-	7.5 %	9.5 %
Sr related surface component (Sr 3d)	18 %	18 %	18 %	21 %

The strong increase of the C/Sr ratio for both terminations is typical for XPS measurements after ambient exposure due to adventitious carbon.[165, 166, 171, 172] The more pronounced carbonate component of the C 1s and O 1s spectra for the SrO-termination points towards the formation of $SrCO_3$, naturally occurring when SrO reacts with CO_2 of the atmosphere.[173] This is also substantiated by the increase of surface component obtained from the Sr 3d spectrum after ambient exposure exclusively for the SrO-termination, as the component could be $SrCO_3$ related. It thus seems that the SrO-termination is instable under ambient conditions due to the formation of $SrCO_3$, eliminating the oxygen vacancy formation inhibiting effect.

Application to $LaAlO_3/SrTiO_3$ heterostructures

As a method to tailor the oxygen vacancy incorporation in $SrTiO_3$ by control of the surface termination under UHV conditions was developed, it was subsequently transferred to the thin film system used within this chapter to elucidate the effects of oxygen vacancies, namely $LaAlO_3/SrTiO_3$.

As described in chapter 2.2 the interface of between $LaAlO_3$ and $SrTiO_3$ is only conducting in the *n*-type configuration. However, the *n*-type conducting interface was shown to prevail for interfaces with up to 83% SrO-termination, which can be explained by the formation of the 2DEG in the TiO_2-terminated areas and percolation paths in between those areas.[76, 78] Further chapter 2.2 described that the shift towards bulk conductivity of $SrTiO_3$ can easily be identified as it is accompanied by a shift towards lower resistivity. [18, 22, 25, 35, 76, 79, 81–86]

As described in chapter 2.2 similar to the bulk conductivity of crystalline $LaAlO_3$/ $SrTiO_3$ grown at low pressures, the 2DEG conductivity of the interface between amorphous $LaAlO_3$ and $SrTiO_3$ single crystals relies on the incorporation of oxygen vacancies into the $SrTiO_3$ lattice. Amorphous $LaAlO_3/SrTiO_3$ therefore can be expected to be sensitive to the oxygen vacancy incorporation at the interface as well. Thus one can expect to see differences in the conductivity depending on the termination for both, crystalline $LaAlO_3/SrTiO_3$ grown in the bulk-conducting regime (i.e. grown at low pressures) and for amorphous $LaAlO_3/SrTiO_3$.

Figure 4.11 a) shows the sheet resistance of crystalline $LaAlO_3/SrTiO_3$ in dependence of temperature obtained for different $SrTiO_3$ terminations. The sheet resistance of $LaAlO_3/SrTiO_3$ with 0% SrO-termination is about $100\ \Omega$ at room temperature and about $10^{-2}\ \Omega$ below 10 K. This corresponds to a dominant metallic bulk conduction of $SrTiO_3$, as expected for these growth conditions.[35] An increase of the SrO-termination to 50% results in an increase of the sheet resistance, to about $10^4\ \Omega$ at room temperature and about $10^3\ \Omega$ below 50 K. This is the typical temperature dependency of the sheet resistance for crystalline $LaAlO_3/SrTiO_3$ dominated by 2DEG conductivity.[18, 22, 25, 35, 76, 79, 81–86] Increasing the SrO-termination further to 100 % did, in agreement with observations reported in literature,[76, 78] result in insulating samples, whose sheet resistance is above the measurement limit ($10^8\ \Omega$).

Figure 4.11 b) shows the sheet resistance of amorphous $LaAlO_3/SrTiO_3$ in dependence of temperature and $SrTiO_3$termination. Amorphous $LaAlO_3/SrTiO_3$ with 0% SrO-terminated $SrTiO_3$ has a sheet resistance of about $10^4\ \Omega$ at room temperature and about $10^3\ \Omega$ below 50 K. This is in good agreement with the temperature dependent resistivity of the 2DEG formed by amorphous $LaAlO_3/SrTiO_3$, now solely relying on the incorporation of interface oxygen vacancies.[85, 87, 88] Increasing the SrO-termination of the $SrTiO_3$ substrate to 50% results in a slight increase of the sheet resistance by a factor of two. A further increase to 100% results, as for the

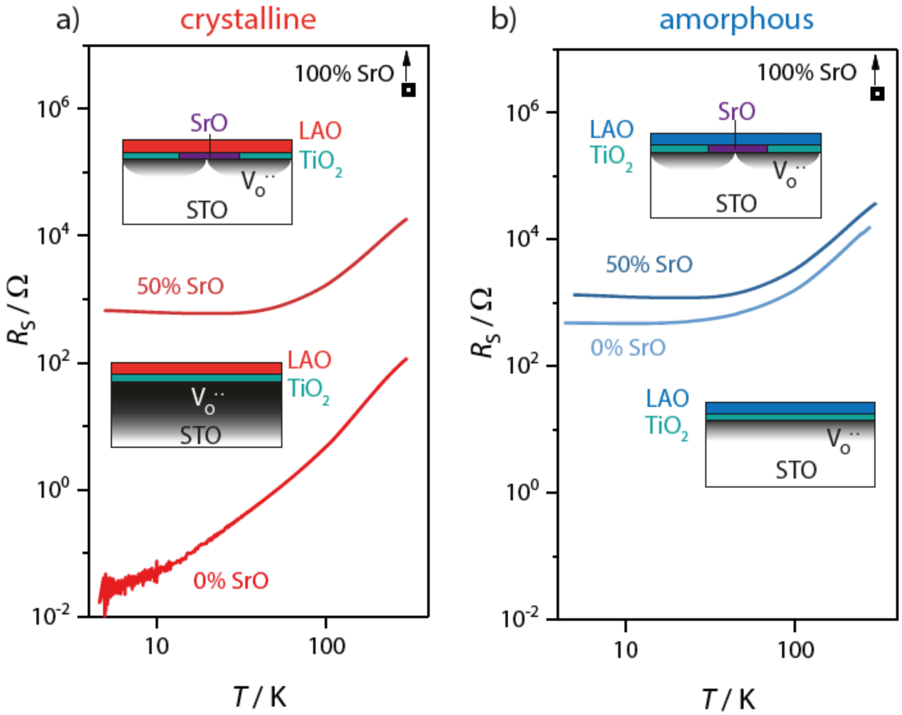

Figure 4.11: Sheet resistance in dependence of temperature of a) crystalline $LaAlO_3/SrTiO_3$ with different $SrTiO_3$ terminations and b) amorphous $LaAlO_3/SrTiO_3$ with different $SrTiO_3$ terminations. 100% SrO-termination results in insulating behavior for both heterostructures. 50% SrO-termination results in 2DEG conductivity for both, as does 0% SrO termination in the amorphous case. The 0% SrO-terminated crystalline $LaAlO_3/SrTiO_3$ shows metallic conductivity.

crystalline case, in an insulating sample. Hence, only a negligible amount of oxygen vacancies has formed at the SrO-terminated interface.

Figure 4.11 shows that the termination control of the $SrTiO_3$ substrate can be utilized to tailor the sheet resistance in $LaAlO_3/SrTiO_3$ heterostructures. As the sheet resistance of both, crystalline $LaAlO_3/SrTiO_3$ grown in reducing conditions and amorphous $LaAlO_3/SrTiO_3$, is defined by the oxygen vacancies[18, 22, 25, 35, 76, 79, 81–

88], their incorporation was successfully tailored. This also explains the shift from bulk dominated to interface dominated conductivity for crystalline LAO, when increasing the SrO-termination to 50% (Figure 4.11 a)). The oxygen vacancy incorporation is limited to the remaining TiO_2-terminated areas, as shown in the top sketch in Figure 4.11 a). The resulting confined conductivity is comparable to the conductivity of amorphous $LaAlO_3/SrTiO_3$ (Figure 4.11 b)), which is also dominated by oxygen vacancies confined to the interface, as shown in the according sketches. Thus, in the same way the increased resistivity for amorphous $LaAlO_3/SrTiO_3$ can be explained.

Discussion and conclusion: Influence of the termination layer

Considering all the results described above a more complete picture of the role of the termination of $SrTiO_3$ for its oxygen exchange kinetics is presented. Applying conditions known to be reducing for $SrTiO_3$ single crystals,[23, 79] it is only possible to efficiently incorporate oxygen vacancies into the TiO_2-terminated single crystal. The SrO-terminated sample remains insulating. It is concluded that the incorporation of oxygen vacancies is inhibited, as other kinetic and thermodynamic factors, e.g. the diffusion coefficient in the bulk, are not affected by termination.

The surface reaction of the oxygen vacancy incorporation is known to be a multi step process, which is influenced by several parameters.[56, 143] Considering that Alexandrov *et al.*[164] have shown by *ab initio* calculations that the formation energy of oxygen vacancies is lower for TiO_2-terminated $SrTiO_3$ as compared to SrO-terminated $SrTiO_3$, it is conceivable that the termination has an influence on one or more steps of the surface reaction. In particular a high formation energy of oxygen vacancies in SrO-terminated $SrTiO_3$ could fully depress the oxygen vacancy incorporation at SrO-terminated surfaces. The schematic of this is shown in figure 4.12.

Another possible mechanism behind the inhibited oxygen vacancy incorporation is SrO acting as a diffusion barrier for oxygen.[174] However an increased diffusion barrier was only shown for SrO in a rock salt structure. For SrO in the perovskite structure of $SrTiO_3$, the effect was not observed.[175] Thus the explanation of a

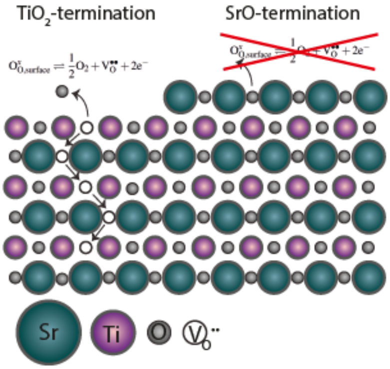

Figure 4.12: Schematic of the oxygen vacancy incorporation at the $SrTiO_3$ surface for different terminations. Due to the higher formation energy of oxygen vacancies for a SrO-termination, the oxygen vacancy incorporation is suppressed.

SrO diffusion barrier is ruled out, leaving the increased formation energy as decisive parameter.

The observed behavior, however, changed drastically after SrO-terminated $SrTiO_3$ was exposed to ambient conditions. Similar vacuum annealing of *ex situ* samples now resulted in high carrier densities independent of termination, indicating that the blocking effect of the SrO termination layer was eliminated by air exposure. This was accompanied by the formation of morphological features, indicating a clustering of SrO related particles.[175] Utilizing XPS measurements these particles were identified as $SrCO_3$.

If a SrO-termination inhibits the formation of oxygen vacancies, the formation of $SrCO_3$ can explain the elimination of the effect under ambient conditions. The formation of islands after ambient exposure results in pores in the oxygen blocking SrO-termination layer, revealing the TiO_2-terminated $SrTiO_3$, which then allows pathways for the incorporation of oxygen vacancies. Moreover, the resulting $SrCO_3$ clusters do not necessarily have a high formation energy for oxygen vacancies.

To profit from the new method to tailor the oxygen vacancy incorporation properties it was applied to the model application of the 2DEG at the $LaAlO_3$/$SrTiO_3$ heterointerface. Crystalline $LaAlO_3/SrTiO_3$ dominated by bulk conductivity and amorphous $LaAlO_3/SrTiO_3$ both rely on oxygen vacancy incorporation. In case of crystalline $LaAlO_3/SrTiO_3$ fabricated under reducing conditions a transition from bulk conducting $SrTiO_3$(0 %) to interface conductivity (50 %) and finally to insulating (100 %) is observed with an increasing amount of SrO-termination. For amorphous $LaAlO_3/SrTiO_3$ a transition to insulating behavior is observed as well, when increasing the SrO-termination to 100%. This confirms the inhibition of the incorporation of oxygen vacancies observed for $SrTiO_3$ single crystals.

Considering crystalline $LaAlO_3/SrTiO_3$ this is especially interesting, as it was found that the conductivity in the initial report of 2DEG conductivity by Ohtomo *et al.*[25] was in fact dominated by bulk conductivity, hence by oxygen vacancies.[18, 83] Nevertheless, conductivity was only observed for TiO_2-terminated $SrTiO_3$.[25] This effect could not be explained within the polar catastrophe scenario. With our findings it is possible to explain this phenomenon *via* the inhibition of the oxygen vacancy incorporation for the SrO-terminated sample.

Within this section a novel way to tailor the oxygen vacancy incorporation in $SrTiO_3$ by controlling its termination was provided. It was demonstrated that a SrO-termination of $SrTiO_3$ completely inhibits the incorporation of oxygen vacancies for otherwise reducing conditions. By systematically controlling the termination of $SrTiO_3$ it is thus possible to tailor the areas of oxygen vacancy incorporation. Due to the widespread use of $SrTiO_3$ as a substrate this result is highly interesting. A specific application for which this new method was employed are $LaAlO_3/SrTiO_3$ 2DEG heterostructures. By doing so, it is not only possible to directly influence the conductivity of these heterostructures, but also their understanding was improved. Further applications include, but are not limited to: i) oxides that require low oxygen pressure growth due to thermodynamic reasons (e.g. $LaVO_3$[176–178], $EuTiO_3$[179]), for which film properties would otherwise be masked by oxygen vacancies induced in $SrTiO_3$; ii) metals, which induce the incorporation of oxygen vacancies at the interface.[180]

4.1.4 Summary: Anion stoichiometry

In this section light was shed on different aspects influencing the anion stoichiometry in $SrTiO_3$. For mere thermal annealing an influence of residual gases was found and more vital an influence of measurement devices based on ionization. Residual gases can decrease the oxygen partial pressure by releasing e.g. hydrogen or carbonmonoxide. Ionic measurement devices change the carbonmonoxide carbondioxide equilibrium to a carbonmonoxide richer atmosphere. This in turn decreases the oxygen partial pressure resulting in a reducing atmosphere.

For PLD growth at adequately low pressures an influence of the UV radiation of the plasma plume was presented. This was enabled by the design of a new holder. It was found that the UV radiation of the PLD plasma plume significantly accelerates the oxygen vacancy formation for low pressure growth.

Last a way to modify the formation of oxygen vacancies was presented. It was found that the formation of oxygen vacancies in $SrTiO_3$ is termination dependent. Namely the formation is only observed for a TiO_2-termination. It is thus possible to tailor the conductivity in $SrTiO_3$, resulting from the induced oxygen vacancies, by manipulating its termination. Utilizing this knowledge $SrTiO_3$ and $LaAlO_3/SrTiO_3$ with a tailored oxygen vacancy formation were presented.

4.2 Cation stoichiometry

In order to vary the cation stoichiometry while ablating from a stoichiometric single crystal target, dependencies of the cation stoichiometry on different parameters during different stages of the PLD growth can be utilized. For the growth parameters of $SrTiO_3$ used in this work (compare chapter 3.2.1) a convenient way to influence the cation non-stoichiometry is a change of laser fluence.[17, 104–106]

As described in chapter 3.2.1 the laser fluence during PLD can easily be adjusted by an attenuator. To determine the detailed influence of the laser fluence on the cation stoichiometry, $SrTiO_3$ thin films were grown on $SrTiO_3$ and 0.5 wt% Nb:$SrTiO_3$ substrates. Thin films grown on $SrTiO_3$ substrates had a thickness of 100 nm to enable XRD analysis, thin films grown on 0.5 wt% Nb:$SrTiO_3$ substrates had a thickness of 20 nm, as those used for the MIM structures in the later chapters. Thin films grown on 0.5 wt% Nb:$SrTiO_3$ substrates were analyzed using XPS and AFM.

Figure 4.13 shows the RHEED data of $SrTiO_3$ thin films deposited with comparably low fluence ($F_L = 0.63$ J/cm^2 – 0.95 J/cm^2). The left column shows the intensity of the (01) spot (green), the (0$\bar{1}$) spot (blue) and the (00) spot (red) during the first ≈ 650 s of growth. The right column shows the relative intensity of these spots to each other after growth. Equally figure 4.14 shows the RHEED data of $SrTiO_3$ thin films deposited with higher fluence ($F_L = 1.04$ J/cm^2 – 1.58 J/cm^2).

As described in chapter 3.2.1 the intensity of the RHEED signal over time cannot only be used to determine the growth rate, but also gives information about the growth mode. For all fluence, except the lowest (figure 4.13 a)) and the highest (figure 4.14 e)), thickness oscillations are observable throughout the first ≈ 650 s of deposition, pointing towards a 2D layer by layer dominated growth. For the lowest fluence the primary (00) spot decreases markedly in intensity after about 300 seconds, while there is a slight increase of the (01) and (0$\bar{1}$) spots (figure 4.13 a)). The decrease of the primary spot can be associated with a roughening of the surface and is thus a hint for a change of the growth to the 3D island type.[181] The reason behind the simultaneous increase of the secondary spots is discussed in the next paragraph. For the highest fluence in figure 4.14 e) oscillations are observable for about 100 seconds.

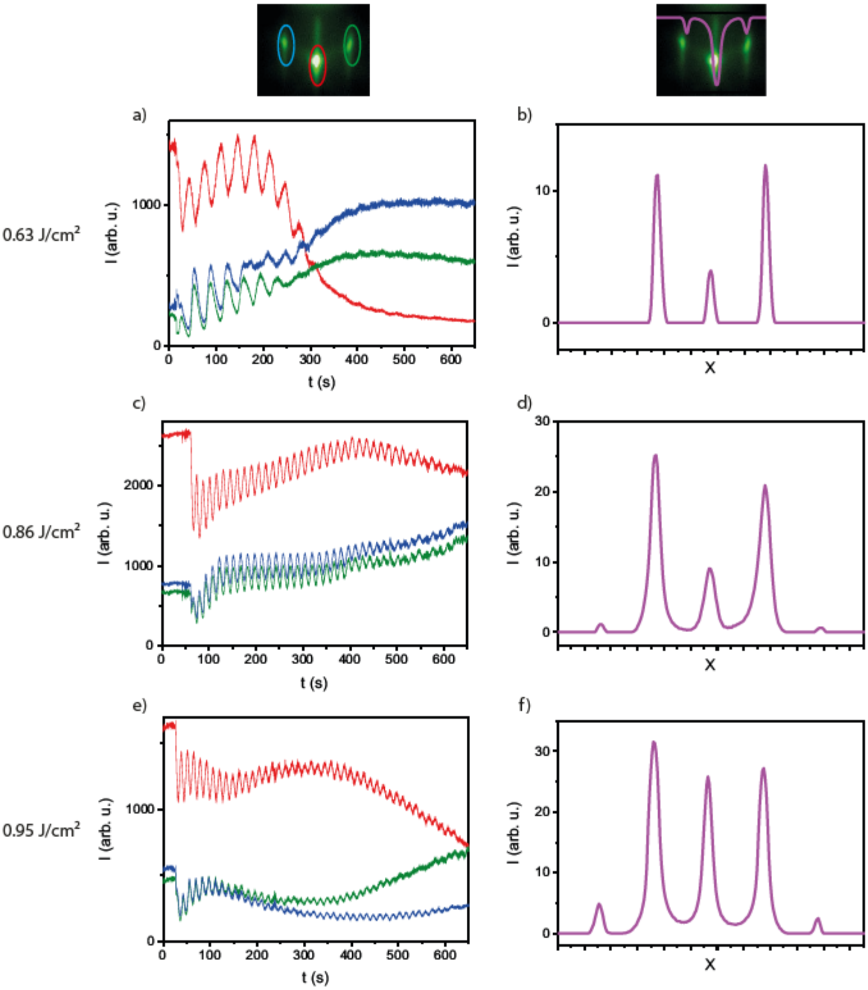

Figure 4.13: The left column shows the RHEED intensity over time and the right column the relative intensity of the (01) spot (blue), the $(0\bar{1})$ spot (green) and the (00) spot (red) for a laser fluence of 0.63 J/cm^2, 0.86 J/cm^{2}and 0.95 J/cm^2. The right column shows the line profile describing the intensity relation of the spots after deposition.

However, the signal intensity does not decrease after the oscillations vanish, but is constant. This indicates step flow growth.[101]

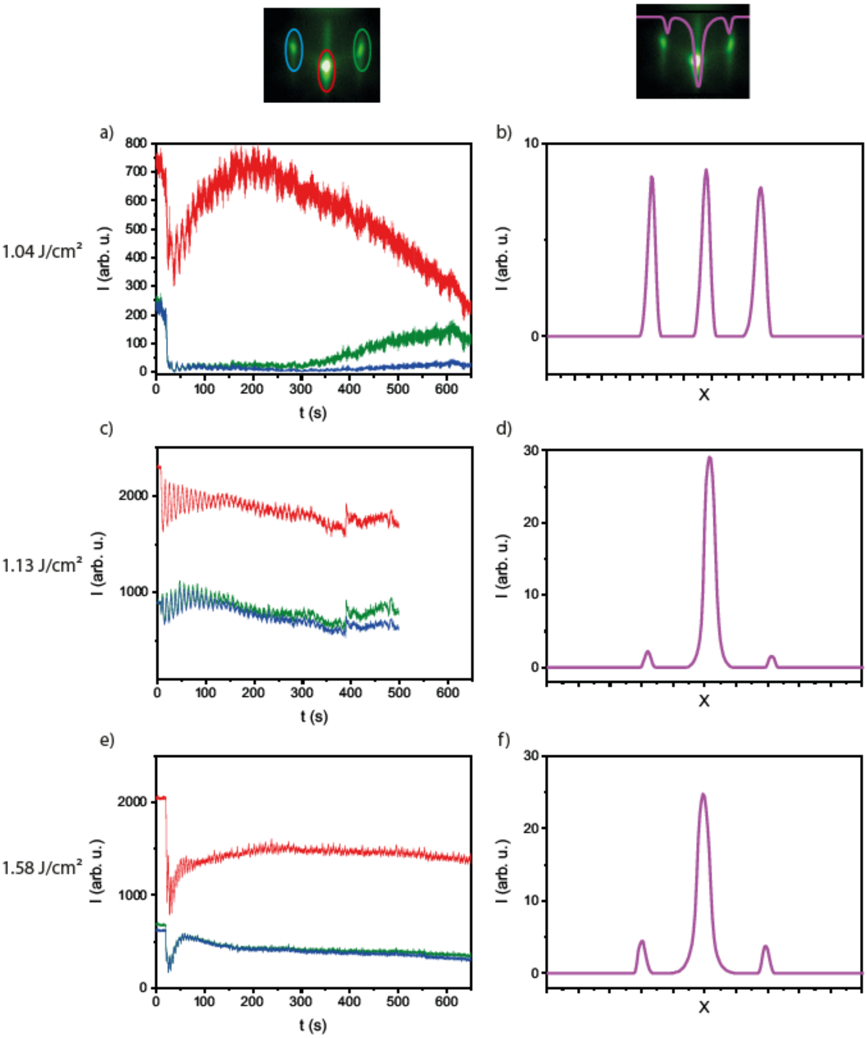

Figure 4.14: The left column shows the RHEED intensity over time and the right column the relative intensity of the (01) spot (blue), the $(0\bar{1})$ spot (green) and the (00) spot (red) for a laser fluence of 1.04 J/cm^2, 1.13 J/cm^{2}and 1.58 J/cm^2.The right column shows the line profile describing the intensity relation of the spots after deposition.

The RHEED signal can further give us information about the termination of $SrTiO_3$. As described in chapter 2.1.1 $SrTiO_3$ can either be TiO_2-, SrO- or mixed terminated.

Unterminated substrates (compare chapter 3.1) usually have a mixed termination consisting of 5 to 25 % SrO and 95 to 75 % TiO_2, respectively.[51] The top right of figures 4.13 and 4.14 represent the intensity ratio of the secondary spots and the primary spot for a typical unterminated substrate. Due to the higher atom form factor of Sr in comparison to Ti the intensity of the secondary spots (blue and green) increases proportionally to the share of SrO termination, while the intensity of the primary spot increases proportionally to the share of TiO_2-termination.[61, 182, 183] The right column of figures 4.13 and 4.14 can thus be used to qualitatively determine the termination of the grown films in dependence of the fluence as it compares the intensity of these spots. At the low fluence 0.63 J/cm^2(figure 4.13 d)) and 0.86 J/cm^2(figure 4.13 f) the secondary spots are dominant after deposition, thus a primarily SrO-terminated surface can be expected. With an increasing fluence the primary spot becomes more and more dominant after deposition, meaning that the share of TiO_2-terminated surface areas increases. For the highest fluence of 1.13 J/cm^2(figure 4.14 d)) and 1.58 J/cm^2(figure 4.14 f)) the secondary sports are barely visible after deposition in comparison to the primary spot, thus a TiO_2-termination can be expected.

To gain more information about the surface of the 20 nm $SrTiO_3$ on 0.5 wt% Nb:$SrTiO_3$ thin films, AFM scans were conducted and the mean square roughness (R_{ms}) was determined. Figure 4.15 shows the resulting topographies with the corresponding fluence and R_{ms} values.

Independent of the laser fluence the typical step structure of $SrTiO_3$ substrates remains observable (compare chapter 3.1). Nevertheless, distinct differences are observable. For the lowest fluence (figure 4.15 a)) the formation of islands is observed and the R_{ms} is consequently the highest. For a fluence between 0.86 J/cm^{2}and 1.04 J/cm^{2}the topography shows no distinct features (figure 4.15 b)-d)). The R_{ms} of all three thin films is reasonably low ($\leq$ 2 nm), however it is the lowest for F_L = 0.95 J/cm^2(1.1 nm). An increase of the fluence to 1.13 J/cm^{2}gives rise to the formation of distinct features on top of the step terraces (figure 4.15 e)), while maintaining a relatively low R_{ms} =2.1 nm. Increasing the laser fluence even further results in extended features on the surface, while the step terraces are barely observable. This also goes together with a markedly increase of the R_{ms} to 4.7 nm.

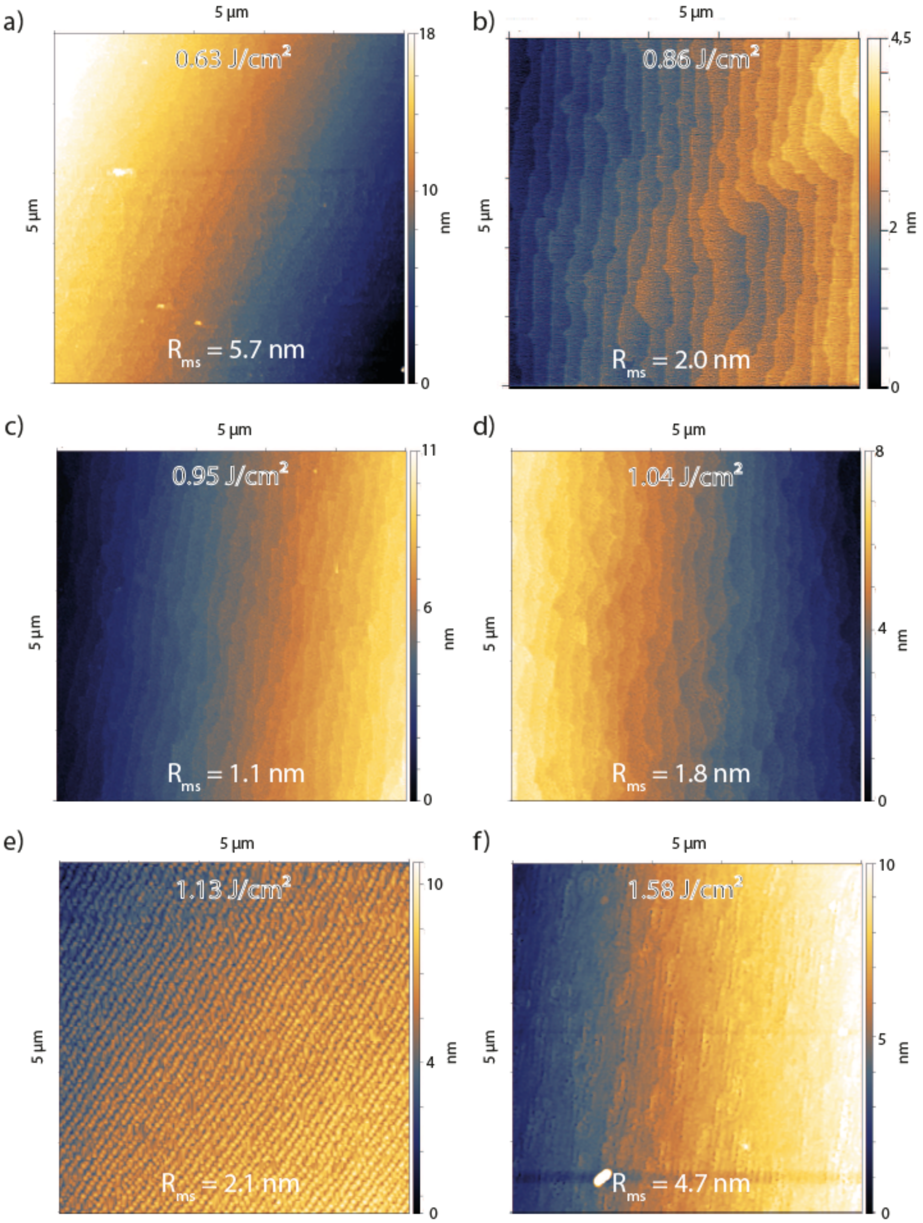

Figure 4.15: Topography of 20 nm $SrTiO_3$ thin films for a different laser fluence with the determined mean square roughness (R_{ms}).

While RHEED and AFM give hints on the stoichiometry of the thin films and RHEED even allows a qualitative analysis of the termination, XPS allows the quantification of both: termination and stoichiometry. This is achieved by an angular dependent measurement of the Ti^{2p} and Sr^{3d} peak. The peak ratio of both corresponds to Sr/(Sr+Ti). For high angles θ this corresponds to the bulk stoichiometry. As XPS gets more surface sensitive with decreasing angle, the ratio at low angles can be used to determine the termination.[184]

Figure 4.16a) shows the bulk Sr/(Sr+Ti) acquired by *in situ* XPS in dependency of the fluence (black) compared to the growth speed (red). The dashed blue line indicates the reference cation stoichiometry. As is to be expected the growth speed is higher for higher fluence. The films deposited with a fluence between 0.86 J/cm^{2}and 1.13 J/cm^{2}are nearly stoichiometric. The film grown with the lowest fluence is Sr-rich, the one with the highest fluence Ti-rich. Figure 4.16b) shows the angular dependent Sr/(Sr+Ti). The progression of this ratio shows an upwards trend for $F_L \leq 1.04$ J/cm^{2}and a downwards trend for $F_L = 1.13$ J/cm^{2}and $F_L = 1.58$ J/cm^2. Thus films grown with $F_L \leq 1.04$ J/cm^{2}predominately show a predominately SrO-terminated surface, while films grown with $F_L = 1.13$ J/cm^{2}and $F_L = 1.58$ J/cm^{2}are predominately $\mathrm{TiO_2}$-terminated.[184]

Although XPS performed at high angles gives bulk sensitive information to some extent, it is still a comparably surface sensitive method. Therefore, XRD measurements were performed. As described in chapter 3.2.2 the 2θ scan (figure 4.16 c)) gives information on the lattice expansion and the rocking curve (figure 4.16 d)) on the crystal quality. As shown in figure 4.16 c), a significant deviation of the c-lattice is only observable for the Ti-rich sample (light blue). Considering that the FWHM of all rocking curves is below 0.03° the bulk of all films is of reasonably good crystal quality.

Discussion and conclusion: Cation stoichiometry

Considering the entirety of results in this chapter a complete picture of the interplay between cation stoichiometry and laser fluence can be presented. For a low laser fluence (0.63 J/cm^2) (figure 4.17 a)) RHEED showed shares of 3D growth

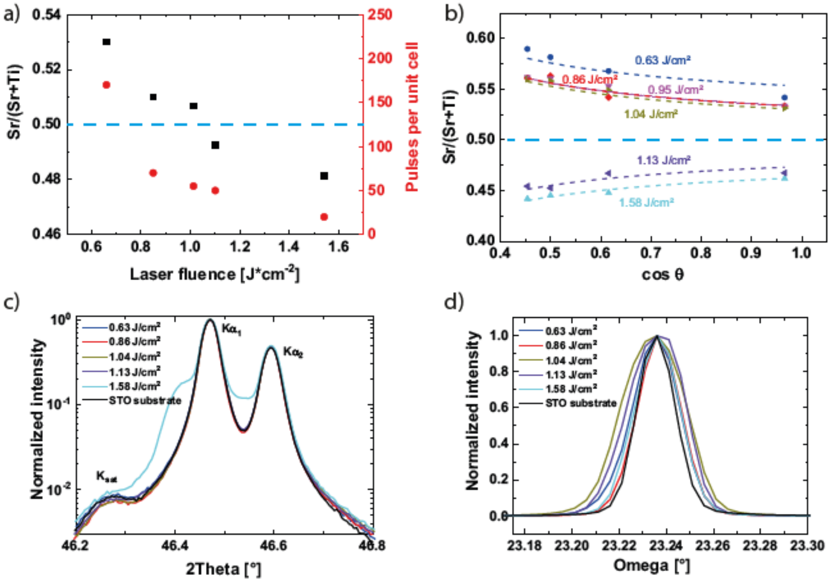

Figure 4.16: a) Sr/(Sr+Ti) ratio obtained from the Ti^{2p} and Sr^{3d} peak by XPS in dependency of the laser fluence (black) and in comparison to the growth rate (red) b) angular dependent Sr/(Sr+Ti) ratio c) XRD 2θ scan for different fluence and d) rocking curves.

and a predominately SrO-terminated surface. The topography confirmed the formation of islands during growth, which can be associated with SrO islands in the rock salt structure.[105, 175, 185] Utilizing angular dependent XPS the SrO termination of the thin film surface was confirmed. As the XRD data neither suggests a c-lattice expansion nor a decrease of crystal quality, but the formation of SrO islands was observed, it seems under these conditions the additional SrO is floating to the surface.[61] A second mechanism previously found for the accommodation of Sr-excess is the formation of Ruddlesden-Popper type anti phase boundaries.[20] In this case the excess of Sr is compensated by stacking fault in form of SrO double layers.

For intermediate fluence (figure 4.17 b)) the RHEED data suggested layer by layer growth and the topography showed that the step structure of the substrate was conserved. The XPS data confirmed that these films are nearly stoichiometric and their XRD data suggests the same. Interestingly all of these films still showed a termination dominated by SrO in opposite to the predominately TiO_2-terminated substrates.

For high fluence (figure 4.17 c)) the growth rate increases drastically and in case of 1.58 J/cm^{2}suggests step flow growth. The increased growth rate results in a second layer nucleation and resulting multilayer growth of the film.[185] This explains the change of the surface morphology and the increase in roughness for higher fluence. As expected the predominant TiO_2termination is restored for the high laser fluence resulting in Ti-rich films. The 2θ scan of the film grown with the highest fluence suggests a lattice expansion. The c-lattice expansion is a result of the formation of Sr-vacancies, which expand the lattice.[10, 62] In contrast to Sr-excess which is accommodated by SrO formation, the Ti-excess is accommodated by the formation of Sr vacancies. The reason behind this is that the formation energy of Sr vacancies is lower than the formation energy of Ti vacancies. Furthermore, the formation energy of SrO, either within or on top of $SrTiO_3$, is low.[60]

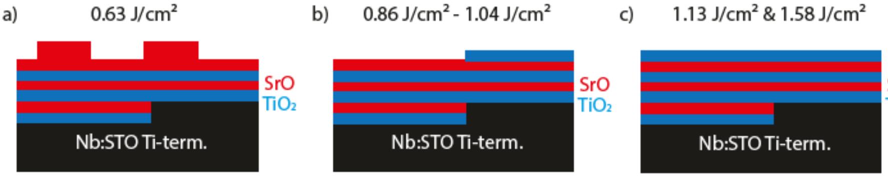

Figure 4.17: Schematics of the films resulting from different fluence regimes a) a low fluence results Sr-rich thin films with SrO islands b) intermediate fluence result in mixed terminated films c) high fluence result in Ti-rich films with a TiO_2termination

In chapter 3.2 influences on the cation non-stoichiometry during PLD were discussed in detail. In a simple manner these influences can be divided into three categories (Figure 4.1 a)):

1) Preferential sticking and re-sputtering on the substrate
   The high growth pressure ($\geq 10^{-1}$ mbar) applied for $SrTiO_3$ in this chapter means re-sputtering effects can be excluded. Further an influence of preferential sticking can be excluded, as neither SrO nor TiO_2 are volatile.[17, 186]

2) Incongruent ablation of the target
   As suggested in chapter 3.2 a probable reason for the cation non-stoichiometry

in $SrTiO_3$ is the difference in the effective evaporation enthalpies of the involved components. Here it was presented that with an increasing laser fluence the Ti ratio increases. This is in good agreement with the evaporation enthalpies,as they suggest that low fluence results in a preferential evaporation of SrO, while high fluence results in a preferential evaporation of TiO_2.[186]

3) Plume interactions

   In chapter 3.2 it was described that the different evaporation enthalpies fail to describe a non-linearity of the stoichiometry dependence on the fluence. Figure 4.16 a) suggests such a non-linearity, which can only be explained by the preferential scattering of the Ti species.

In conclusion, in this chapter the influence of the fluence on the cation stoichiometry was clarified. The cation stoichiometry can be steered precisely by fluence variation, as can the termination of the film. Low fluence result in Sr-rich thin films, intermediate fluence in stoichiometric thin films and high fluence in Ti-rich thin films. The non-stoichiometry is accommodated by different mechanisms. Sr-rich thin films form SrO islands and can also show extended defects in form of Ruddlesden-Popper type anti phase boundaries within the film[20]. Ti-rich growth is, in the here considered regimes, accommodated by the formation of Sr-vacancies. The reason behind the fluence dependent cation stoichiometry is an interplay of different effective evaporation enthalpies for SrO and TiO_2 and a stronger interaction with the process gas within the chamber for Ti than Sr at low energies.

5 Engineering $SrTiO_3$ for resistive switching

After considering possibilities for engineering defects in the previous chapter, this chapter will discuss possible applications for defect engineering in $SrTiO_3$ thin films for resistive switching. In the previous chapter the impact of Sr-rich growth on the defect structure was discussed. It was found that Sr-rich $SrTiO_3$ growth can on the one hand be accommodated by the formation of Ruddlesden-Popper type anti phase boundaries and on the other hand by the formation of SrO islands on top of the film.

Previous works in this group already considered the influence of stoichiometry deviations on the resistive switching properties of $SrTiO_3$. It was shown that the low resistive state (LRS) of Sr-rich $SrTiO_3$ is more stable over time in comparison to Ti-rich and stoichiometric $SrTiO_3$. Further it was shown that Sr-rich devices also exhibit an improved ON/OFF ratio, as they have a lower LRS and a higher high resistive state (HRS) than stoichiometric and Ti-rich devices.[48] Sr-rich devices thus show an overall superior performance.

A major focus of this group has thus been to understand the superior performance of Sr-rich $SrTiO_3$. As described in chapter 2.3 resistive switching of $SrTiO_3$ is based on the formation of an oxygen vacancy rich filament during the first sweep. It was recently shown by this group that the oxygen vacancies are introduced at the Pt/$SrTiO_3$ interface.[98, 100] It has been shown that the oxygen vacancy concentration at this interface increases by a factor of 2-3 for the LRS in comparison to the HRS. Therefore the reoxidization of the $SrTiO_3$ at the Pt interface results in an LRS failure.[187, 188]

Under consideration of this knowledge two possible explanations for the improved performance of Sr-rich devices have been presented by this group. The first is a stabilization of the oxygen vacancies of the filament at extended defects such as anti phase boundaries.[48] In the previous chapter it was shown that Ruddlesden-Popper type anti phase boundaries can accommodate the Sr surplus of Sr-rich growth. Another mechanism of Sr excess accommodation is the formation of SrO islands, which were found to be an oxygen diffusion blocking layer and thus were presented as the second explanation for a filament stabilization.[174] While both possibilities can explain the enhanced stability of the LRS, either by a stabilization of the oxygen vacancies,[48] or by a blockage of the reoxidization,[174] neither can explain the enhanced ON/OFF ratio. Further both explanations lack the possibility to ultimately separate the influence of extended defects from the influence of SrO islands.

This chapter thus aims to enable a differentiation between the influence of the different types of Sr-excess accommodation on the resistive switching properties of $SrTiO_3$. This will be achieved by engineering both accommodation types separately in stoichiometric films. It is conceivable that it is possible to engineer Ruddlesden-Popper type anti phase boundaries by a controlled deposition of SrO double layers. To start with a defined SrO coverage it is important to start with a defined surface termination.

As former studies mainly worked with unterminated 0.5 wt% Nb:$SrTiO_3$ substrates for resistive switching[189, 190] the first step will be to investigate, whether the termination of the substrate has an influence on the switching performance of the $SrTiO_3$ devices. After clarifying the influence of the substrate termination, the impact of purposefully induced Ruddlesden-Popper type anti phase boundaries will be considered. Last the influence of SrO islands on top of stoichiometric $SrTiO_3$ will be investigated.

Parts of this chapter were published in reference [175].

5.1 Role of the substrate termination and thin film stoichiometry

The goal of this section is to determine, whether the termination of the 0.5 wt% Nb:$SrTiO_3$ substrate plays a role for the switching behavior of the $SrTiO_3$ thin film. Sr-rich and stoichiometric films are investigated with regard to their *I(V)*-characteristics, their time stability and variability. Current compliances of 10 mA and 30 mA are applied for the SET, as previous work suggests that the difference between stoichiometric and Sr-rich films can be best observed at 10 mA and vanishes to some extend at 30 mA.[174] For the self limiting RESET no current compliance is required.

Figure 5.1 shows the *I(V)*-characteristics of the stoichiometric $SrTiO_3$ thin films for the forming step (red) and a representative SET (blue). The voltage was nominally 3 V for the SET and -4 V for the RESET (compare chapter 2.3). The top row shows the *I(V)*-characteristics with a current compliance of 10 mA for an unterminated (a)) and a TiO_2-terminated substrate (b)). The bottom row shows the *I(V)*-characteristics with a current compliance of 30 mA for an unterminated (c)) and a TiO_2-terminated substrate (d)), respectively.

The 30 mA current compliance is reached at a higher voltage than the 10 mA current compliance, for both terminations (dashed line). For all devices the increase of the current is shifted to a higher voltage for the first sweep (red) in comparison to subsequent SETs (blue). The samples thus show a small, but distinguishable, forming step. Both forming and SET are gradual. For the respective current compliance the *I(V)*-characteristics show no apparent influence of the substrate termination.

Figure 5.2 shows the *I(V)*-characteristics of the Sr-rich $SrTiO_3$ thin films for the first sweep (red) and a representative SET (blue). SET, RESET and current compliance were applied in the same way as for the stoichiometric samples.

In contrast to the stoichiometric samples the forming step does not necessarily change to higher voltages for higher current compliances. Further only the SET is as gradual as for the stoichiometric devices, for the first sweep the current increases faster

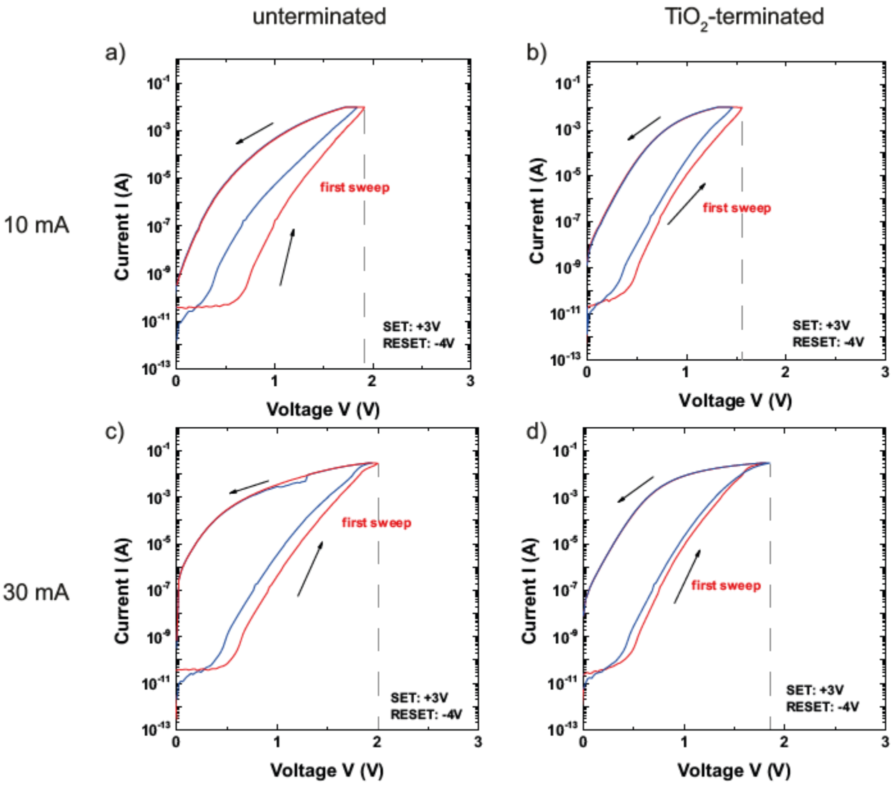

Figure 5.1: *I(V)*-characteristics of stoichiometric SrTiO$_3$thin films grown on unterminated (left) and TiO$_2$-terminated (right) 0.5 wt% Nb:SrTiO$_3$substrates. All samples were SET with 3 V and RESET with -4 V. The top row shows the first sweep (red) and SET (blue) for a current compliance of 10 mA, the bottom row for a current compliance of 30 mA, respectively.

than the voltage can be controlled by the source, resulting in an increasing current with a decreasing voltage in the current compliance. Additionally for the Sr-rich devices the shift of current increase between SET (blue) and first sweep (red) is even more pronounced. Both of these observation result in a more pronounced forming step for the Sr-rich devices than for the stoichiometric devices, which is in accordance with previous work.[48, 174, 175] Again the *I(V)*-characteristics show no apparent influence of the substrate termination for the respective current compli-

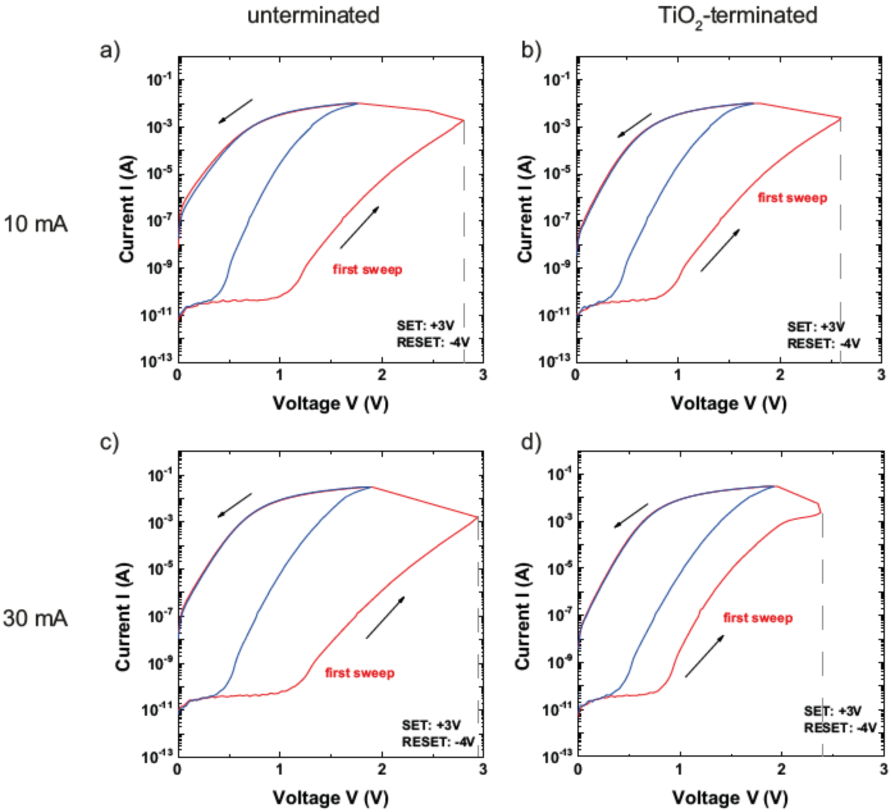

Figure 5.2: *I(V)*-characteristics of Sr-rich $SrTiO_3$thin films grown on unterminated (left) and TiO_2-terminated 0.5 wt% Nb:$SrTiO_3$(right) substrates. All samples were SET with 3 V and RESET with -4 V. The top row shows the first sweep (red) and SET (blue) for a current compliance of 10 mA, the bottom row for a current compliance of 30 mA, respectively.

ance.

Considering the *I(V)*-characteristics of MIMs based on mixed- and TiO_2-terminated 0.5 wt% Nb:$SrTiO_3$ at most a small difference is conceivable. For further investigation the time stability of the LRS and the ON/OFF ratio for both current compliances and all four MIM setups was measured.

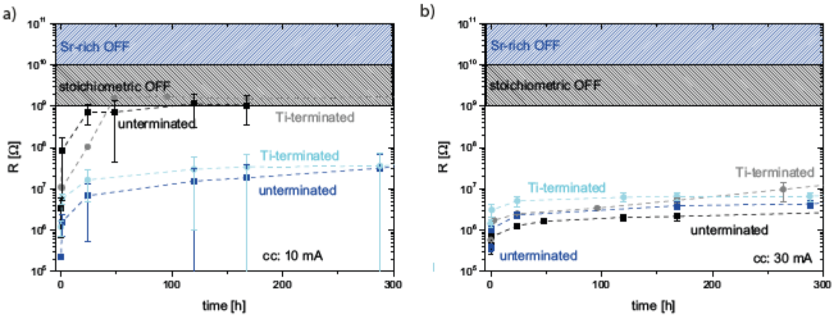

Figure 5.3: LRS retention over 300 h and ON/OFF ratios for a) a current compliance of 30 mA and b) a current compliance of 10 mA for stoichiometric samples (black and gray) and Sr-rich samples (blue and turquoise).

Figure 5.3 a) shows the ON/OFF ratio and time stability of the LRS for samples switched with 10 mA current compliance. The Sr-rich devices show a LRS around 10^6 Ω, the LRS of the stoichiometric devices is around one order of magnitude higher independent of substrate termination. The HRS of the Sr-rich samples is around one order of magnitude higher than for the stoichiometric devices for both kinds of substrates, TiO_2-terminated and unterminated. This results in an ON/OFF ratio of 10^4 for the Sr-rich samples and an ON/OFF ratio of 10^2 for the stoichiometric samples. The LRS of the Sr-rich devices increases by a factor of 2 within the first hour and saturates around 10^7 Ω in the course of 300 h. The stoichiometric devices, however, show an initial increase of the LRS of one order of magnitude and after between 25 and 50 hours their LRS becomes indistinguishable from the HRS. The LRS of all samples has a high device to device variability as the error bars indicate.

Figure 5.3 b) shows the ON/OFF ratio and LRS time stability for samples switched with 30 mA current compliance. As for switching with a 10 mA current compliance the HRS of all stoichiometric samples is 10^9 Ω and for all Sr-rich samples 10^{10} Ω. However the initial LRS is now around 10^6 Ω for all samples. The ON/OFF ratio is thus 10^3 for the stoichiometric samples and 10^4 for the Sr-rich samples. All samples show a steep increase in the LRS of a factor around 1.5 within the first hour. Afterwards the LRS is reasonably stable for at least 300 h. In comparison to the samples switched with 10 mA current compliance the device to device variability is lower, as indicated by the error bars.

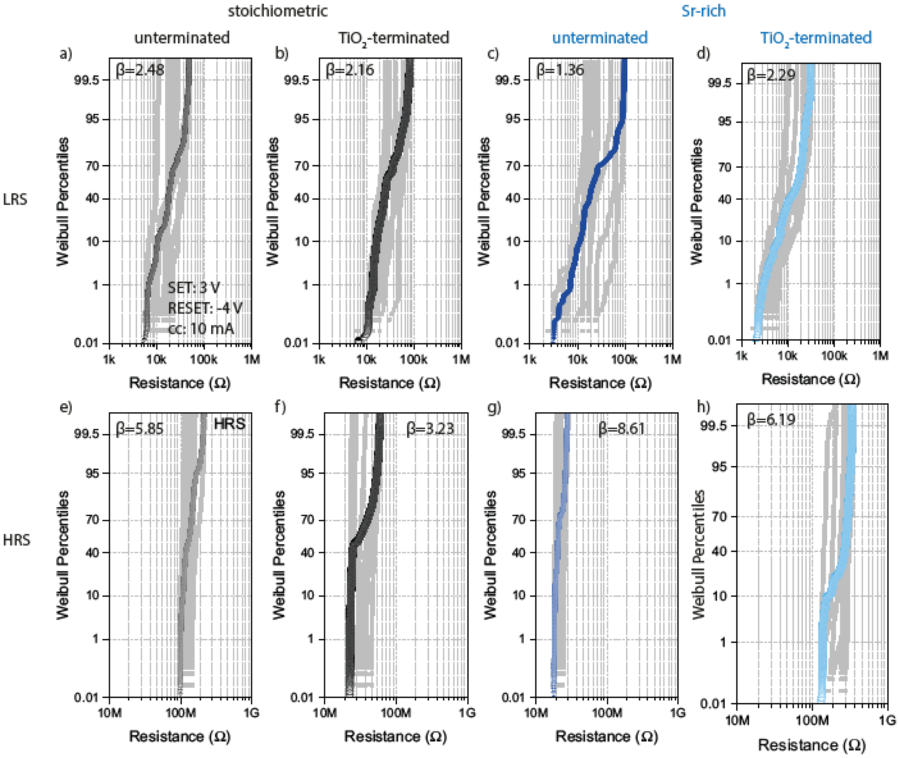

Figure 5.4: Comparison of the device to device and cycle to cycle variability for the LRS a) - d) and the HRS e) to h) of stoichiometric and (left) and Sr-rich (right) devices based on TiO_2-terminated and unterminated 0.5 wt% Nb:$SrTiO_3$.

One reason behind the high error in figure 5.3 is the used MIM. As described in chapters 3.3 and 3.4, the MIM layout used for *I(V)*-characterization and LRS time stability measurements requires contacting the top electrode directly with a W-whisker probe resulting in an inherent high variability induced by the contact resistance and its change over time. In the same chapters an alternative layout, avoiding direct contacting, was introduced. While this MIM inhibits the inherently high variability it does not allow switching for a 30 mA current compliance. Figure 5.4 shows the result of the variability measurements. Each gray graph represents the cycle to cycle variability of one device. It was acquired over 2000 cycles. The highlighted graph represents the device to device variability taking the cycle to cycle variability into account. It is acquired by averaging the respective gray graphs. A measure for the device to device variability is the Weibull slope β, which results from the highlighted graphs; the higher its value, the lower the variability.

The top row of figure 5.4 shows the variability of the LRS of stoichiometric and Sr-rich devices based on unterminated and TiO_2-terminated 0.5 wt% Nb:$SrTiO_3$ substrates. Comparing the influence of the termination for both stoichiometries no influence on cycle to cycle or device to device variability is observable. However, comparing both stoichiometries with each other, the Sr-rich devices (figure 5.4 c) and d)) show a higher cycle to cycle variability than the stoichiometric devices (figure 5.4 a) and b)). The bottom row of figure 5.4 shows the variability of the HRS. Independent of substrate termination and film stoichiometry, devices have a very low cycle to cycle and device to device variability in the HRS ($3.23 \leq \beta \leq 8.61$) . As described in chapter 2.3, given appropriate switching parameters, the HRS is similar to the virgin resistance.[92, 191]

Discussion and conclusion: Role of the substrate termination and thin film stoichiometry

In this chapter the influence of the 0.5 wt% Nb:$SrTiO_3$ termination on the switching properties of $SrTiO_3$ was investigated for stoichiometric and Sr-rich thin films. Considering all measured properties, *I(V)*-characteristics, time stability, ON/OFF ratio and variability, the termination of the substrate plays at most a minor role for the switching performance.

As described in the introduction to this chapter the stoichiometry, however, plays a central role for the switching performance.[48, 174] Within this chapter it was shown that independent of the substrate termination Sr-rich devices show an improved LRS stability compared to stoichiometric devices. The following chapter will answer the question, if the improved LRS stability is based on the stabilization of oxygen vacancies at Ruddlesden-Popper type anti phase boundaries[48] or on the blockage of the reoxidization by SrO islands[174].

Similar to the time stability of the LRS the improved ON/OFF ratio of Sr-rich devices in comparison to stoichiometric devices is independent of the substrate termination. In addition to these properties the cycle to cycle and device to device variability were investigated with respect to stoichiometry and termination. Again the termination proved to have no influence, whereas Sr-rich devices have higher variability than stoichiometric devices. A possible explanation for this can be deducted from the previous chapter. Equally to the improved LRS stability an influence of the Ruddlesden-Popper type anti phase boundaries or the SrO islands is conceivable. If in fact these defects have a considerable influence on the switching performance of $SrTiO_3$ their uneven distribution can explain the higher device to device variability. A possible explanation for the higher cycle to cycle variability is a change of either the Ruddlesden-Popper type anti phase boundaries or the SrO islands between cycles. However, both of these explanations require further investigations to be proven.

As the termination of the 0.5 wt% Nb:$SrTiO_3$ substrate does not markedly influence the properties of resistively switching $SrTiO_3$ and a TiO_2-termination offers the benefit of a defined substrate surface, all following $SrTiO_3$ MIM structures are based on TiO_2-terminated 0.5 wt% Nb:$SrTiO_3$.

5.2 SrO interface engineering

In this chapter it will be investigated, which influence both possibilities of Sr-excess accommodation, Ruddlesden-Popper type anti phase boundaries and SrO islands, have on the switching performance of $SrTiO_3$ devices. In order to separate both of their influences the respective accommodation mechanisms will be engineered for stoichiometric $SrTiO_3$ thin films.

5.2.1 Additional SrO at the bottom interface

The first step in investigating the influence of Ruddlesden-Popper type anti phase boundaries independently of other effects of off-stoichiometric growth is to find a method to purposefully induce them into a stoichiometric thin film. As described in chapters 2.1, Ruddlesden-Popper type anti phase boundaries are in principal stacking errors induced by a double layer of SrO. An obvious approach is thus to deposit additional SrO within the stack. However, if a double layer of SrO is deposited, there is only a Ruddlesden-Popper type anti phase boundary parallel to the growth direction. In order to achieve Ruddlesden-Popper type anti phase boundaries perpendicular to the growth direction an incomplete layer of SrO is needed. At the edges of the resulting one u.c. high SrO islands the anti-phase boundaries should be induced. The underlying principle is depicted in figure 5.5.

As the substrates have a TiO_2-termination, 1.5 u.c. of SrO were deposited using the parameters described in chapter 3.2. Subsequently, stoichiometric $SrTiO_3$ is grown using the parameters obtained in chapter 4.2. Figure 5.6 a) shows the topography resulting from such a thin film growth. The step edges are barely visible and numerous islands have formed. The surface is comparable to the surface of Sr-rich thin films, which show the outgrowth of SrO islands (compare chapter 4.2). It thus seems that the additional SrO did not remain at the bottom interface and induce anti-phase boundaries as intended, but rather ended up at the top interface. This effect can be explained by the findings of Nie *et. al.*[61], that for SrO double layers it is energetically preferable for the additional SrO to migrate to the surface of the film. This is schematically represented on the left side of figure 5.5.

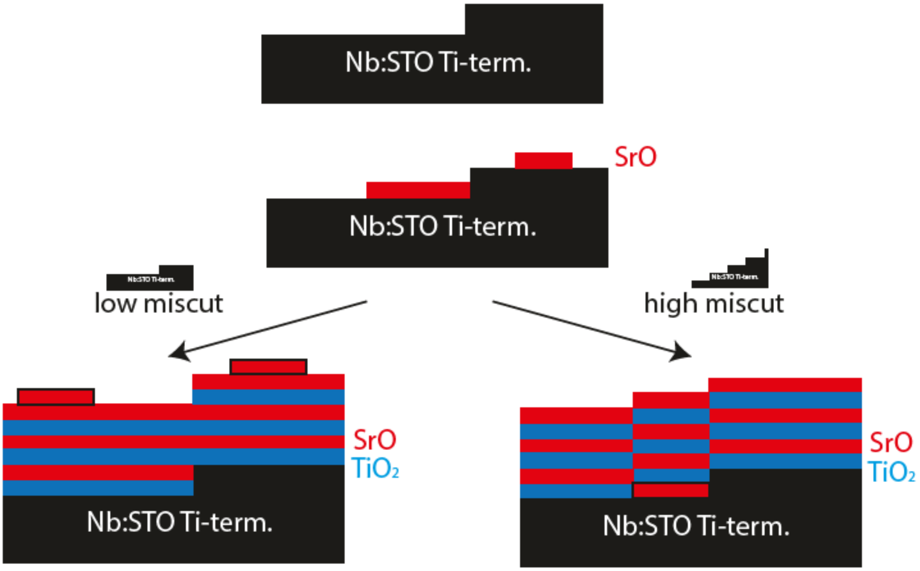

Figure 5.5: The two possibilities of stoichiometric $SrTiO_3$growth on top of a TiO_2-terminated 0.5 wt% Nb:$SrTiO_3$substrate with 1.5 u.c. of SrO. Either the SrO migrates to the top or it is stabilized at the bottom interface and induces anti phase boundaries.

The challenge is thus to prevent the additional SrO deposited at the bottom interface from migrating to the stop interface. Generally two strategies are conceivable for this. If the subsequent growth of $SrTiO_3$ is performed at a temperature low enough to suppress fast cation diffusion, a migration of the SrO layer to the surface is also suppressed. This strategy inherently results in additional problems. A suppression of the cation diffusion results in thin films with additional extended defects and thus a poor crystal quality.[66, 192] The second strategy is to stabilize the SrO at step edges. In comparison to a normal site on a step terrace, where a species is only bond on one side, a species at a step edge is bond on two sides. Thus species bond at step edges are energetically more stable.[193] To utilize this 0.5 wt% Nb:$SrTiO_3$(100) substrates with an intentionally high miscut were selected. The miscut is responsible for the density of step edges, the higher the miscut in one direction the higher the step edge density. Here a miscut of 4° in the (010) direction was chosen.

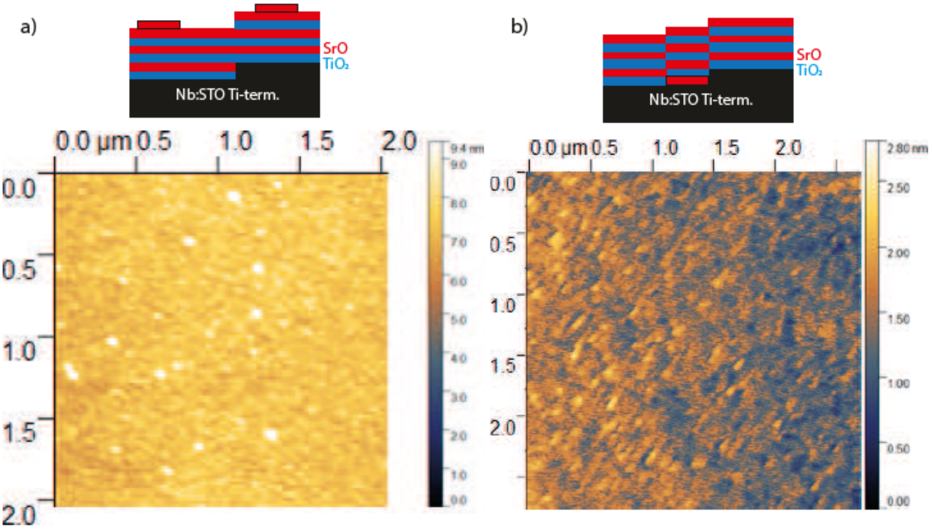

Figure 5.6: Topography of stoichiometric $SrTiO_3$deposited on 1.5 u.c. of SrO on top of a) standard TiO_2- terminated 0.5 wt% Nb:$SrTiO_3$and b) TiO_2- terminated 0.5 wt% Nb:$SrTiO_3$with intentional miscut.

Figure 5.6 b) shows the topography of a stoichiometric $SrTiO_3$ film grown on top of 1.5 u.c. of SrO, which were grown on the 4° miscut TiO_2-terminated 0.5 wt% Nb:$SrTiO_3$ substrate. Using the substrate with a miscut results in a thin film, which shows no SrO segregations. Further, the dense step edge structure remains observable. It is thus probable that the 1.5 u.c. of SrO are indeed located within the film. To verify this TEM analysis was performed.

Figure 5.7 a) shows the HAADF TEM survey of the stoichiometric $SrTiO_3$ thin film grown on 1.5 u.c. of SrO on top of 4° miscut TiO_2-terminated 0.5 wt% Nb:$SrTiO_3$ substrate and a zoom into the interface area between thin film and substrate. The survey reveals that the grown thin film exhibits a good crystal quality. The zoom into the interface area reveals a double layer of Sr (green) at the interface. This means, that the additional 1.5 u.c. SrO grown on the bottom interface, did indeed remain there and did form a Ruddlesden-Popper type anti phase boundary parallel to the growth direction.

The next step is to validate, whether the engineering of Ruddlesden-Popper type

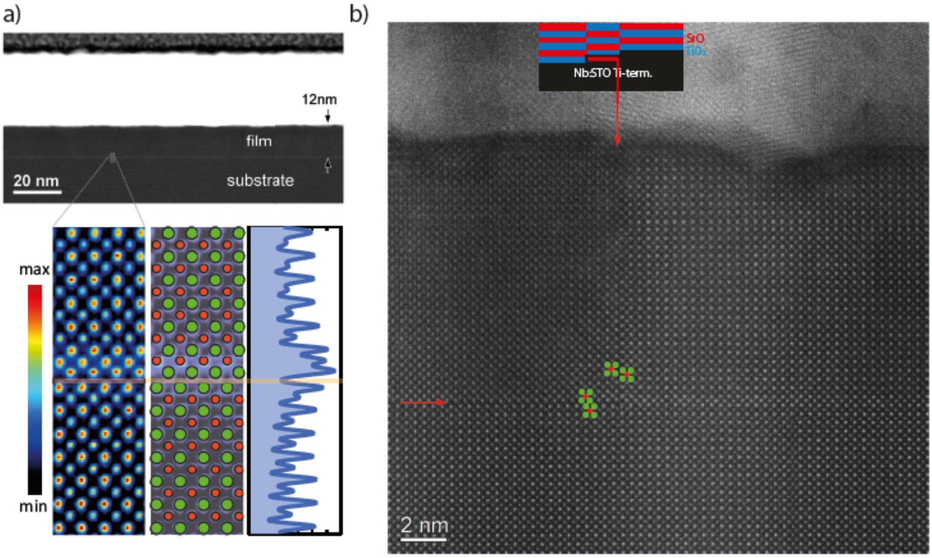

Figure 5.7: a) HAADF TEM survey of the stoichiometric $SrTiO_3$thin film grown on 1.5 u.c. of SrO on top of TiO_2- terminated 0.5 wt% Nb:$SrTiO_3$with intentional miscut and zoom on the substrate thin film interface. Green dots represent Sr, red ones Ti b) Close up of the induced anti phase boundary with unit cells marked for orientation. The TEM measurements were conducted by Hongchu Du.

anti phase boundaries perpendicular to the growth direction was equally successful. Figure 5.7 b) shows a HAADF TEM survey of a step edge and the interface between substrate and thin film. As planned a Ruddlesden-Popper type anti phase boundary starts at step edge of the substrate and continues throughout the film.

The TEM results of figure 5.7 and the AFM result of figure 5.6 show that vertical anti phase boundaries were successfully engineered within an otherwise stoichiometric thin film. The electrical characterization of this thin film should thus unravel the effect of the anti phase boundaries on resistive switching.

Figure 5.8 shows the first sweep (red) and SET (blue) *I(V)*-characteristics for a current compliance of a) 10 mA and b) 30 mA. Similar to the switching of stoichiometric devices shown in figure 5.1 the current compliance is reached at higher voltages for a higher current. Independent of the current compliance, the first sweep

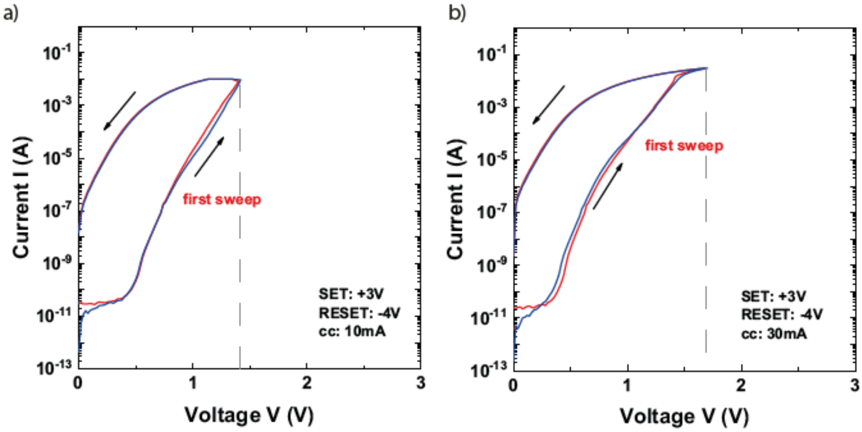

Figure 5.8: *I(V)*-characteristics of a sample with intentionally induced anti phase boundary witched with a) a current compliance of 30 mA and b) a current compliance of 10 mA.

is not distinguishable from the subsequent SET. The devices are thus forming free. Considering the *I(V)*-characteristics of Sr-rich devices in figure 5.2 it is conspicuous that the *I(V)*-characteristics of the *I(V)*-characteristics of devices with intentionally induced Ruddlesden-Popper type anti phase boundaries do not resemble them.

To ultimately verify the influence of Ruddlesden-Popper type anti phase boundaries, the time stability of the LRS and the ON/OFF ratio of the devices are compared to stoichiometric and Sr-rich devices for 10 and 30 mA current compliance (figure 5.9), respectively. As described in chapter 5.1 the OFF state of Sr-rich devices is one order of magnitude higher than the OFF state of stoichiometric devices. The OFF state of the anti phase boundary devices is identical to the OFF state of the stoichiometric devices.

Figure 5.9 a) shows the ON/OFF ratio and time stability of the LRS for 10 mA current compliance. In accordance with chapter 5.1 the Sr-rich devices have a lower ON resistance than the stoichiometric devices and considering the higher OFF resistance consequently also a higher ON/OFF ratio. In contrast to the stoichiometric devices they also have a stable retention of more than 300 h. The ON state of the stoichiometric devices becomes indistinguishable from their OFF state within 50 h. The ON state of the anti phase boundary devices is even higher than the one of the stoichiometric devices. They thus have the lowest ON/OFF ratio. Within one hour their ON state is no longer distinguishable from their OFF state. Hence they also have the shortest retention time.

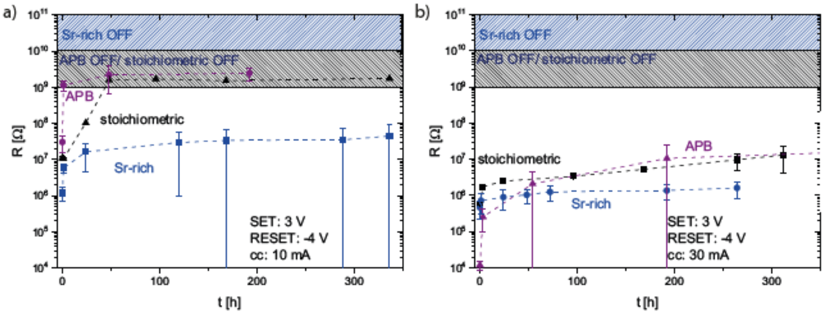

Figure 5.9: Retention and ON/OFF ratio of stoichiometric (black) Sr-rich (blue) and anti phase boundary (violet) devices for a current compliance of a) 10 mA and b) 30 mA. The OFF state of the Sr-rich devices is hatched in blue, the OFF state of the anti phase boundary devices and the stoichiometric devices in black

Figure 5.9 b) shows the ON/OFF ratio and time stability of the LRS for 30 mA current compliance. As for the current compliance of 10 mA the LRS time stability and ON/OFF ratio of stoichiometric and Sr-rich devices is in accordance with chapter 5.1. The Sr-rich devices have a higher ON/OFF ratio and a more stable retention. However, for 30 mA current compliance, also the LRS of the stoichiometric devices is reasonably time stable. Surprisingly using 30 mA current compliance, the LRS of the anti phase boundary devices is the lowest with approximately 10^4 Ω. Within the first hour a steep increase in resistance is observable, comparable to the 10 mA current compliance. Subsequently, the 30 mA current compliance LRS stabilizes on the same level as the LRS of the stoichiometric devices.

Discussion and conclusion: Bottom interface engineering

Considering the *I(V)*-characteristics, the ON/OFF ratio and the time stability of the LRS of anti phase boundary devices and comparing them to stoichiometric and Sr-rich devices it is unlikely that Ruddlesden-Popper type anti phase boundaries are responsible for the enhanced ON/OFF ratio or improved time stability of the LRS of Sr-rich devices. Their retention time is even shorter than the one of the stoichiometric devices and their ON/OFF ratio only improves at 30 mA current compliance. While Ruddlesden-Popper type anti phase boundaries can thus be excluded as the responsible mechanism for an enhanced performance of Sr-rich devices, devices with intentionally induced Ruddlesden-Popper type anti phase boundaries still show a highly interesting property. Their first *I(V)*-sweep is identical to all subsequent SETs, they are thus forming free. A property that is highly desirable for application,[194] but was so far not reported for resistively switching $SrTiO_3$.

As the devices with intentionally induced Ruddlesden-Popper type anti phase boundaries are forming free, an obvious explanation would be the presence of a preformed filament. Further, the only difference between these devices and stoichiometric devices are the Ruddlesden-Popper type anti phase boundaries. It is thus likely that the Ruddlesden-Popper type anti phase boundaries are connected to the preformed filaments. A possible explanation is an enrichment in naturally occurring oxygen vacancies[195, 196] at the Ruddlesden-Popper type anti phase boundaries. This is conceivable as it was reported for other extended defects in $SrTiO_3$, namely small angle grain boundaries[197, 198] and dislocations[7, 198, 199]. For these defects the formation energy of oxygen vacancies is lower in the defect's vicinity.[7, 197–199] If the formation of oxygen vacancies is lower at Ruddlesden-Popper type anti phase boundaries, it is conceivable that this naturally occurring oxygen vacancy rich region is the preformed filament, ultimately explaining the lack of a forming step.

Postulating preformed filaments, the short retention time of these devices can also be explained. Joule heating is an important factor for the formation of the oxygen vacancy rich filament in $SrTiO_3$, as it aids the oxygen vacancy formation and diffusion.[93, 95, 100] Generally Joule's first law describes: $P \propto I^2 R$. If Ohm's law applies as well the proportionality turns into a equation.[200] Considering the

I(V)-characteristics of $SrTiO_3$ devices Ohm's law does, however, not apply. A precise determination of the Joule heating present in these devices is thus difficult. Nevertheless qualitatively one can expect higher Joule heating, when the current compliance is reached at a higher voltage and when the current increase takes place at higher voltages. For devices with a forming step considerable Joule heating is induced during forming. The Joule heating increases vacancy formation and diffusion, resulting in filaments with a diameter of 100-500 nm.[100, 174, 187, 201] Considering the *I(V)*-characteristics of the anti phase boundary devices one can expect less Joule heating and thus either a smaller filament diameter or less oxygen vacancies forming. It is conceivable that an oxygen vacancy rich filament with a smaller diameter or less oxygen vacancies reoxidizes faster and thus has short retention time. A dependence of the retention time on Joule heating is also consistent with the current compliance dependence of the retention time. For a higher current compliance more Joule heating is expected and a higher time stability of the LRS is observed. Further it was shown that at high currents the diffusion of SrO to the $Pt/SrTiO_3$ interface is activated, which as described can stabilize the LRS.[174]

In this section it was shown that Ruddlesden-Popper type anti phase boundaries are not responsible for the enhanced performance of Sr-rich devices. However, Ruddlesden-Popper type anti phase boundaries can be utilized to obtain forming free devices. For this, in a first step, Ruddlesden-Popper type anti phase boundaries have to be successfully engineered into the $SrTiO_3$ thin film. In this section it was shown that this can be achieved by the deposition of 1.5 u.c. of SrO on an intentionally miscut TiO_2-terminated 0.5 wt% $Nb:SrTiO_3$ substrate. The additional SrO at the bottom interface induces horizontal and more important vertical Ruddlesden-Popper type anti phase boundaries. Extended defects in $SrTiO_3$ are known to pinpoint native oxygen vacancies.[7, 197–199] A probable explanation for forming free devices are thus preformed filaments along the anti phase boundaries. This should in future be further investigated. One possibility would be to calculate the formation energy of oxygen vacancies at the Ruddlesden-Popper type anti phase boundaries.

5.2.2 Additional SrO at the top interface

In this section the second accommodation mechanism for Sr-surplus in Sr-rich thin films will be investigated with regard to its influence on the switching behavior. For this purpose SrO islands are grown on top of stoichiometric $SrTiO_3$ films. The resulting devices will then be investigated paying special attention to the possibility to tailor the time stability of the LRS.

Figure 5.10 shows the topography of the as-grown thin films acquired by AFM of a) a stoichiometric thin film and b) a Sr-rich thin film as presented in chapter 4.2. The stoichiometric $SrTiO_3$ is atomically flat, while the Sr-rich STO film shows SrO islands.

In order to emulate the SrO segregation of Sr-rich thin films, additional SrO was deposited after the deposition of a 20 nm thick stoichiometric thin film. Figure 5.10 f) shows the RHEED oscillations for the growth of SrO. Due to the higher atom form factor of Sr in comparison to Ti a maximum in the intensity of the secondary spots (blue and green) corresponds to a SrO termination as discussed in chapter 4.2.[61, 182, 183] The oscillation of secondary spots and the additional oscillation of the main spot (red) thus correspond to the layer-by-layer growth of 1.5 unit cells (u.c.).[61]

Further deposition of SrO results in the formation of SrO islands, shown for 2 u.c. in Figure 5.10 d) and 3 u.c. in Figure 5.10 e). The increase of the amount of the additional SrO results in a higher SrO island density, while the individual islands show a similar height. The increased surface roughness results in the vanishing of the RHEED signal (Figure 5.10 f)). The transition to 3D growth can be explained by the different lattice parameters of $SrTiO_3$ and SrO. While SrO has a rock salt structure with a lattice constant of a = 0.51 nm, $SrTiO_3$ is a perovskite with a = 0.39 nm.[49, 202, 203] The high lattice mismatch results in a high stress, which in turn results in a transition to 3D growth to release the strain.

Having successfully deposited SrO on top of $SrTiO_3$ the samples were electrically characterized. Figure 5.11 shows the *I(V)*-characteristics for a 10 mA current compliance of the devices with different SrO thicknesses and as a reference the *I(V)*-characteristics of a stoichiometric and Sr-rich device.

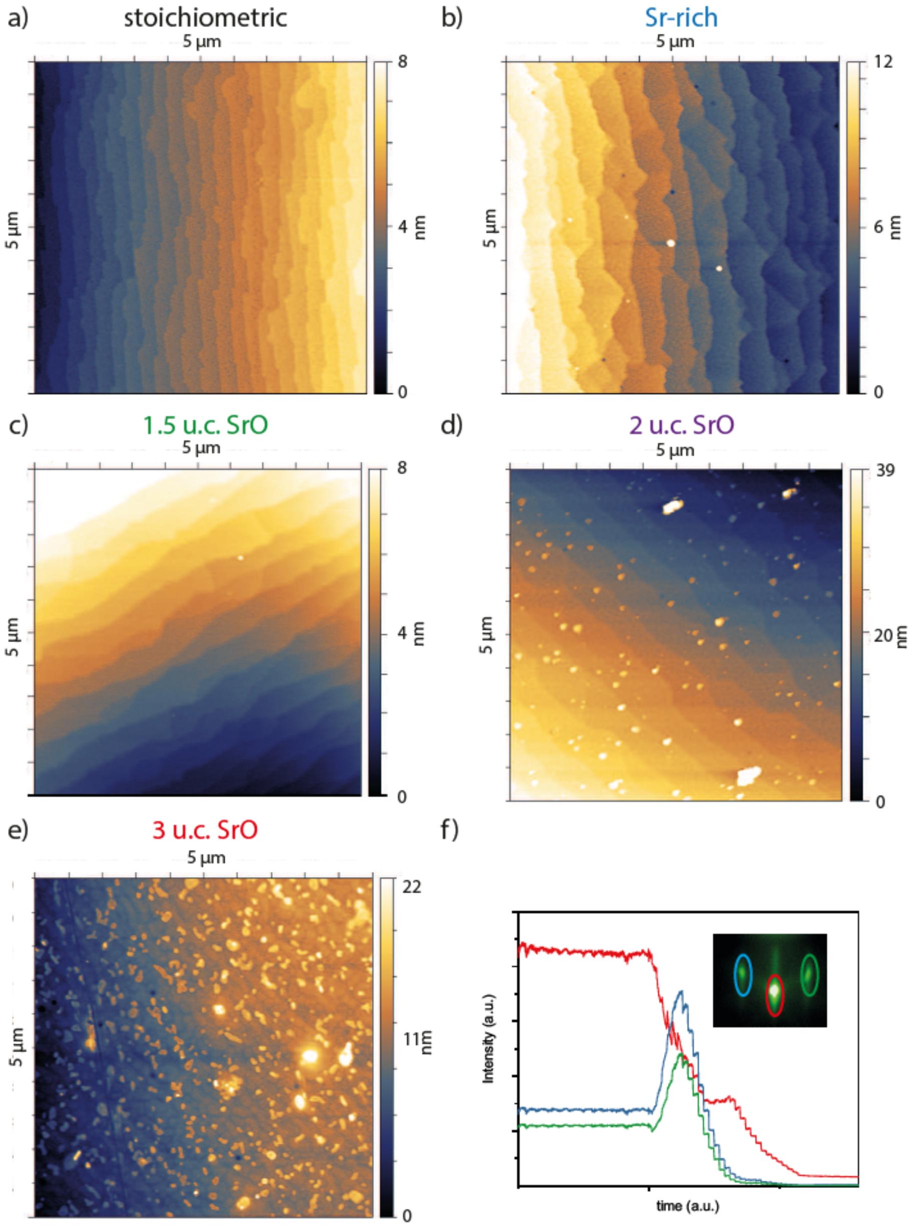

Figure 5.10: AFM topography images of a) stoichiometric SrTiO$_3$, b) Sr-rich SrTiO$_3$c) 1.5 u.c. of SrO deposited on top of a stoichiometric thin film, d) 2 u.c. and e) 3 u.c., respectively. f) shows the RHEED oscillation recorded during the deposition of SrO. The inset shows the RHEED pattern corresponding to the oscillations.

For the devices with additional SrO at the top interface the forming step gets increasingly more pronounced with an increasing amount of additional SrO. The similarity of the *I(V)*-characteristics for the Sr-rich $SrTiO_3$ devices and the devices with intentionally inserted SrO is a first hint towards the same underlying mechanism. For both a significant current starts at the comparably high voltage of 1 V (compare stoichiometric: 0.5 V).

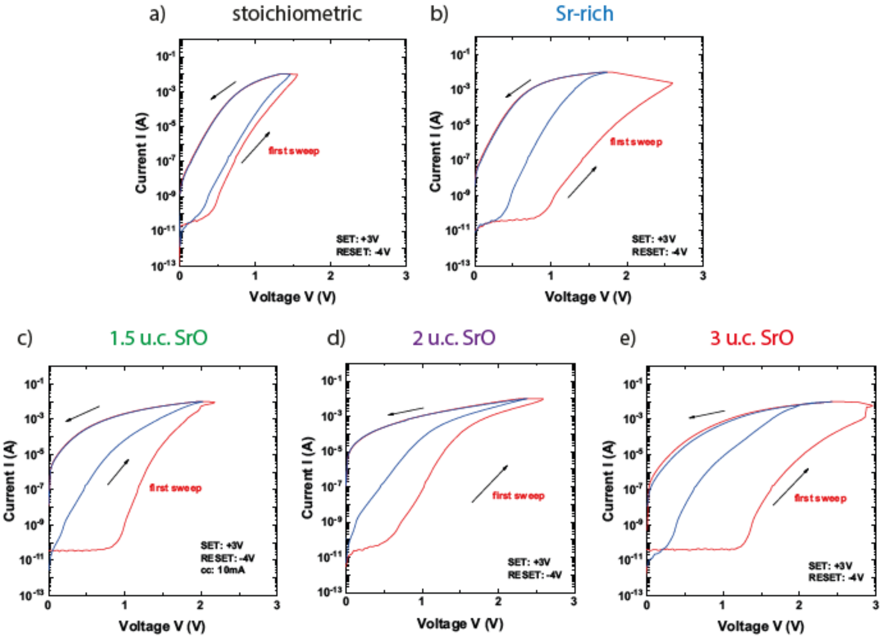

Figure 5.11: *I(V)*-characteristics for a current compliance of 10 mA of a) a stoichiometric, b) a Sr-rich device and devices with additional c) 1.5 u.c. SrO, d) 2 u.c. SrO and e) 3 u.c. SrO

Figure 5.12 shows the *I(V)*-characteristics for a current compliance of 30 mA. Basically the same trend as for 10 mA can be observed.

Figure 5.13 a) shows the LRS resistance immediately after the SET for samples switched with 10 mA current compliance. The error bars in Figure 5.13 correspond to the standard deviation of at least six switched devices. As described in chapter 5.1 the stoichiometric devices (black) have the highest LRS and the lowest HRS

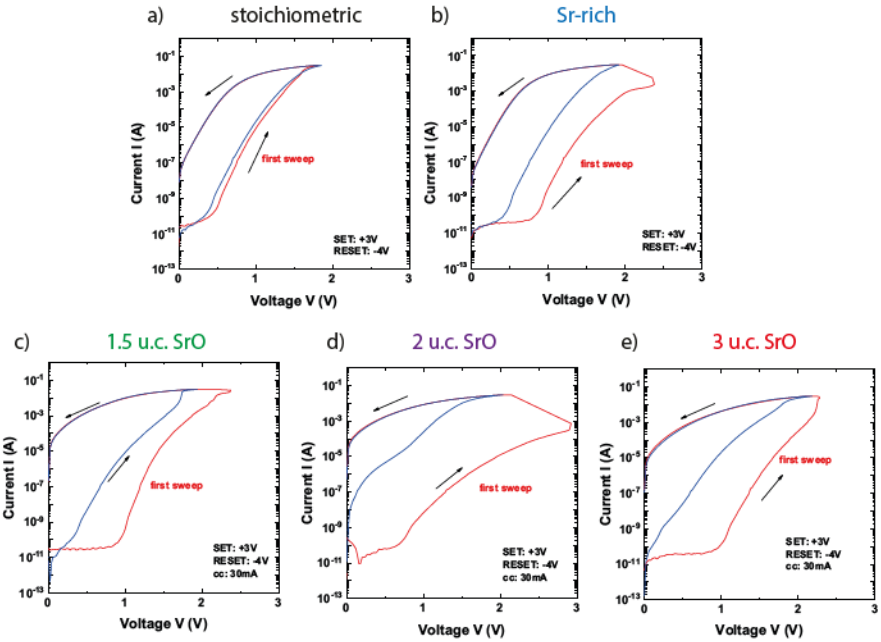

Figure 5.12: *I(V)*-characteristics for a current compliance of 30 mA of a) a stoichiometric, b) a Sr-rich device and devices with additional c) 1.5 u.c. SrO, d) 2 u.c. SrO and e) 3 u.c. SrO

(Figure 5.13 b) black HRS). The LRS of the Sr-rich devices (blue) is one order of magnitude lower and the HRS (Figure 5.13 b) blue HRS) is one order of magnitude higher. Their memory window is thus two orders of magnitude larger. All devices with additional SrO at the top interface show an even lower LRS resistance. Taking the error into account, the LRS of devices with additional SrO at the top interface is rather independent of the thickness of the SrO. Their HRS, however is lower than for the Sr-rich devices (Figure 5.13 b) black HRS). They have thus a similar memory window as Sr-rich devices.

Although the LRS resistance measured immediately after the SET is independent of the SrO thickness, the LRS retention in Figure 5.13 b) is directly affected by it. While samples with an additional 1.5 u.c. of SrO (green) show a similar retention as stoichiometric devices (black), samples with an additional 2 u.c. SrO (pink) show a

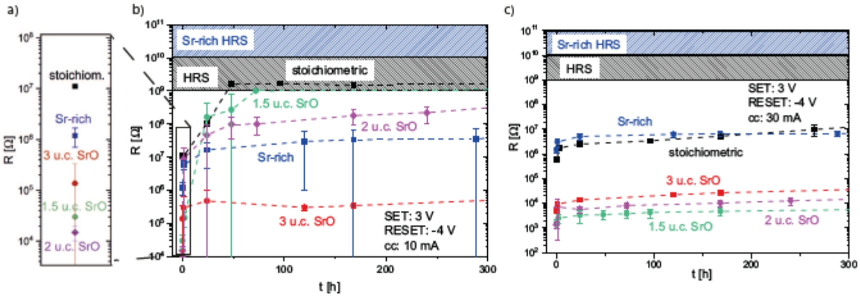

Figure 5.13: a) Resistance after forming with 10 mA, read out at 0.1 V, and retention for different thicknesses of the SrO at the interface in comparison with stoichiometric and Sr-rich SrTiO$_3$devices for forming with b) 10 mA and c) 30 mA.

similar retention behavior as Sr-rich devices (blue). Depositing a layer of 3 u.c. (red) even results in a significantly improved retention of the corresponding devices. However, their resistance still increases by a factor of two.

Of course, one could expect this trend to continue, when further increasing the SrO thickness. However, considering the already high surface roughness of the stoichiometric film with an additional 3 u.c. of SrO (Figure 5.10 e)), samples with additional 4 u.c were not fabricated.

Figure 5.13 c) shows the ON/OFF ratio and retention for samples switched with a 30 mA current compliance. Taking the error into account, the LRS of devices with additional SrO at the top interface is again independent of the thickness of the SrO. In contrast to the LRS achieved with 10 mA current compliance this LRS is, however, significantly lower, and thus also significantly lower than the LRS of stoichiometric and Sr-rich devices. While the LRS of stoichiometric and S-rich devices is $\approx 10^6$ Ω, the LRS of the devices with additional SrO on top is $\approx 10^3$ Ω. While Sr-rich devices still have exclusively a higher HRS, the ON/OFF ratio is now the highest for the devices with additional SrO, as it benefits from the much lower LRS. In particular the ON/OFF ratio is the lowest for the stoichiometric devices, $\approx 10^3$, intermediate for Sr-rich devices, $\approx 10^4$, and the highest for the devices with additional SrO, $\approx 10^6$. As expected for 30 mA (compare chapter 5.1) all devices have a stable retention over 300 h.

Figure 5.14 shows the variability of a) stoichiometric devices and b) Sr-rich devices as shown in figure 5.4 for comparison. Figure 5.14 c) shows the cycle to cycle variability (gray) and the resulting device to device variability (red) of devices with additional 3 u.c. of SrO at the Pt/$SrTiO_3$ interface. Interestingly the cycle to cycle variability of the device with 3 u.c. SrO is lower. The device to device variability, however, is higher, as indicated by the Weibull slope $\beta = 1.72$.

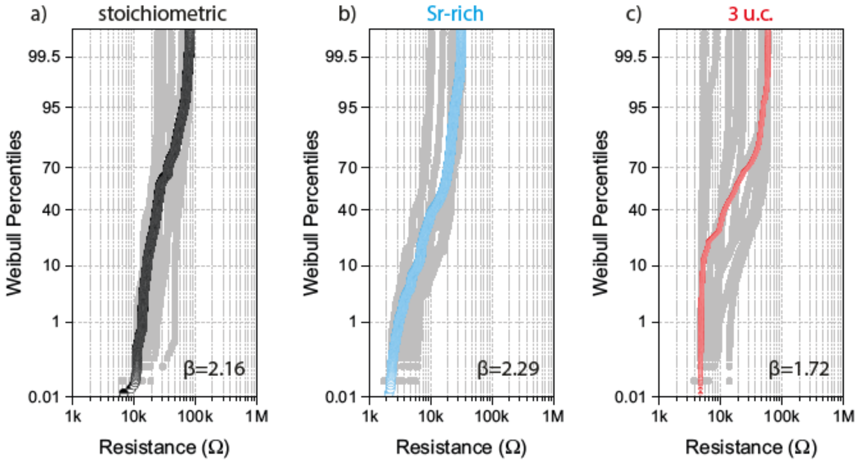

Figure 5.14: Cycle to cycle (gray) and device to device (colored) variability of a) stoichiometric devices, b) Sr-rich devices, and c) devices with additional 3 u.c. SrO at the Pt/$SrTiO_3$ interface.

Discussion and conclusion: Top interface engineering

In the beginning of this chapter two possible explanations were given for the enhanced switching performance of Sr-rich $SrTiO_3$, the stabilization of oxygen vacancies at growth induced extended defects [48] and the protection of the oxygen vacancy rich filament by the formation of SrO islands, acting as diffusion barriers [174]. We have considered the latter one in detail in this section by growing SrO of different thicknesses on top of stoichiometric $SrTiO_3$.

Considering the *I(V)*-characteristics in Figures 5.11 and 5.12 it is conspicuous that switching stoichiometric devices with additional SrO at the top interface results in a similar distinct forming step as switching Sr-rich devices. The distinct forming step is determined by the comparably higher voltage needed for a significant current. As SrO has a higher band gap than $SrTiO_3$[49, 203] it is a serial resistance with an additional higher barrier for the electrons to overcome. One explanation for the distinct forming step of Sr-rich devices can thus be the serial resistance of SrO islands, as it was possible to mimic it by SrO islands on stoichiometric $SrTiO_3$. Another explanation can be found in the oxygen diffusion blocking properties of the SrO. As oxygen vacancies are incorporated at the Pt/$SrTiO_3$ interface, the oxygen needs to overcome the higher SrO oxygen diffusion barrier, for which a higher field is necessary, thus resulting in a shift of the current increase to higher voltages, defining the distinct forming step.

Considering the time stability of the LRS, the similarities are verified. In the past it was postulated that SrO is an oxygen diffusion blocking layer and can thus act as retention stabilizing layer.[174] Considering the retention times in Figure 5.13 b), at least 2 u.c. of SrO are needed to form a LRS stabilizing layer. As shown in Figure 5.10 f) this corresponds to the transition from 2D to 3D growth and thus to the transition of the SrO from the perovskite to the rock-salt structure. It can thus be concluded that a mere termination change towards SrO is not sufficient for diffusion blocking of oxygen and thus the LRS stabilization, but at least 2 u.c. of SrO are needed. Increasing the thickness of the SrO to 3 u.c. results in an even more stable LRS, which is in good agreement with this understanding. Still the resistance increases by a factor of two, which can be explained by the island coverage of SrO at the surface, still exposing some channels for oxygen back-diffusion. This is consistent with the expected diameter of the filaments (100 - 500 nm)[174, 188, 201], which exceeds that of most SrO islands. The significant improvement of the LRS stability, when increasing the thickness of the SrO layer from 2 to 3 u.c., is in good agreement with the higher density of SrO islands, thus exposing less channels for the oxygen back diffusion. Comparing the diameter of the filaments with the thickness of the film it is clear that a lateral reoxidization plays a minor role. The LRS stabilization is schematically depicted in figure 5.15.

It is noticeable that both Sr-rich devices and devices with additional SrO show an increased memory window. However only Sr-rich devices have an increased HRS. This might be explained by the cation vacancies induced by the Sr-rich growth[106], which

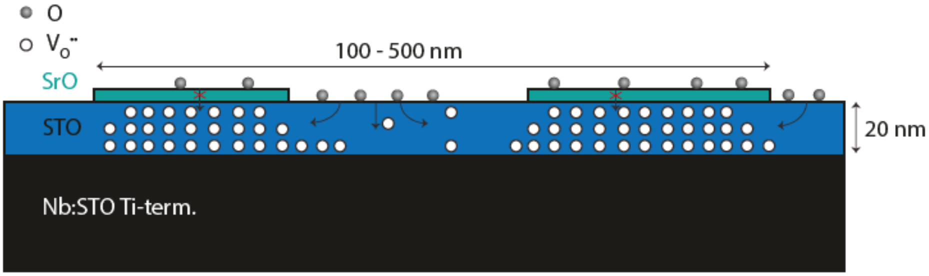

Figure 5.15: Reoxidization paths for the filament. The SrO islands are a diffusion barrier for the oxygen, the oxygen vacancy rich filament is thus stabilized underneath the islands.

are deep acceptors and consequently increase the resistance of the bulk $SrTiO_3$[48]. Both, Sr-rich devices and devices with additional SrO, show a lower LRS compared to stoichiometric devices. A low LRS thus seems to be related with SrO segregations. The mechanism behind the lower LRS, however, remains an open question at this point. This question will be addressed in chapter 7.

Devices with additional 3 u.c. SrO did further show a lower cycle to cycle variability and a higher device to device variability. The higher device to device variability is in accordance with the observation of Sr-rich devices having a higher device to device variability. In chapter 5.1 the higher device to device variability of Sr-rich devices was linked to an uneven distribution of the accommodation of Sr surplus during growth. Considering the topography shown in figure 5.10 e) an irregular distribution and morphology of SrO islands is mainly responsible for a high device to device variability. The responsible mechanism behind the decreased cycle to cycle variability can at this point, however, not be explained and will also be a addressed in the subsequent chapter.

In this section, the enhanced performance of Sr-rich $SrTiO_3$ devices was unraveled. The formation of SrO islands, which occur during Sr-rich growth of $SrTiO_3$ and during switching of the same, was artificially engineered by growing additional SrO on top of stoichiometric $SrTiO_3$ films. It was found that the deposition of 2 u.c. of SrO results in the same switching performance as observed for Sr-rich devices. It is possible to correlate the enhanced performance with the presence of SrO islands. Consistently following these results, the thickness of the SrO layer was further increased. This way devices with a further increased LRS time stability were obtained. The beneficent effect of SrO on the retention time was attributed to its high diffusion barrier for oxygen.

5.3 Summary: Engineering $SrTiO_3$ for resistive switching

Within this chapter, possibilities to engineer defects for $SrTiO_3$ thin films were presented and influences of these defects on the switching characteristics were investigated. One motivation behind this was to unravel the enhanced performance of Sr-rich thin film devices. To achieve this, two explanations were methodically tested. The first possibility considered was that Ruddlesden-Popper type anti phase boundaries within the Sr-rich thin film enhance its performance. To examine this, it was necessary to develop a technique to induce Ruddlesden-Popper type anti phase boundaries in thin films, without changing other properties. This was achieved by growing 1.5 u.c. of SrO on TiO_2-terminated 0.5 wt% Nb:$SrTiO_3$ substrates with an intentional miscut. This miscut prevented the SrO diffusion to the surface. While the resulting devices did not show the enhanced performance of Sr-rich devices, namely a large ON/OFF ratio and a time stable LRS, they were interestingly forming free. A possible explanation are preformed filaments, defined by an oxygen vacancy enrichment in the vicinity of the Ruddlesden-Popper type anti phase boundaries.

The other explanation is that the LRS of Sr rich devices is time stable because of the oxygen diffusion blocking effect of the SrO islands induced during forming and growth. Thus additional SrO was grown on top of stoichiometric films. The results showed that not only the enhanced performance of Sr-rich devices could be reproduced with devices with additional SrO at the top interface, but the performance could even be further improved. While the enhanced retention was unraveled within this chapter, the next step is to understand the enhanced ON/OFF ratio of Sr-rich devices, which was even further improved for devices with additional SrO at the top interface. This open question will be addressed in the next chapter.

6 Influence of the top electrode

In the previous chapter the mechanism behind the superior retention of Sr-rich $SrTiO_3$ devices was unraveled. This was achieved by depositing SrO on top of stoichiometric thin films. Those devices did not only show a similar LRS stability to Sr-rich devices, but an even more conductive LRS. In this chapter the mechanism behind the low LRS for devices with SrO islands and Sr-rich devices is revealed. This knowledge is then applied to influence the switching properties of $SrTiO_3$.

6.1 Role of Carbon

In chapter 5.2 it was shown that purposely growing SrO islands at the Pt/$SrTiO_3$ interface has a surprising influence on the LRS. While one would expect that additional SrO at this interface would, due to the high resistivity of SrO,[204] result in a serial resistance, the LRS is in fact lower as presented in table 6.1. Taking the error into account the LRS is comparably low for all investigated thicknesses of SrO at the Pt/$SrTiO_3$ interface. Independent of the current compliance the LRS is markedly lower for devices with SrO at the Pt/$SrTiO_3$ interface than for Sr-rich devices.

To unravel the reason behind the lower LRS for devices with additional SrO at the Pt/$SrTiO_3$ interface in comparison to Sr-rich devices, the surface chemistry of both is considered. *In-situ* XPS measurements were carried out for a Sr-rich $SrTiO_3$ thin film and a stoichiometric $SrTiO_3$ thin film with 3 u.c. SrO deposited on top. Figure 6.1 a)-c) shows the fits for the Sr-rich and d)-f) for the stoichiometric sample with 3 u.c. SrO on top. The chemical information is gained from these fits. The

Table 6.1: LRS of Sr-rich devices in comparison to devices with different thicknesses of additional SrO at the Pt/$SrTiO_3$ interface for 10 mA and 30 mA current compliance. The error corresponds to the standard deviation of at least six switched devices

Current Compliance	**10 mA**	**30 mA**
Sr-rich	1200 ± 500 kΩ	1400 ± 300 kΩ
1.5 u.c. SrO	30 ± 14 kΩ	1.6 ± 0.6 kΩ
2 u.c. SrO	14 ± 5 kΩ	1.3 ± 0.4 kΩ
3 u.c. SrO	140 ± 200 kΩ	5.0 ± 0.8 kΩ

comparisons in the right column shows the difference between the Sr-rich thin film (blue) and the stoichiometric thin film with additional 3 u.c. of SrO (red). The C 1s spectra are fitted with a Sr 3p component for the lowest binding energy, a hydrocarbon component ($E_B \approx 286$ eV) and a carbonate component for the highest binding energy. The O 1s spectra are fitted using 3 components. The lowest E_B component represents metal oxide bonds in the $SrTiO_3$ bulk. The highest E_B component represents carbonates.[167–169] The intermediate E_B can be ascribed to hydroxides and other non-carbonate contaminations, and is referred to as contaminations peak. The Sr 3d spectra are composed of a doublet from the $SrTiO_3$ bulk and a second, surface-related doublet at higher binding energies, as is typically observed for $SrTiO_3$.[170]

In order to estimate the surface chemistry, the peak areas of the different core-levels are compared. In case of the C 1s spectra the area ratio of the C 1s and Sr $3p_{1/2}$ peaks are used to obtain a C/Sr ratio. Further the area of the carbonate and the hydrocarbon peak are used to obtain a relative carbonate contribution. For the O 1s spectra, the areas of the carbonate and the contaminations peak in relation to the metal oxide peak are used to obtain a relative carbonate contribution and contamination concentration, respectively. The relative contribution of the Sr related surface component to the Sr 3d signal is obtained from the ratio of the doublet at high binding energy and the doublet from the bulk $SrTiO_3$.

These ratios can be found in Table 6.2. The C/Sr ratio of the sample with 3 u.c. of SrO is 4 %, while it is slightly lower for the Sr-rich sample, 1.3 %. Sr-rich $SrTiO_3$ shows a 4.1 % carbonate contribution. For 3 u.c. of SrO this ratio tenfolds to 46 %. The contamination concentration is again the highest for the 3 u.c. SrO sample,

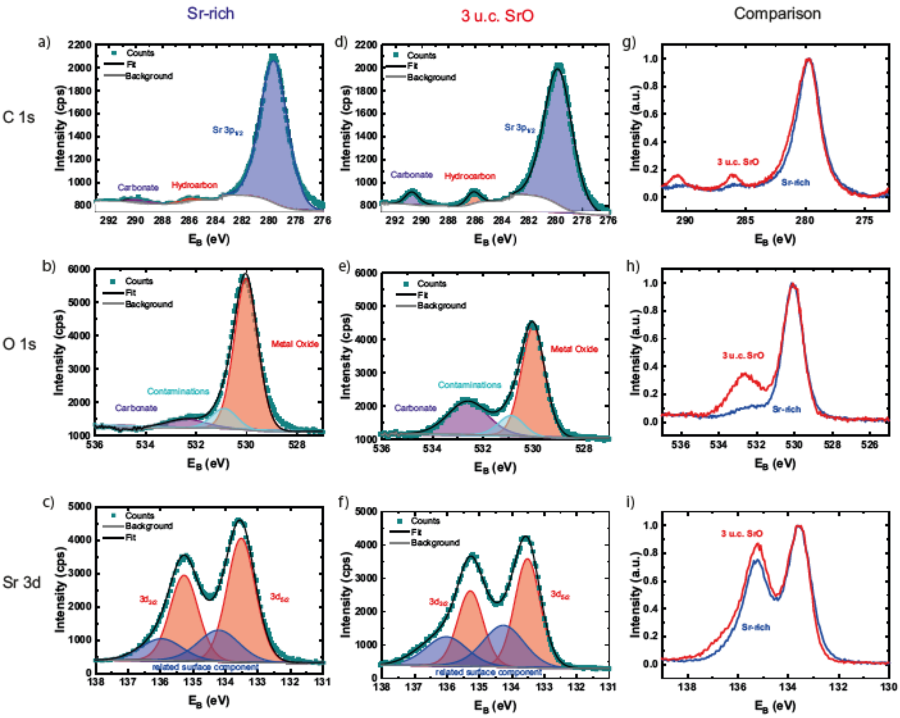

Figure 6.1: a)-c) Fits for the Sr-rich sample and d)-f) fits for the stoichiometric sample with 3 u.c. of SrO on top for the C 1s, O 1s and Sr 3d core levels, respectively. g)-i) A comparison between both samples for the same core levels.

51 %, while it is comparably lower for the the Sr-rich sample, 14 %. The carbonate contribution for the Sr-rich sample it is 10 % and for the 3 u.c. SrO sample it is double as high, 19 %. The Sr related surface component is 37 % for the Sr-rich sample and even higher for the 3 u.c. SrO sample, 55 %.

Considering the results of chapter 4.1 it is probable that the SrO on top of Sr-rich thin films and stoichiometric thin films with additional 3 u.c. of SrO reacts to $SrCO_3$ *in situ*, without ambient exposure. This can be explained by the residual CO_2 within the vacuum system.

Table 6.2 reveals that the C content increases for the much higher SrO surface coverage of the stoichiometric sample with additional 3 u.c. SrO in comparison to the

Table 6.2: Ratios obtained from XPS fits for *in situ* samples, for TiO_2-termination as reference, Sr-rich $SrTiO_3$ and stoichiometric $SrTiO_3$with 3 u.c. of SrO.

Sample	Sr-rich	3 u.c. SrO
C/Sr ratio (C 1s)	1.3 %	4.0 %
Carbonate contribution (C 1s)	4.1 %	46 %
Contamination concentration (O 1s)	14 %	51 %
Carbonate contribution (O 1s)	10 %	19 %
Sr related surface component (Sr 3d)	137 %	55 %

Sr-rich sample. In table 6.1 it was shown that the LRS decreases for samples with additional SrO at the Pt/$SrTiO_3$ interface. Thus in a next step these films are compared with regard to their *I(V)*-characteristics. To avoid additional contaminations by ambient exposure the Pt electrodes were deposited *in situ*.

Figure 6.2 shows the *I(V)*-characteristics for a Sr-rich (top) sample and a sample with additional 3 u.c. SrO on top (bottom). The left column shows the *I(V)*-characteristics for a 10 mA current compliance and the right column for a 30 mA current compliance.

The *I(V)*-characteristics of the Sr-rich sample with an *in situ* Pt electrode surprisingly reveal no hysteresis independent of the forming current. The stoichiometric film with an additional 3 u.c. of SrO on top on the other hand shows the expected *I(V)*-characteristics, namely a pronounced forming step and a hysteresis (compare chapter **??**).

Connecting table 6.2 and figure 6.2 it is conspicuous that only the sample with the highest carbon concentration at the Pt/$SrTiO_3$ interface shows a hysteresis. It thus seems that the Carbon at the top interface plays a crucial role for resistive switching. To investigate this in detail different thicknesses of carbon were DC sputtered *in situ* on top of stoichiometric thin films as described in chapter 3.2. Subsequently the Pt was evaporated *in situ* on top. With regard to table 6.2 stoichiometric thin films were chosen to avoid an uncontrollable high *in situ* C contamination.

The left column of figure 6.3 shows the *I(V)*-characteristics of samples with 0 - 1 nm of C switched with a 10 mA current compliance and the right column of samples switched with a 30 mA current compliance, respectively. As a reference figure 6.3 a)

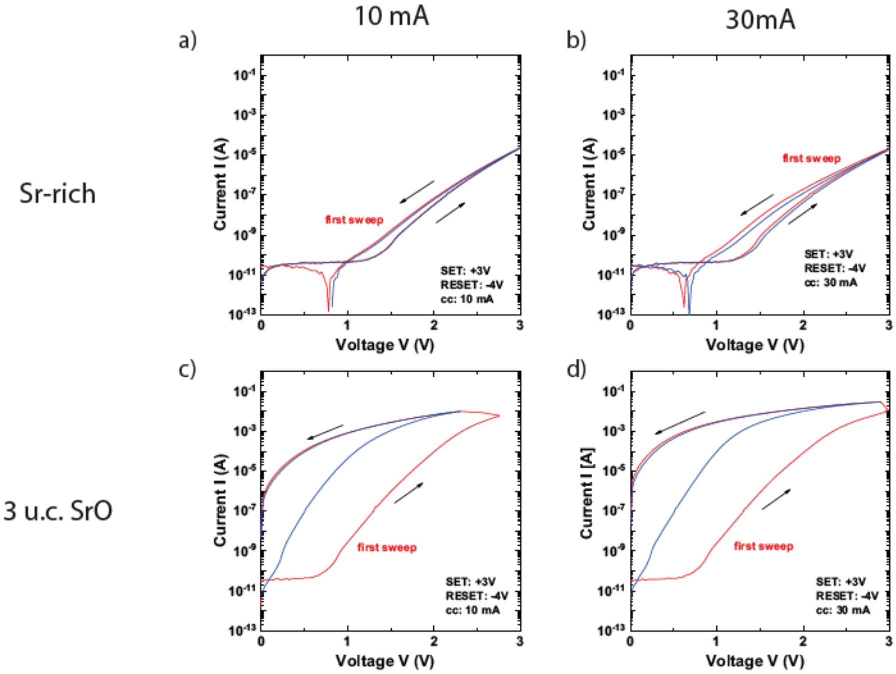

Figure 6.2: a) and b) *I(V)*-characteristics for a Sr-rich sample (top) and c) and d) a stoichiometric sample with additional 3 u.c. SrO on top (bottom) with an *in situ* top electrode. The left column shows the *I(V)*characteristics for a 10 mA current compliance and the right column for a 30 mA current compliance.

and b) shows the *I(V)*-characteristics of a stoichiometric samples with the previously used Pt top electrode. Here referred to as 'dirty', as it is deposited *ex situ* and using a graphite crucible.[189]

Figure 6.3 c) and d) shows the *I(V)*-characteristics of the stoichiometric sample with *in situ* Pt. Like for the Sr-rich sample presented in figure 6.2 no hysteresis is observable. For 1 nm of C sputtered in between the stoichiometric $SrTiO_3$ and the *in situ* Pt top electrode, figure 6.3 e) and f), a hysteresis is observable for both current compliances. While the SET (blue) is comparable to the SET of the reference devices in figure 6.3 a) and b), the forming step is slightly more pronounced. This is due to a higher voltage necessary to observe an increase of the current for the forming step. Possible reasons behind this will be discussed at a later point.

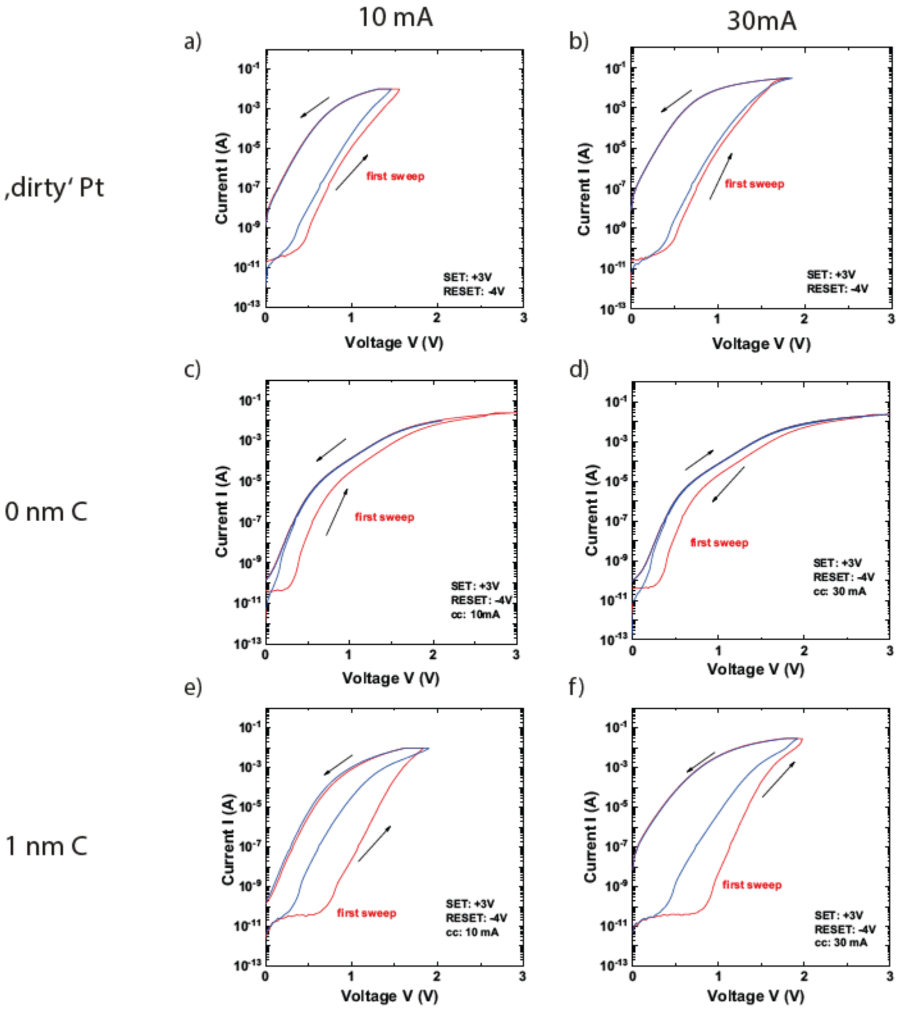

Figure 6.3: Left column: 10 mA current compliance; right column: 30 mA current compliance *I(V)*-characteristics of a) and b) stoichiometric $SrTiO_3$ with *ex situ* Pt c) and d) with *in situ* Pt e) and f) with *in situ* sputtered 1 nm C.

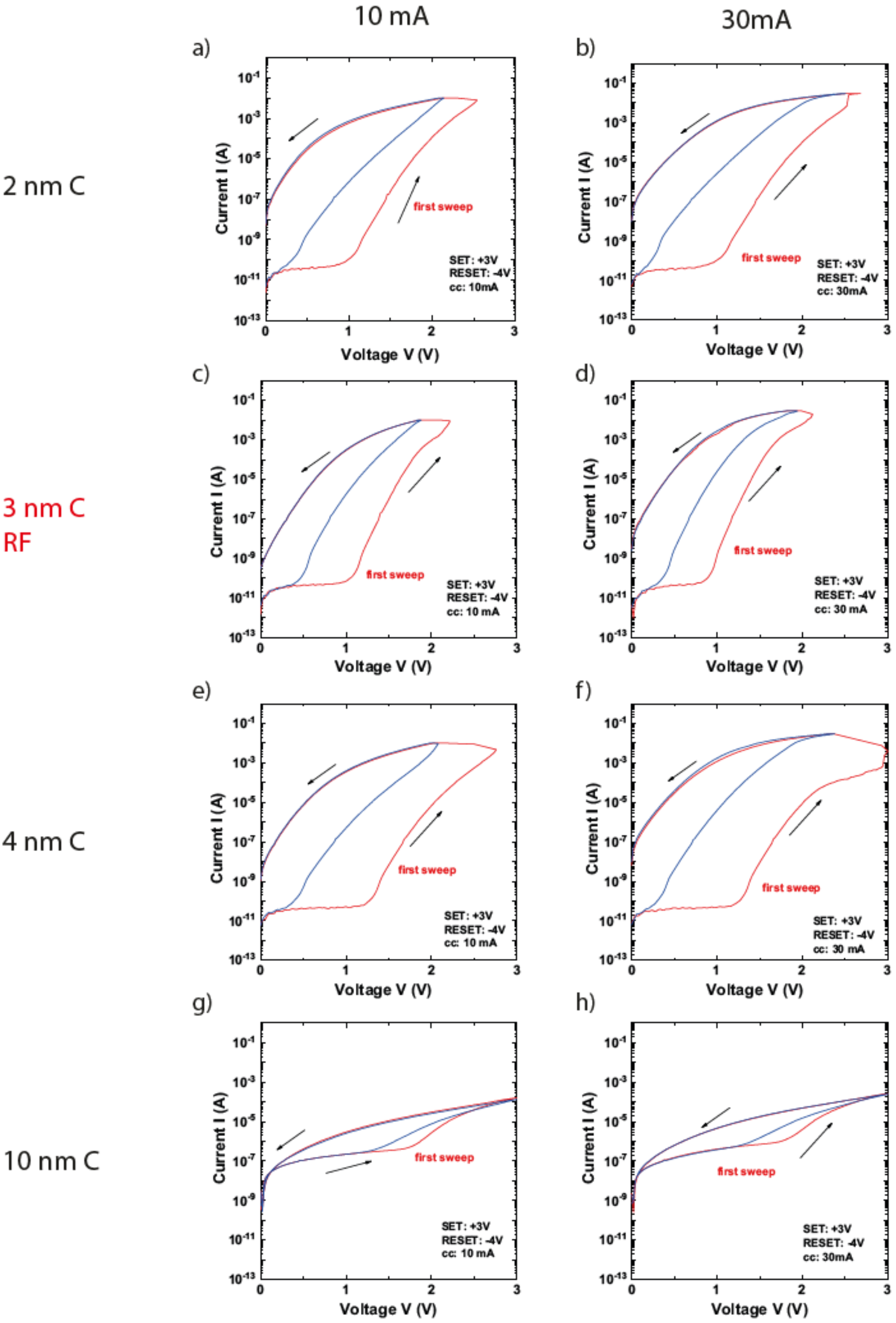

Figure 6.4: *I(V)*-characteristics shown in dependence of the carbon thickness. Left column: 10 mA current compliance; right column: 30 mA current compliance.

This confirms the necessity of carbon at the Pt/$SrTiO_3$ interface for the resistive switching of $SrTiO_3$. Consequently following this result, the thickness of the sputtered C layer was further increased. Figure 6.4 shows the resulting *I(V)*-characteristics for increasing the thickness of the sputtered C from 2 nm up to 10 nm. Again the left column shows the *I(V)*characteristics for 10 mA current compliance and the right column for 30 mA current compliance, respectively. It is worth noting that the 3 nm carbon layer in figure 6.4 c) and d) was not DC sputtered, but rather RF sputtered with a new parameter set, as described in chapter 3.2.

An increase of the carbon thickness between the $SrTiO_3$ and Pt to 2 nm results in a distinct forming step (red) as presented in figure 6.4 a) and b). Comparing the *I(V)*-characteristics of devices containing 2 nm C with devices containing 1 nm C as in figure 6.3 g) and h), it is noticeable that an increase of the interface C thickness is accompanied by an increase of the voltage necessary to observe a current increase. However, the *I(V)*-characteristics of the 3 nm C devices (figure 6.4 c) and d)) do not show the same trend. Rather the forming step is comparable to the devices with 2 nm C. This is probably linked to the change of deposition technique for the C. Considering the 4 nm C devices in figure 6.4 e) and f) the trend of an increased voltage necessary to observe an increase in current with an increased C thickness for the forming step is confirmed.

Figure 6.4 g) and h) show the *I(V)*-characteristics for a drastically increased thickness of C. The sputtered C here is 10 nm, thus half the thickness of the active switching layer $SrTiO_3$. While a hysteresis is still observable to some degree, it shows no permanent resistance change.

In the next step the role of the carbon at this interface for the ON/OFF ratio and thus the LRS will be considered. Figure 6.5 shows the LRS and HRS for stoichiometric devices with different thicknesses of sputtered C at the *in situ* Pt/$SrTiO_3$ interface. As expected for *I(V)*-characteristics lacking a hysteresis the HRS and LRS of devices with 0 nm C, 0.1 nm C and 10 mm C are equal independent of the current compliance.

Considering the devices, which actually have the desired hysteresis, the LRS (light blue) of a device with 1 nm is comparably high; $\approx 10^9\ \Omega$ in comparison to $\approx 10^7\ \Omega$ for the 'dirty' reference sample. Its HRS (dark blue) is, however, also one order of magnitude higher ≈ 10^{10} Ω. This results in an ON/OFF ratio of 10. Again comparing this ratio to the reference, 10^2, it is comparably low. Increasing the C thickness to 2 nm results in a decrease of the LRS to ≈ 5×10^6 Ω and a decrease of the HRS to ≈ 5×10^9 Ω. The resulting ON/OFF ratio has thus markedly increased to 10^3.

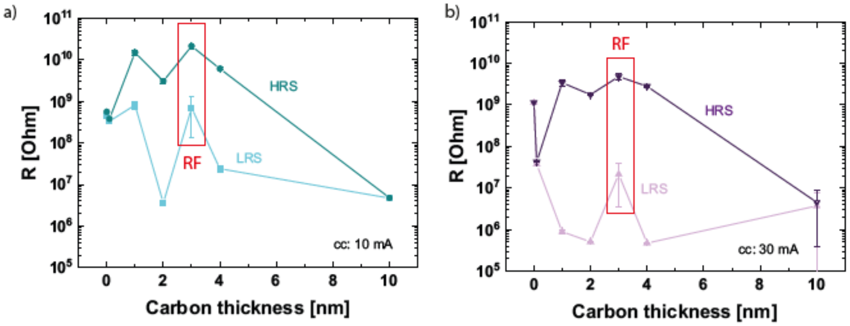

Figure 6.5: LRS and HRS in dependence of the additional C at the Pt/$SrTiO_3$ interface for a) 10 mA current compliance and b) 30 mA current compliance. The error bars correspond to the standard deviation of at least six switched devices.

As mentioned before, the 3 nm C were RF sputtered in opposite to the other carbon thicknesses. The device with 3 nm C does also not follow the *I(V)*-characteristic trend as discussed for figure 6.4. In figure 6.5 a) it is obvious that the LRS and HRS of the RF sputtered C devices is rather similar to the LRS and HRS of the devices with 1 nm C. It thus seems that the structure of the carbon to some extend influences the switching characteristics. Henceforth the 3 nm RF-sputtered carbon will be excluded from discussion. Increasing the C thickness further to 4 nm and returning to DC sputtered C results in a HRS similar to the 2 nm C devices. The LRS slightly increases to ≈ 10^7 Ω. The resulting ON/OFF ratio is thus 5×10^2.

In chapter 5.1 it was shown that stoichiometric devices show an improved ON/OFF ratio when increasing the current compliance to 30 mA. Considering the results presented in figure 6.5 b) this is also true for devices with carbon at the Pt/$SrTiO_3$ interface. The LRS (pink) of a device with 1 nm decreases to ≈ 10^6 Ω, while its HRS (violet) changes to ≈ 5×10^9 Ω. The resulting ON/OFF ratio is thus 5×10^3 for 30 mA current compliance instead of 10 for 10 mA current compliance. For 2 nm

C and 4 nm C the ON/OFF ratio increases to 5×10^3 as well. It thus seems that the C thickness is less influential on the ON/OFF ratio for a higher current compliance.

At this point it is clear that the carbon at the interface between Pt and $SrTiO_3$ influences the LRS. In particular a certain amount of C is necessary to even allow resistive switching. If enough carbon is available to allow switching, an increase of the C at the interface results in a lower LRS until a minimum is reached. Following the retention time of the LRS of the stoichiometric devices with different thicknesses of C at the Pt/$SrTiO_3$ interface that showed resistive switching was investigated.

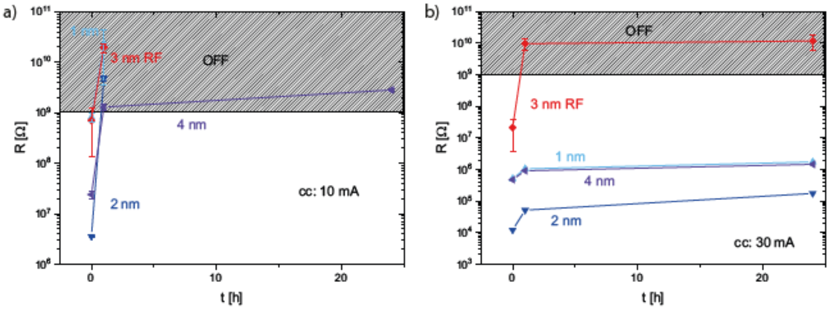

Figure 6.6: Time stability of the LRS for different thicknesses of carbon at the PT/$SrTiO_3$ interface for a) 10 mA current compliance and b) 30 mA current compliance.

Figure 6.6 shows the LRS time stability for a) switching with a 10 mA current compliance and b) switching with a 30 mA current compliance. As for 'dirty' stoichiometric devices (compare chapter 5.1) the retention time is short for all devices switched with a 10 mA current compliance. For a 30 mA current compliance all devices with DC sputtered carbon have a time stable LRS, also comparable to the 'dirty' stoichiometric devices. Again the RF sputtered C devices deviate from this observation, as they do not show a time stable LRS, even for a 30 mA current compliance. This is another hint that the structure of the C plays a crucial role for the switching properties of $SrTiO_3$ based devices.

Overall the C at the Pt/$SrTiO_3$ interface does not have a noticeable influence on the retention of $SrTiO_3$ devices. The retention thus is, as discussed in the previous chapter, stabilized by oxygen diffusion blocking.

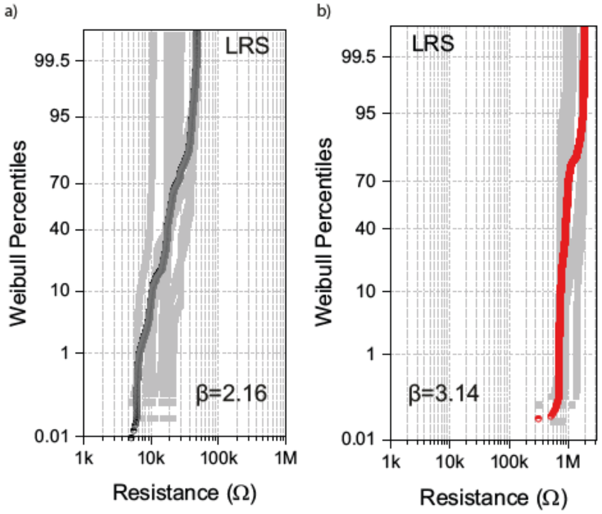

Figure 6.7: Cycle to cycle (gray) and device to device (colored) variability of the LRS of a) 'dirty' Pt devices as reference and b) the of devices with 2 nm RF sputtered carbon at the $Pt/SrTiO_3$ interface. The device to device variability results from averaging the cycle to cycle variabilities.

Last the variability of a device with additional 2 nm of C is investigated in figure 6.7. The LRS in figure 6.7 b) has a low device to device (red) variability and an extraordinarily low cycle to cycle variability (gray) compared to any other shown in this work before, represented by stoichiometric devices with 'dirty' Pt in figure 6.7 a). As is evident considering their Weibull slopes β. (compare chapter 5.1)

Discussion and conclusion: The role of carbon

This chapter started with the investigation of a possible reason behind the lower LRS of devices with supposedly SrO at the $Pt/SrTiO_3$ interface. It was found that

SrO forms marked amounts of $SrCO_3$. To investigate the influence of the C at the Pt/$SrTiO_3$ interface on the resistive switching properties, different thicknesses of C were deposited *in situ* on stoichiometric $SrTiO_3$. It was found that increasing the C thickness resulted in an increase of the voltage during forming that is needed to measure an increase in current. This will be discussed later in this section. It was found that the optimal thickness of the C interlayer is between 2 and 4 nm, resulting in the highest ON/OFF ratio. Additionally devices with 2 nm C have an extraordinary low cycle to cycle variability. Devices with below 1 nm C did not show a switching event at all. C is thus a prerequisite for resistive switching. However, it was also observed that the deposition technique of the carbon layer plays a central role for the resulting properties.

Having established that C is necessary for resistive switching of $SrTiO_3$ and does directly influence the LRS, the next step is to understand the mechanism behind this. To identify the responsible mechanism different approaches derived from existing literature are considered:

1) An intrinsic defect rich layer at the Pt/Nb:$SrTiO_3$ interface[92]

   This is the most obvious explanation that can be found in literature, as it describes the dependence of resistive switching in Nb:$SrTiO_3$ of the top electrode. Similar to the here presented results they found that the occurrence of a switching event depends heavily on the choice of deposition technique for the top electrode. Their explanation focuses on the necessity of charge trapping at an unintentionally induced intrinsic defect rich layer at the Pt/Nb:$SrTiO_3$ interface.[92] Their result states that the choice of the deposition technique for the Pt determines this intrinsic defect rich layer at the Pt/Nb:$SrTiO_3$ interface; i.e. that sputtering of Pt causes less defects than thermal evaporation.[92, 205]

   As this explanation is based on the defects induced by the deposition of Pt, it is, despite the similarities, not suited to explain the here observed results. Firstly, the general assumption that sputtering induces less defects than thermal evaporation is not unequivocally true, but rather depends on the deposition parameters and the involved materials.[205–210] Secondly, the here presented results differed in either the exposure to ambient and residuals ('dity' Pt) or the thickness of the purposefully induced Carbon layer. The deposition technique for the Pt did not change (compare chapter 3.2). This explanation will thus be disregarded.

2) The enhancement of catalytic activity using Pt with a carbon intermixing in comparison to pure Pt[211–214]

In the field of catalysis and fuel cells it is well known that the activity of Pt as a catalyst can be improved by the introduction of carbon.[211–214] In the picture of resistively switching $SrTiO_3$ one could consider the Pt top electrode as catalytic active material for the formation of oxygen vacancies. It is thus conceivable that the Pt electrode would need to be catalytically activated by the addition of C, as for example in the case of certain fuel cells.[214]

In general catalytic activities can be measured by cyclic voltammetry, allowing the measurement of the activity of the Pt electrode, with and without additional carbon.[215] During measurements conducted in the course of this work no differences were observable, more frankly no peaks were observable in the voltammograms. However, this must not necessarily mean that this explanation can be ruled out, as single crystal $SrTiO_3$ is a poor ionic conductor,[216] thus making cyclic voltammetry measurements difficult.[217]

3) Energetically favorable formation of CO_2 or CO in comparison to O_2

This explanation is based on the rate determining step for the surface reaction during oxygen exchange for $SrTiO_3$, which is the formation of O_2.[56, 143] Considering Hess's law O_2 has per definition a standard enthalpy of formation of 0 kJ/mol. Thus, the formation of either, CO or CO_2, is thermodynamically more favorable then the formation of O_2. The corresponding enthalpies can be found in table 6.3.

Considering the enthalpies it is probable that, if C is available, the formation of oxygen vacancies is energetically more preferable than without the presence of C. This explanation is conclusive considering the absence of a switching event in case of the absence of C. The formation of O_2, which would be necessary in the absence of C, requires significantly more energy, which may not be provided by the system. This could also be the underlying mechanism of explanation 2).

Table 6.3: Enthalpies of possible reactants during the filament formation in $SrTiO_3$

	ΔH (kJ/mol)
C, O_2	0
CO	-111
CO_2	-282

4) A carbon heating layer as patented for PCMs[218]

This explanation is based on a patent that suggest a carbon containing interfacial layer for an improvement of performance in PCMs based on thermal confinement induced by said interfacial layer.[218] A thermal confinement is desirable for PCMs as the switching mechanism is mainly heat driven. Thus heat confinement can prevent the undesirable exposure of non-active parts of the sample to heat and at the same time can increase the locally induced heat, ultimately decreasing the power consumption.[219]

Basically the idea of improving performance by thermal confinement could also be applied to resistive switching of $SrTiO_3$. As described in the previous chapter 5.2, Joule heating is an important factor for the formation of the oxygen vacancy rich filament including the surface reaction of the oxygen vacancy formation and their diffusion.[93, 95, 100] For a higher local Joule heating an enhanced oxygen vacancy formation and diffusion can be expected, resulting in better conducting filaments.

Considering the thermal conductivity of carbon, however, it is surprising that it was suggested by Xu as thermal confinement layer.[218] The thermal conductivity of carbon is indeed higher than of most materials.[220] Considering the results of table 6.2 not only carbon can be found at the Pt/$SrTiO_3$ interface, but also $SrCO_3$, which exhibits a very low thermal conductivity[221].

The role of C for resistive switching would thus be a reaction with SrO to form a thermal confinement layer of $SrCO_3$. In the absence of C the confinement layer does not form and thus the local Joule heat is not sufficient to enable a filament formation. Increasing the C thickness increases the thermal confinement and thus the local Joule heating, ultimately resulting in an increased oxygen vacancy formation and diffusion, until a saturation is reached. At this point additional C may not contribute to the confinement layer, as it may remain C.

The formation of a $SrCO_3$ thermal confinement layer can also explain the shift to higher voltages needed to measure an increase in current with an increasing C thickness and for samples with SrO at the top interface. In the previous chapter two possible explanations were given for this observation. One was the serial resistance of the SrO islands. However, above results suggest that SrO islands on the $SrTiO_3$ surface form $SrCO_3$. Considering the much smaller band gap of $SrCO_3$ (3.17 eV)[222] compared to the one of SrO (5.22 eV)[203], this explanation is unlikely. The other explanation was the necessity of a higher voltage in order to overcome the SrO oxygen diffusion barrier. This explanations seems likely, as $SrCO_3$ has, like SrO, a high diffusion barrier for oxygen[223] and can explain the shift also for samples with additional C at the Pt/$SrTiO_3$ interface.

To determine which of the above mechanisms is in fact responsible for the influence of carbon for resistive switching in $SrTiO_3$, its influence is investigated for a c8w-switching MIM structure. The inlet of figure 6.8 shows the MIM structure used for c8w-switching. For forming a positive voltage is applied to the top, Schottky-type, interface. Thus the switching does not rely on an oxygen exchange with the atmosphere or the Schottky-type interface, but relies, as described by the disc-plug model in chapter 2.3, on an internal rearrangement of the oxygen vacancies.

Explanation 1) was already found not to be responsible, explanations 2) and 3) are based on influences on the oxygen vacancy formation, while explanation 4) is based on a confinement of the Joule heating. Thus carbon should only have an influence on c8w-switching in the considered setup, if explanation 4) is responsible.

Figure 6.8 shows the *I(V)*-characteristics of Metal/(C/)Ta_2O_5/Ta/SiO_2 MIM structures. For the top row the metal is gold and for the bottom row platinum. The left column shows the *I(V)*-characteristics without additional C and the right column with additional 2 nm of C.

The top row of figure 6.8 shows the *I(V)*-characteristics of a) a Au/Ta_2O_5/Ta/SiO_2 MIM and b) of a Au/C/Ta_2O_5/Ta/SiO_2 MIM. Equally to the influence of C on the

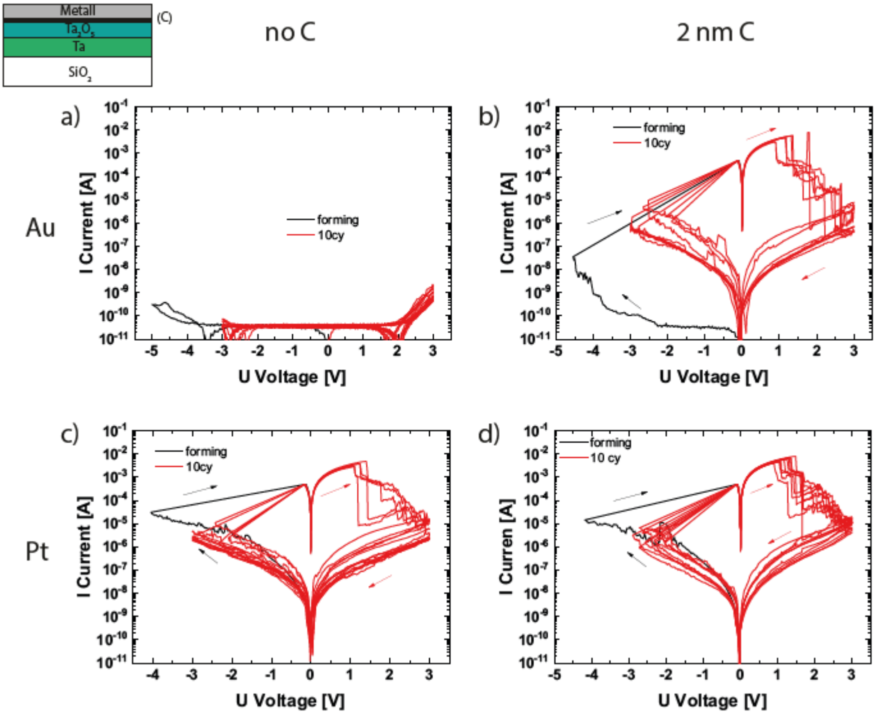

Figure 6.8: *I(V)*-characteristics of Ta_2O_5/Ta with a) and b) Au and c) and d) Pt top electrode. The left column shows the *I(V)*-characteristics without and the right with additional C.

8w-switching $SrTiO_3$ an absence of C for this MIM results in the absence of resistive switching. Considering above explanations this confirms explanation 4), as it is the only one not restricted to an oxygen exchange with the atmosphere or stored oxygen in the Schottky-electrode, but instead explains the influence of C by a confinement of the Joule heating.

In a next step the Au top electrode was exchanged for a Pt top electrode. As Pt has a lower thermal conductivity[224] than Au[225], this should be beneficial for the switching of Ta_2O_5. Figure 6.8 c) does reveal that, when using a Pt top electrode, in fact switching occurs without the addition of C to the interface. Adding C to the Pt/Ta_2O_5 does not show any observable effect, as shown in figure 6.8 d). This is not surprising as the thermal conductivity of C[220] is similar to the one of Pt[224].

For $SrTiO_3$ based MIMs the formation of $SrCO_3$ is responsible for the thermal confinement layer. While the formation of tantalum carbides is due to their formation energy unlikely,[226] but cannot be excluded,[227] their thermal conductivity is also rather high.[228]

Summarizing, in this chapter the influence of the top electrode on resistive switching was unraveled. In particular it was found that the thermal conductivity of the top electrode plays a central role for the occurrence of a switching event and for the resulting LRS. If the thermal conductivity is below a case dependent threshold value, no switching event occurs, lowering the thermal conductivity results in a successive lower LRS. The reason behind this is a local confinement of the heat induced during the switching. The heat in turn accelerates all rate limiting steps, resulting in a lower LRS. It was shown that this theory is valid for 8w- and c8w-switching MIMs independent of the active oxide, it is thus valid for all VCM systems. It can further explain the lower LRS for samples with intentional or unintentional SrO at the top interface (compare chapter 5.2), which was shown to form $SrCO_3$.

Introducing an additional thermal confinement layer was shown to decrease the variability and allow an adjustment of the LRS. The next steps should thus be to try and use the influence on the variability of the heat confinement to control it.

6.2 Carbon patterns

In the previous chapter it was shown that carbon is necessary at the Pt/$SrTiO_3$ interface to enable resistive switching. It was further shown that intentionally introducing it can result in a lower variability. In this chapter the possibility of controlling the filament position utilizing this knowledge will be tested. Controlling the filament position could ultimately result in the possibility to control the variability, which is highly desirable for the emerging field of neuromorphic computing, where this could be used to introduce stochasticity and thereby improve the learning efficiency of a neural network.[229–233]

The idea behind variability control is that this group has recently shown that a main reason behind the high variability of $SrTiO_3$ devices is the formation of multiple filaments during the first SET, of which different filaments can be active in subsequent SETs and RESETs.[201] As it was shown in chapter 6.1, carbon is necessary to enable switching in $SrTiO_3$. If it is possible to introduce a carbon pattern at the Pt/$SrTiO_3$ interface, it should thus be possible to pinpoint the filament position and, thus, to decrease the variability. Controlling the number of carbon patterns, it might be possible to control the variability.

To provide patterned C-pads at Pt/$SrTiO_3$ interface in a simple way an SEM was used. The electron beam of the SEM can condense the residual C of the background pressure and in that manner form a carbon layer.[234] Figure 6.9 shows a) one carbon pad, b) two carbon pads and c) three carbon pads acquired by focusing the beam with a 220 x magnification, 15 kV acceleration voltage and 80 s exposure time. Additional single pads with a doubled exposure time were fabricated.

To investigate the morphology of the deposited carbon pads the topography was investigated. Figure 6.10 a) shows the topography of a single carbon pad and c) of three carbon pads next to each other, b) and d) show the respective line profiles.

The topography of the single carbon pad is homogeneous. The rectangular pad, $\approx$ 2 x 2 μm^2, directly written with the e-beam of the SEM is well defined and has a height of approximately 4 nm. Around the rectangular pattern a circle with

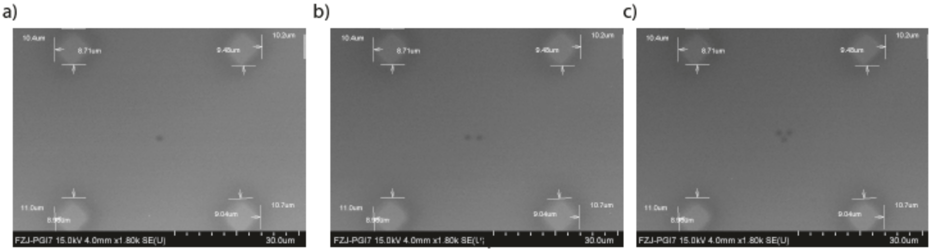

Figure 6.9: a) one carbon pad, b) two carbon pads and c) three carbon pads achieved by utilizing the carbon deposition effect during SEM.

a height of 2 nm is visible. The circle probably results of the e-beam changing directions at the edge of the pattern and thus exposing the surrounding area. In the previous chapter it was shown that the optimal carbon thickness for resistive switching in $SrTiO_3$ is between 2 and 4 nm. The carbon pad is thus a promising seed for filament formation. The topography of the three carbon pads in vicinity of each other reveals a decrease of the homogeneity. The pad deposited first (top left) looks similar to the single pad in figure 6.10 a). The subsequently deposited pads show a less defined rectangular structure, while the circular pattern around it remains unchanged.

After successfully depositing a C pattern at the $Pt/SrTiO_3$ interface, the next step is to investigate its influence on resistive switching. Figure 6.11 shows the results including reference devices, which have no C pad, however a C contamination is expected, as an *ex-situ* transfer to the SEM is necessary and the SEM will also deposit small amounts of carbon contaminations in areas, where it is not intended. All different numbers and thicknesses of C pads presented in figure 6.11 were measured on the same $SrTiO_3$ film, as was the reference.

The *I(V)*-characteristics shown in figure 6.11 a) to d) show a first sweep that is slightly different from the subsequent SET, however no distinct forming step is visible as for samples with similar C thickness (compare figure 6.4). The *I(V)*-characteristics are similar to the *I(V)*-characteristics of 'dirty' Pt samples (compare figure 6.3). This is conceivable as they were exposed to ambient. Considering the *I(V)*-characteristics no influence of C thickness, pad number or even presence is observed.

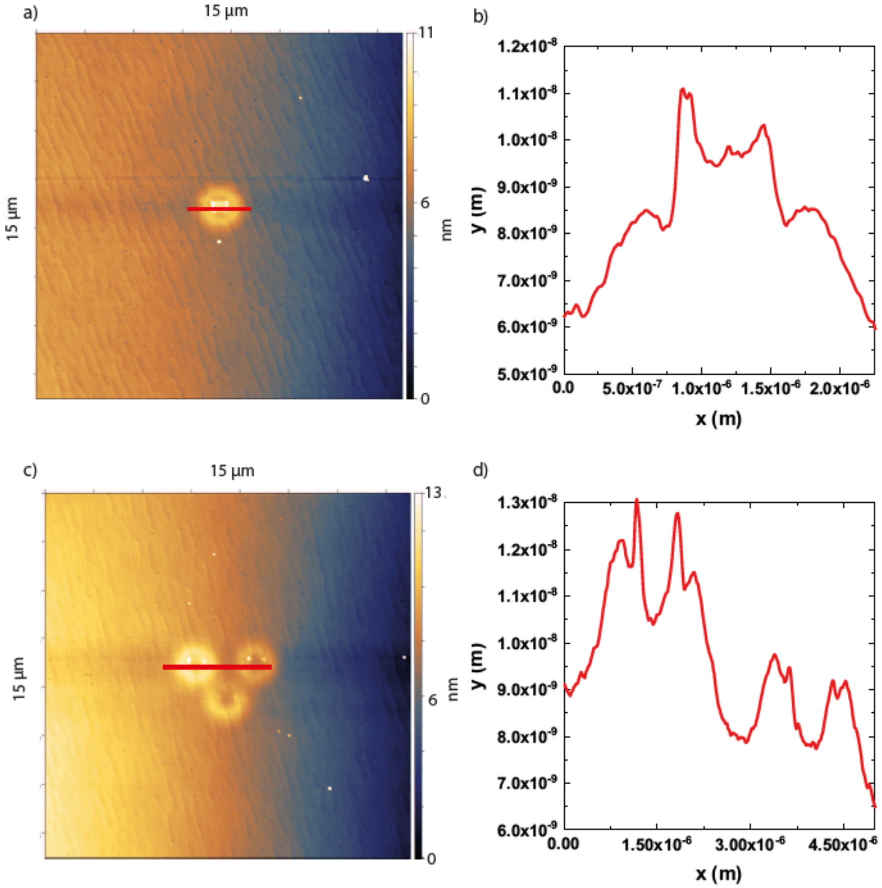

Figure 6.10: a) topography and b) line profile of a single carbon pad. c) Topography and d) line profile of three carbon pads in direct vicinity of each other.

Figure 6.11 e) shows the LRS and f) the LRS time stability of the devices with different carbon pad thicknesses and numbers and the reference. The reference device LRS is 10^7 Ω. The LRS of all other devices is independent of the number or thickness of the C pad around 5×10^5 Ω. The trend of a lower LRS by the addition of C to the top interface discussed in the previous chapter can thus be reproduced for patterned carbon. The low LRS time stability of the reference sample is in agreement with previous work from this group.[189]

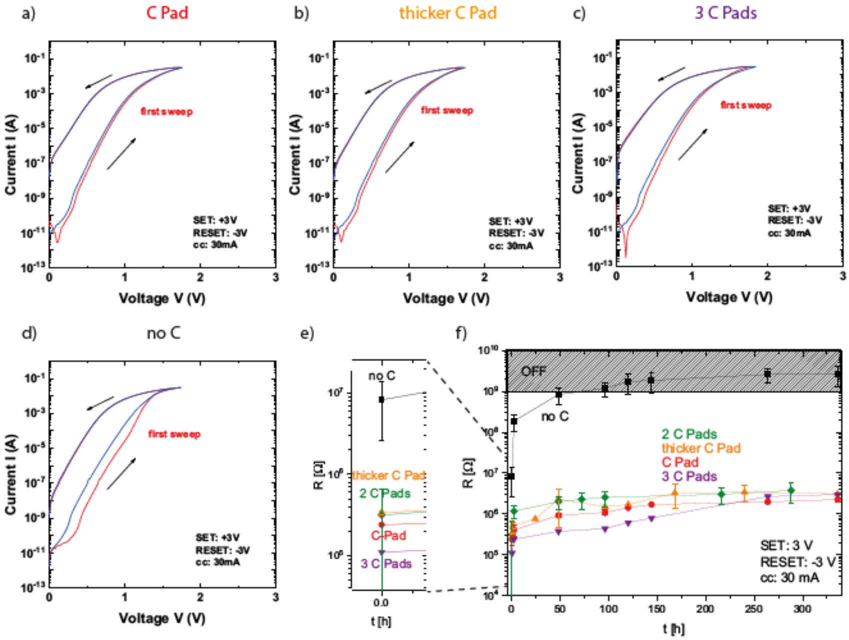

Figure 6.11: a) *I(V)*-characteristic of a stoichiometric $SrTiO_3$ device with a single carbon pad at the Pt interface, b) with a thicker C pad and c) with three carbon pads. d) *I(V)*-characteristic of a device without carbon pad on the same sample. e) LRS and f) LRS time stability of $SrTiO_3$ devices with different numbers and thicknesses of SEM deposited carbon pads.

Considering figure 6.11 it is mostly possible to reproduce the influence of C on the switching behavior of $SrTiO_3$, when using C patterns. Thus in a next step the influence of the C patterning on the variability is considered. Figure 6.12 shows the cycle to cycle (gray) and device to device (color) variability of devices with 0 pads (black), 1 pad (red), 2 pads (green) and 3 pads (violet). In comparison to the devices with areal carbon (figure 6.7), which had a markedly low cycle to cycle and device to device variability, both, cycle to cycle and device to device variability, are very high independent of pad number or even presence. Consequently their Weibull slopes are low ($0.85 \leq \beta \leq 1.36$), comparing to the one of areal carbon devices ($\beta = 3.14$).

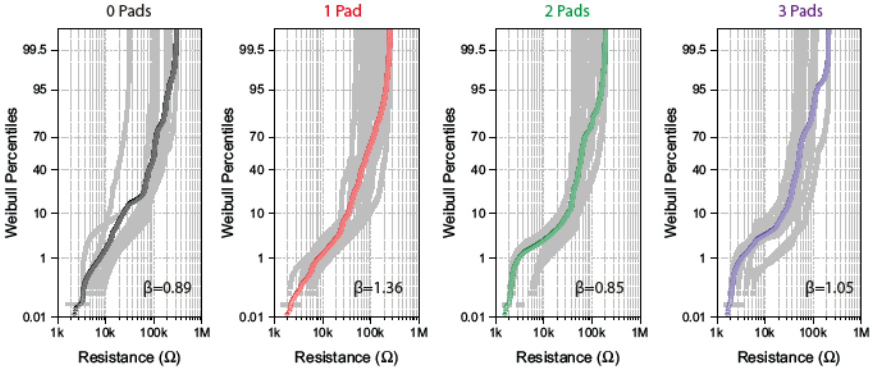

Figure 6.12: Cycle to cycle (gray) and device to device (color) variability of devices with 0 pads (black), 1 pad (red), 2 pads (green) and 3 pads (violet). The device to device variability results from averaging the cycle to cycle variabilities.

Discussion and conclusion: Carbon patterns

Within this section the possibilities of carbon patterns at the Pt/$SrTiO_3$ interface were investigated. SEM was identified as a practical method for the lithography of C pads of the desired height.

Different numbers of these pads and two different thicknesses were deposited and the resulting devices were subsequently investigated regarding their switching properties, which were then compared to a reference device, without any C pad. Expectedly devices with C patterns showed a lower LRS than the reference devices, which can be explained by the $SrCO_3$ heat confinement layer, as described in the previous section.

While this chapter aimed to pinpoint the filament and thus decrease the variability, devices with carbon pads showed the opposite effect. Their cycle to cycle variability increased. A possible explanation can be found in figure 6.13. Figure 6.13 a) shows exemplary the first 300 cycles of a device with three carbon pads, which underly the variability measurements. Figure 6.13 b) shows the topography of the device after forming and c) after 292 cycles, respectively. The topography reveals the recrystallization of Pt in certain areas. The recrystallization of Pt requires a temperature $\gtrsim$ 400 °C.[235] The recrystallized Pt can thus be used as an indicator for Joule

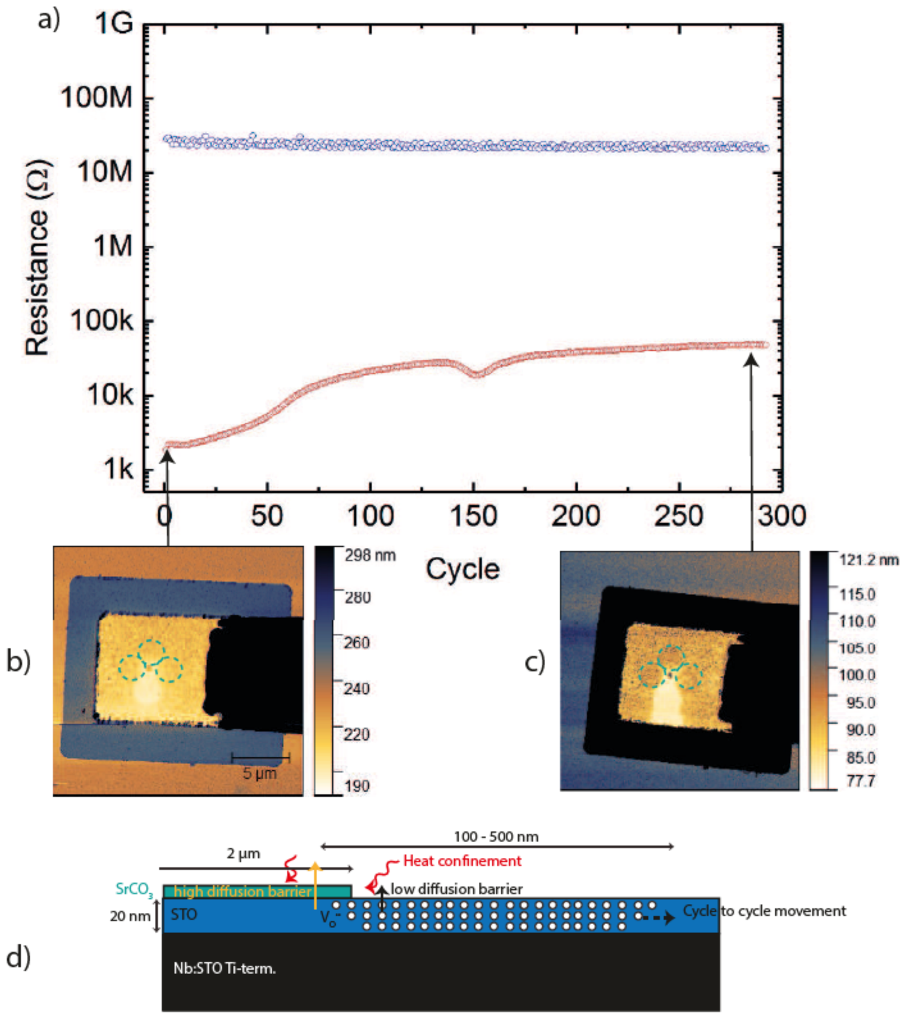

Figure 6.13: a) LRS resistance (red) and HRS resistance (blue) for 300 cycles with the recrystallization of Pt indicating the filament position illustrated by AFM topography measurements b) after forming and c) after 292 cycles, as a guide to the eye the position of the C pads is indicated by turquoise circles d) illustration of the proposed mechanism behind the change of the variability.

heating and filament position.

Figure 6.13 b) reveals that after the forming step basically two recrystallization circles are visible, one at the center of the carbon pads (center of the device) and one in contact with the first one, directly below it. A mechanism that could possibly explain this arrangement is, that the C pads confine heat, however their serial resistance makes it unlikely for the current to flow directly through the pads, instead the filament is formed in the vicinity of the pads, benefiting from the heat and the lower serial resistance. Figure 6.13 c) reveals an additional recrystallization circle after additional cycles. Considering figure 6.13 a) the appearance of the additional recrystallization circle is accompanied by a change of the LRS. The additional recrystallization circle implies that the position of the filament has drifted further away from the carbon pads to the bottom edge of the device. The fact that this drift is accompanied by a change of the LRS suggest that said drift is responsible for the high variability. The mechanism is depicted in figure 6.13 d).

The mechanism of heat confinement at the C pad resulting in a filament in the vicinity of the pad rather than underneath the pad can also explain the less pronounced forming step for devices with a carbon pad in comparison to to samples with similar areal C thickness. The forming step for areal C devices was explained by the high diffusion barrier for oxygen of $SrCO_3$, which has to be overcome. However the filament in case of C pads does not form underneath the $SrCO_3$, thus the diffusion barrier does not have to be overcome. In conclusion it is possible to initiate a certain filament position, but not to prevent its motion during repeated switching.

7 Conclusion and outlook

7.1 Origin and engineering of defects

7.1.1 The origin of oxygen vacancies and how to tailor them

In the course of chapter 4.1 different influences on the formation of oxygen vacancies during thermal annealing and pulsed laser deposition were investigated. These influences are summarized in figure 7.1. In case of thermal annealing, it can be assumed that $SrTiO_3$ is in thermal equilibrium. As discussed in chapter 2.1 the oxygen vacancy formation in the extrinsic regime can be described by equation 7.1.

$$\mathrm{O}_\mathrm{O}^x \rightleftharpoons \frac{1}{2}\mathrm{O}_2 + \mathrm{V}_\mathrm{O}^{\bullet\bullet} + 2\mathrm{e}^- \tag{7.1}$$

An obvious influence factor on this equilibrium is the oxygen pressure p_{Ox}, as it is a direct measure for the oxygen partaking in the reaction. In the course of this work it was found that, for physical annealing, the determination of the actual p_{Ox} is less trivial than expected. While commonly the p_{Ox} is determined by applying oxygen to a pumped system until reaching the desired pressure, it was found that the actual p_{Ox} is orders of magnitude lower. It was identified that the reason behind this are applied measurement devices that are based on ionization, e.g. the cold cathode pressure gauge. The cold cathode pressure gauge is schematically depicted on the left of figure 7.1. It was found that the cold cathode gauge shifts the CO/CO_2 towards CO. This in turn lowers the effective p_{Ox}, shifting equation 7.1 towards more reducing conditions.

It is also conceivable that the increased amount of CO increases the oxygen vacancy formation rate. The rate determining steps of oxygen vacancy formation are generally

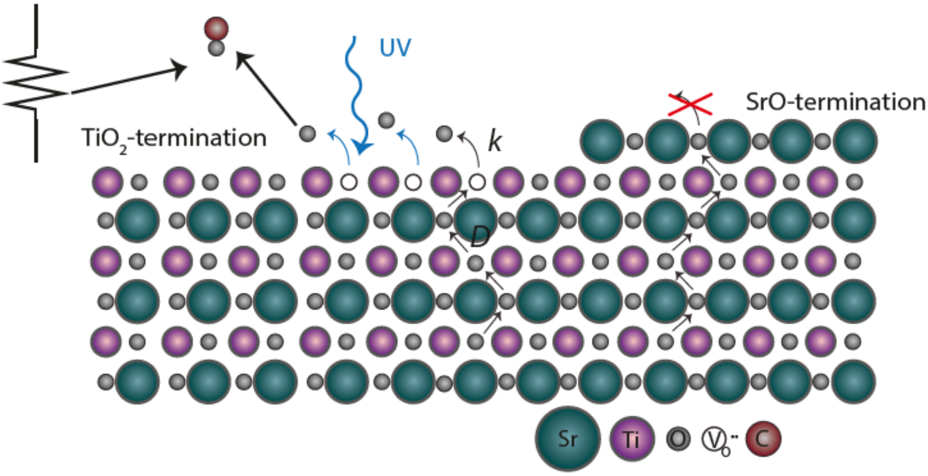

Figure 7.1: Schematic illustration of influences on the oxygen vacancy formation in $SrTiO_3$ unraveled in this work.

the oxygen vacancy diffusion D and the surface reaction rate k. In case of $SrTiO_3$ the oxygen vacancy diffusion can $\gtrsim 750$ K be estimated fast enough to consider the surface reaction as solely rate determining.[142] Further for all following considerations it will be presupposed that sufficient lattice oxygen is present.

Assuming that CO actively partakes in the oxygen vacancy defect equilibrium, it can be rearranged to equation 7.2.

$$O_O^x + CO \rightleftharpoons CO_2 + V_O^{\bullet\bullet} + 2e^- \tag{7.2}$$

Considering the formation enthalpies of O_2 (ΔH= 0 kJ/mol) and of CO reacting to CO_2 (ΔH=-171 kJ/mol) the enhanced oxygen vacancy incorporation is further based on the thermodynamical benefiting influence of CO on the rate limiting formation of oxygen from the lattice.

In the course of this work it was further found that the plasma plume during PLD emits UV radiation. This radiation in turn was found to influence the surface reaction rate. The underlying mechanism is based on the formation of electron hole pairs by the radiation and can thus be generalized for other radiation sources.

$$nil + hv \rightarrow \mathrm{e}^- + \mathrm{h}^\bullet \tag{7.3}$$

Equation 7.3 describes the formation of an electron hole pair by radiation.[56, 142–144]

$$\mathrm{O}_\mathrm{O}^x + 2\mathrm{h}^\bullet \rightleftharpoons \frac{1}{2}\mathrm{O}_2 + \mathrm{V}_\mathrm{O}^{\bullet\bullet} \tag{7.4}$$

Rearranging equation 7.1 into equation 7.4 it is apparent that the additional holes generated by the radiation enhance the oxygen vacancy incorporation.

Last the influence of the termination of $SrTiO_3$ was investigated. It was found in this work that the respective termination drastically influences the oxygen vacancy formation in the investigated pressure regime. Namely a SrO-termination fully depresses the oxygen vacancy incorporation. An explanation can be derived from the findings of Alexandrov *et al.*[164], who have shown by *ab initio* calculations that the formation energy of oxygen vacancies is lower for TiO_2-terminated $SrTiO_3$ as compared to SrO-terminated $SrTiO_3$. This in turn will influence the surface reaction. As the SrO coverage of $SrTiO_3$ can be controlled with high precision this allows a tunable oxygen vacancy formation, ranging from an inhibition of the oxygen vacancy formation to limiting their formation to certain areas of the surface.

Considering above results it was possible to further unravel the vast variety of influence factors on the oxygen vacancy formation in $SrTiO_3$. Two major influence factors, which are not linked to a change of the p_{Ox}, on the surface reaction of the formation of oxygen vacancies were presented, namely radiation and crystal termination. The latter one was utilized to tailor the formation of the oxygen vacancies. While the underlying mechanisms for both influence factors were largely uncovered, in future it would be interesting to quantify their influence on the surface reaction. Basically this is possible utilizing ^{18}O exchange and subsequently analyzing the ion profile with secondary ion mass spectrometry. However, this is non-trivial for the influence of the surface termination, as the SrO-termination was, in the course of this work, proven to be very unstable.

7.1.2 Cationic defect engineering

In chapter 4.2 the possibility of tailoring the stoichiometry of $SrTiO_3$ thin films by laser fluence control were fathomed. The underlying mechanisms of the fluence dependent stoichiometry are on the one hand the different effective evaporation enthalpies of SrO and TiO_2,[186] which result in a preferential ablation of SrO at low fluence and of TiO_2 at high fluence. On the other hand the much lighter Ti interacts stronger with the process gas than Sr, resulting in a Ti depletion for low energies. The Sr depletion at high fluence is, in the regimes considered in this work, accommodated by Sr-vacancies. Ti-vacancies are, as described in chapter 2.1, energetically unfavorable. Therefore the Ti-depletion for a low fluence is accommodated by the formation of Ruddlesden-Popper type anti phase boundaries and SrO islands on top of the film shown schematically in figure 7.2.

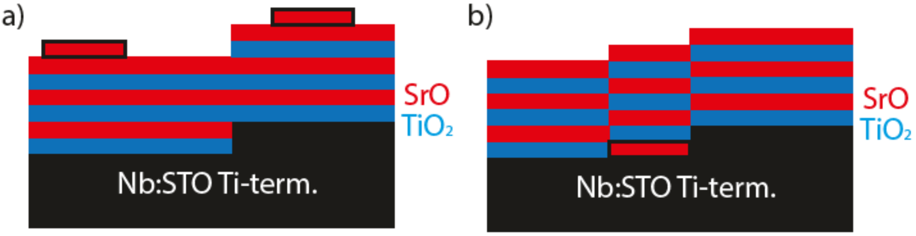

Figure 7.2: Schematic illustration of a) SrO islands and b) Ruddlesden-Popper type anti phase boundaries.

In the course of chapter 5.2 both accommodation mechanisms were engineered for stoichiometric thin films. In order to emulate SrO segregation on the surface, additional SrO exceeding 1.5 u.c. thickness is deposited on top of the stoichiometric thin film. Exceeding 1.5 u.c. thickness ensures the formation of islands, as the SrO no longer growth in a layer-by-layer fashion due to its high lattice mismatch in relation to $SrTiO_3$. Changing the thickness of the additional SrO, the thickness and morphology of the resulting islands can be influenced.

To engineer Ruddlesden-Popper type anti phase boundaries 1.5 u.c. SrO were deposited on the TiO_2-terminated 0.5 wt% Nb:$SrTiO_3$ substrate. As schematically shown in figure 7.2 b) the deposition of half a unit cell of SrO results in SrO islands on the now SrO-terminated 0.5 wt% Nb:$SrTiO_3$ substrate. These islands result in

SrO double layers during $SrTiO_3$ growth and can be regarded as Ruddlesden-Popper type anti phase boundaries parallel to the growth direction. Moreover, subsequently depositing stoichiometric $SrTiO_3$ will result in Ruddlesden-Popper type anti phase boundaries induces at the edges of the SrO islands as shown in figure 7.2 b). However, using regular 0.5 wt% Nb:$SrTiO_3$ substrates the SrO islands will rather migrate to the surface of the film, as it is energetically preferable.[61] It was shown that this effect can be avoided by using substrates with a higher miscut. A higher miscut results in a higher density of step edges. The SrO stabilizes at the step edges, compare figure 7.2 b), eventually resulting in the desired seeds for the formation of Ruddlesden-Popper type anti phase boundaries.

7.2 Impact of defects on the switching performance

In the following the results of this work on the influences on resistive switching presented in chapters 5 and 6 will be presented categorized by properties. One motivation of this work was to understand the enhanced performance of devices with Sr-rich $SrTiO_3$ in comparison to stoichiometric $SrTiO_3$ devices and, thus, eventually to be able to derive design rules from this understanding. It was found that one of the most important influence factors is additional $SrCO_3$ at the Pt/$SrTiO_3$ interface. For Sr-rich devices more $SrCO_3$ forms at the Pt/$SrTiO_3$ interface than for stoichiometric devices due to the increased availability of SrO. This amount can be increased even further, when depositing additional SrO at the Pt/$SrTiO_3$ interface, as described above. If the Pt is applied *in situ* the formation of $SrCO_3$ can be depressed. Depositing C *in situ* allows to some extend controlling the amount of $SrCO_3$ forming at the Pt/$SrTiO_3$ interface.

Forming step

The forming step is characterized by a higher voltage necessary to observe an increase in current for the first SET than for all subsequent SETs. As the low resistive state is characterized by the formation of a conductive oxygen vacancy rich filament, the limiting factors of eq. 7.1 can either be the diffusion of the oxygen vacancies or their generation. All subsequent SETs and RESETs were shown to only change the oxygen vacancy concentration by a factor of 2-3.[188] Thus the difference between the virgin state and the formed state can be explained by the necessity to generate additional oxygen vacancies during the first SET. The limitation of this process by either diffusion or generation results in a pronounced forming step. From a viewpoint of industrial application a forming step is highly undesirable.[194]

In the course of this work a possible mechanism underlying the device structure dependent forming step was introduced. Additionally devices were engineered that show no forming step. In the course of this work it was found that the forming step roughly scales with the amount of $SrCO_3$ at the Pt/$SrTiO_3$ interface. $SrCO_3$ has a high diffusion barrier for oxygen,[223] it is thus conceivable that with an increasing thickness of this diffusion barrier an increasing voltage is necessary to enable oxygen diffusion through this barrier and thus enable the formation of oxygen vacancies in $SrTiO_3$. This is schematically illustrated in figure 7.3 a). While this mechanism best explains the results presented in this work, it also fails to some extend. Our results suggest $SrCO_3$ islands much smaller than the filament diameter (100-500 nm),[174, 188, 201] provoking the question, why the diffusion barrier would have to be overcome, if it could just be bypassed, as shown in figure 7.3 a). A possible reason could be the additional heat induced by the $SrCO_3$ discussed below. In future this contradiction should be unraveled or a more suitable explanation should be found e.g. by additional spectromicroscopic investigations of the forming step in the vicinity of the islands or by simulating the field and temperature distribution and comparing it to the here presented experimental data.

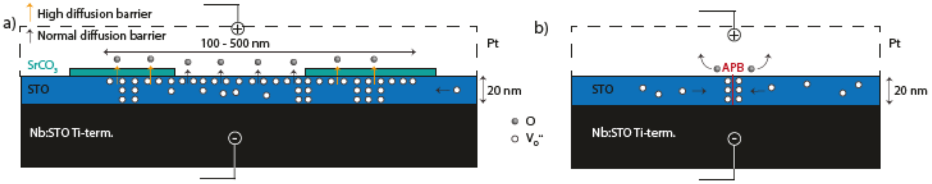

Figure 7.3: Schematic illustration of a) the proposed mechanism underlying a pronounced forming step and b) Ruddlesden-Popper type anti phase boundaries acting as preformed filaments.

Within this work $SrTiO_3$ devices that require no forming step were fabricated by intentionally introducing Ruddlesden-Popper type anti phase boundaries (compare section 7.1.2). A possible explanation is that Ruddlesden-Popper type anti phase boundaries act as preformed filaments, as depicted in 7.3 b). It is conceivable that oxygen vacancies have a lower formation energy in the vicinity of Ruddlesden-Popper type anti phase boundaries, as they have for other extended defects, as small angular grain boundaries and dislocations.[7, 197, 199, 236] This in turn would result in an oxygen vacancy enrichment along Ruddlesden-Popper type anti phase boundaries, defining them as preformed filaments. To prove this explanation a conceivable next step would be to actually determine the formation energy of oxygen vacancies at the Ruddlesden-Popper type anti phase boundaries.

ON/OFF ratio

The ON/OFF ratio describes the difference between LRS and HRS measured immediately after SET and RESET, respectively. Only one device structure showed a markedly different HRS than all other devices, namely devices including Sr-rich $SrTiO_3$. This was explained by the cation vacancies induced by the Sr-rich growth,[106] which are deep acceptors trapping electrons and consequently increase the resistance of the bulk $SrTiO_3$. [48] For all other devices the ON/OFF ratio is consequently defined by the LRS.

In the course of chapter 6.1 it was uncovered that the LRS is mainly defined by the Joule heating present during SET, as the Joule heating increases the formation of oxygen vacancies. In particular it was found that the heat needs to be confined at the interface to induce sufficient heat to activate the formation of oxygen vacancies at the $Pt/SrTiO_3$ interface. It was found that $SrCO_3$ acts as a heat confinement layer and that by increasing the amount of $SrCO_3$ it is possible to decrease the LRS until a certain saturation value is reached. Samples completely lacking $SrCO_3$ at the $Pt/SrTiO_3$ interface were even found to show no switching at all.

Currently the suggested heat confinement mechanism best described the experimental observations of this work. In future it would be desirable to confirm this mechanism by simulations of the heat confinement. Further the next logical step would be to apply a heat confinement layer with an even lower thermal conductivity than $SrCO_3$.

A possible candidate is WO_2 as it has a low thermal conductivity[237] and is a metallic conductor ($\rho(300\ \mathrm{K}) = 2.9 \times 10^{-3}$)[238].

LRS retention time

One of the major failure mechanisms of resistive switching $SrTiO_3$ is a reoxidization of the oxygen vacancy rich filament at the Pt/$SrTiO_3$ interface over time resulting in an approach of the LRS towards the HRS.[187, 188] In the course of this work a possibility to stabilize the LRS was developed. The introduction of a oxygen diffusion blocking layer at the Pt/$SrTiO_3$ interface stops a reoxidization of the filament over time. One possibility to achieve a diffusion blocking layer is the deposition of SrO at the Pt/$SrTiO_3$ interface. If more than 1.5 u.c. SrO are deposited the formation of islands is observable, as is also observable for Sr-rich growth. The resulting islands would supposedly be SrO in the rock salt structure exhibiting the desired diffusion blocking property.[174] It was found that increasing the thickness of these islands did in the investigated regime further increase the stability of the LRS. Although the area of these islands is smaller than the filament area as depicted in 7.4 it is, considering the filament dimensions, still conceivable that they stabilize the LRS *via* the proposed mechanism. Moreover, a reoxidization of the uncovered filament area can explain the initial increase of the LRS that is usually observed.

While at the beginning of this work SrO was proposed as the retention stabilization layer, the results obtained in the further course of this work suggest that the SrO forms $SrCO_3$. However, as $SrCO_3$ has a high oxygen diffusion barrier as well,[223] the proposed mechanism is equally valid.

Variability

While traditionally the development of memories aimed for a very low variability, [239] the emerging field of neuromorphic computing is also interested in employing it for stochastic learning algorithms.[229–233] Prior to this work the variability of $SrTiO_3$ devices has scarcely been investigated. Recent advances of this group have suggested that the high variability of $SrTiO_3$ devices is caused by a change of the filament position or physiognomy between cycles.[201] Within this work the

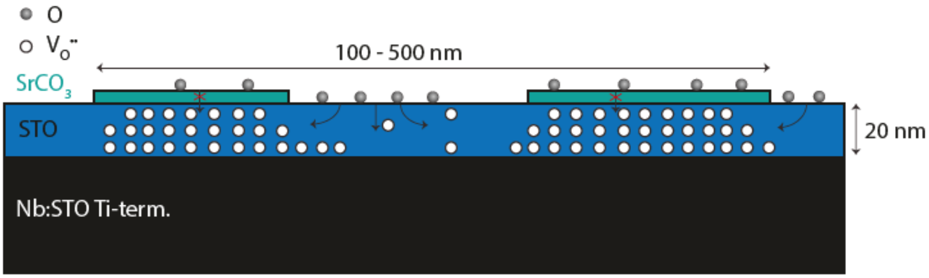

Figure 7.4: Illustration of the underlying mechanism of the LRS stabilization by $SrCO_3$ islands.

proposed mechanism was further investigated with respect to different influences. In agreement with the prior work it was possible to account for changes in the LRS by a change of the filament position. It was possible to visualize the change of the filament position by investigating the recrystallization of the Pt top electrode.

The stoichiometry of the $SrTiO_3$ thin film showed no significant influence on the variability. Thus, following the relatively high cycle to cycle and device to device variability presented for stoichiometric and Sr-rich devices in chapter 5.1 is considered as reference. Below a possible underlying mechanism for devices that showed marked deviations from the references will be discussed. Devices with additional 3 u.c. of SrO, that were shown to form $SrCO_3$, at the Pt/$SrTiO_3$ interface showed, as presented in chapter 5.2, a low cycle to cycle variability, but a high device to device variability. Devices with areal C deposition, resulting in a thin areal $SrCO_3$ layer, showed a low cycle to cycle and device to device variability, as presented in chapter 6.1. Devices with a C pattern at the Pt/$SrTiO_3$ interface showed an increased cycle to cycle variability, as presented in chapter 6.2.

The proposed underlying mechanism for the variability of the three different considered devices is illustrated in figure 7.5. The mechanism assumes a filament diameter of 100-500 nm as observed previously by this group.[174, 188, 201] Further it presupposes the existence of preferred filament positions within the $SrTiO_3$ film. As described in figure 7.3, one possibility for such a position are anti phase boundaries.

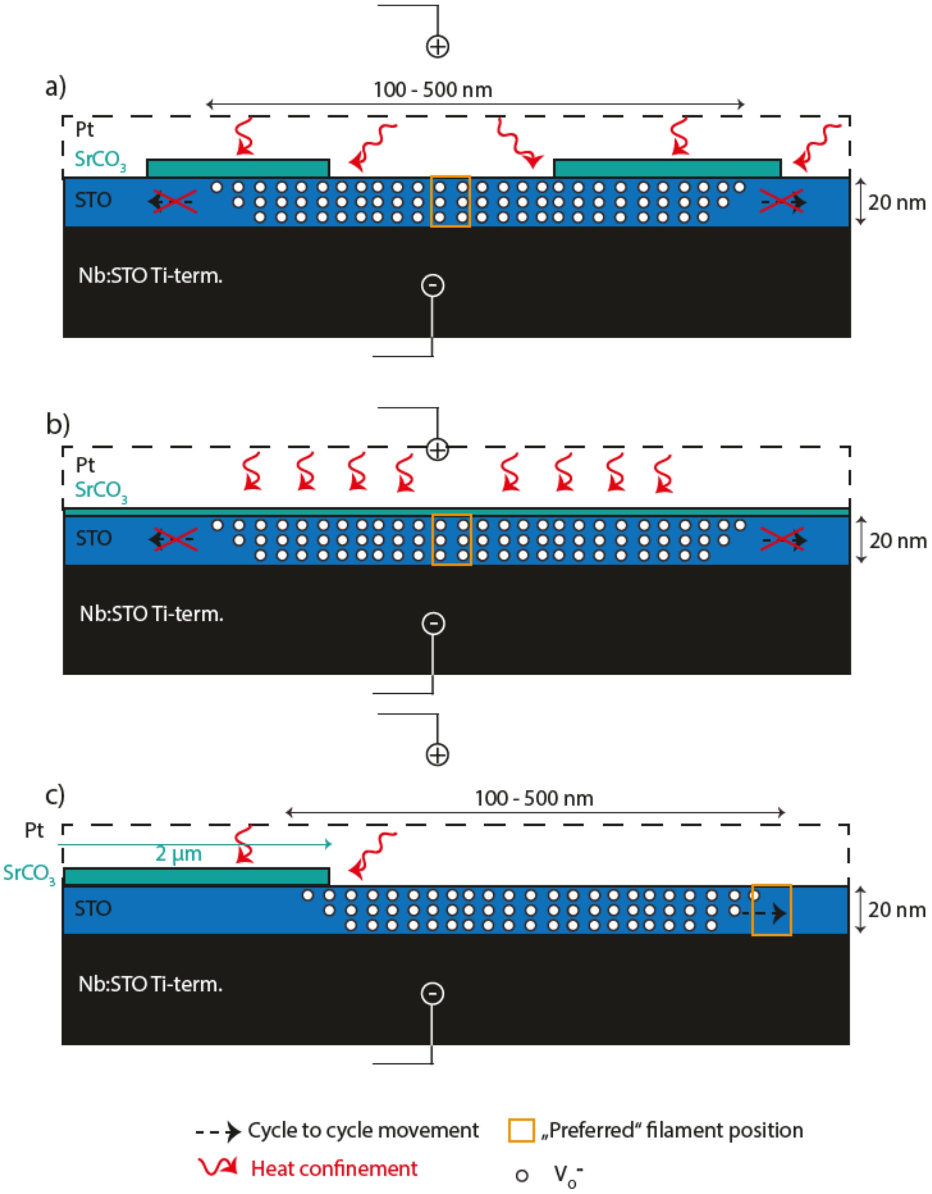

Figure 7.5: Proposed underlying mechanism of the variability observed for devices with a) $SrCO_3$ islands, b) areal $SrCO_3$ and c) $SrCO_3$ pads.

Figure 7.5 a) shows the proposed mechanism for devices with additional 3 u.c. of SrO deposited at the Pt/$SrTiO_3$ interface. The resulting SrO islands form $SrCO_3$, which confine the heat during switching. The $SrCO_3$ islands are randomly distributed at the Pt/$SrTiO_3$ interface and considerably smaller than the filament. Upon appliance of the voltage the filament will form, where a preferred filament position is best aligned with the heat confining islands. The result will be a filament that is pinpointed and will likely not change for subsequent SETs and RESETs, explaining the low cycle to cycle variability. However, the alignment of preferred filament position and heat confining islands can differ from device to device, in turn explaining the high device to device variability.

Figure 7.5 b) shows the proposed mechanism for devices with areal C at the Pt/$SrTiO_3$ interface, which probably forms a thin $SrCO_3$ layer. In comparison to device with $SrCO_3$ islands the heat is confined evenly over the whole device area for each device. Consequently the filament will form at its preferred position for each device and not change position afterwards. This results in a low cycle to cycle and device to device variability.

Figure 7.5 c) shows the proposed mechanism for devices with a carbon pattern applied to the Pt/$SrTiO_3$ interface. In comparison to the $SrCO_3$ in figure 7.5 a) the $SrCO_3$ 'islands' resulting from the appliance of a C pad have a diameter of $\approx 2\ \mu$m and are thus significantly bigger than the filament. This comparably big structure will confine the heat, when a voltage is applied. However the filament will only form in its vicinity. Opposed to the $SrCO_3$ islands in figure 7.5 a), which are smaller than the filament and thus allow the formation of the filament underneath, the oxygen vacancies will form at the edge of the big $SrCO_3$ island, where they do not have to overcome an additional diffusion barrier, but still profit from the induced heat. It is unlikely that this edge is also a preferred filament position. Thus, for the subsequent cycles, the filament will move towards its preferred position, where it stabilizes. This is in good agreement with the observations in chapter 6.2 that the high variability of the LRS occurs during the first 200 cycles. Afterwards position and LRS are stable, which would, in the proposed mechanism, be explained by the stabilization of the filament at its preferred position.

In future further investigations should be conducted to verify the proposed mechanisms. One possibility is to investigate the Joule heating by heat sensible microscopy. More importantly it is necessary to prove the existence of preferred filament positions.

List of abbreviations

AFM	Atomic force microscopy
APB	Anti-phase boundary
c8w	counter-eightwise
CC	Cold cathode gauge
cc	Current compliance
DC	Direct current
DFT	density functional theory
FWHM	Full width half maximum
HAADF	High angular annual dark field
HRS	High resistance state
IR	Infrared
LCAFM	Local conductivity atomic force microscopy
LRS	Low resistance state
MIM	Metal-insulator-metal
MS	Mass spectrometer
PCM	Phase change memory
PEEM	Photoemission electron microscopy
PLD	Pulsed laser deposition
RT	Room temperature
RF	Radio frequency
RHEED	Refelctive high energy electron diffraction
SKPFM	Cross sectional scanning Kelvin probe microscopy
STM	Scanning tunneling microscopy
TEM	Transmission electron microscopy
UHV	Ultra-high vacuum
UV	Ultraviolett

VCM	Valence change mechanism
VEPALS	Variable energy positron annihilation lifetime spectroscopy
XPS	X-ray photon spectroscopy
XRD	X-ray diffraction
2DEG	Two dimensional electron gas
8w	eightwise

Bibliography

[1] **C. Rao**, *Annual Review of Physical Chemistry* **40**, 291 (1989). 1

[2] **H. M. Christen** and **G. Eres**, *Journal of Physics: Condensed Matter* **20**, 264005 (2008). 1

[3] **D. H. Lowndes**, **D. B. Geohegan**, **A. A. Puretzky**, **D. P. Norton**, and **C. M. Rouleau**, *Science* **273**, 898 (1996). 20

[4] **P. R. Willmott** and **J. R. Huber**, *Reviews of Modern Physics* **72**, 315 (2000). 1, 47

[5] **R. Moos**, **W. Menesklou**, and **K. H. Hardtl**, *Applied Physics a-Materials Science & Processing* **61**, 389 (1995). 1, 2, 3, 6, 7, 34, 35, 38, 39, 40, 41, 54

[6] **R. Moos** and **K. H. Hardtl**, *Journal of the American Ceramic Society* **80**, 2549 (1997). 2, 6, 7, 35, 39, 40, 54

[7] **R. A. De Souza**, **V. Metlenko**, **D. Park**, and **T. E. Weirich**, *Physical Review B - Condensed Matter and Materials Physics* **85**, 1 (2012). 3, 6, 7, 34, 36, 40, 44, 51, 54, 56, 92, 93, 133

[8] **F. Gunkel**, **S. Hoffmann-Eifert**, **R. Dittmann**, **S. B. Mi**, **C. L. Jia**, **P. Meuffels**, and **R. Waser**, *Applied Physics Letters* **97**, 2 (2010). 1, 2, 34

[9] **Y. Kozuka**, **Y. Hikita**, **C. Bell**, and **H. Y. Hwang**, *Applied Physics Letters* **97**, 11 (2010). 1

[10] **T. Ohnishi**, **K. Shibuya**, **T. Yamamoto**, and **M. Lippmaa**, *Journal of Applied Physics* **103**, 0 (2008). 8, 75

[11] **J. Son**, **P. Moetakef**, **B. Jalan**, **O. Bierwagen**, **N. J. Wright**, **R. Engel-Herbert**, and **S. Stemmer**, *Nature materials* **9**, 482 (2010).

[12] **D. J. Keeble**, **B. Jalan**, **L. Ravelli**, **W. Egger**, **G. Kanda**, and **S. Stemmer**, *Applied Physics Letters* **99**, 97 (2011).

[13] **M. Andrä**, **F. DvoÅ™ák**, **M. Vorokhta**, **S. Nemšák**, **V. Matolín**, **C. M. Schneider**, **R. Dittmann**, **F. Gunkel**, **D. N. Mueller**, and **R. Waser**, *APL Materials* **5**, 056106 (2017).

[14] **F. Gunkel**, **P. Brinks**, **S. Hoffmann-Eifert**, **R. Dittmann**, **M. Huijben**, **J. E. Kleibeuker**, **G. Koster**, **G. Rijnders**, and **R. Waser**, *Applied Physics Letters* **100**, 3 (2012).

[15] **F. Gunkel**, **R. Waser**, **A. H. Ramadan**, **R. A. De Souza**, **S. Hoffmann-Eifert**, and **R. Dittmann**, *Physical Review B* **93**, 1 (2016).

[16] **R. Meyer**, **A. F. Zurhelle**, **R. A. De Souza**, **R. Waser**, and **F. Gunkel**, *Physical Review B* **94** (2016). 1

[17] **R. Dittmann**, Stoichiometry in epitaxial oxide thin films, in *Epitaxial growth of complex oxides*, chapter 9, pp. 231–260, Elsevier, Cambridge, 2015. 1, 20, 22, 55, 68, 75

[18] **E. Breckenfeld**, **N. Bronn**, **J. Karthik**, **A. R. Damodaran**, **S. Lee**, **N. Mason**, and **L. W. Martin**, *Physical Review Letters* **110**, 1 (2013). 1, 13, 56, 62, 63, 66

[19] **G. Herranz**, **M. Basletic**, **M. Bibes**, **R. Ranchal**, **A. Hamzic**, **E. Tafra**, **K. Bouzehouane**, **E. Jacquet**, **J. P. Contour**, **A. Barthélémy**, and **A. Fert**, *Physical Review B - Condensed Matter and Materials Physics* **73**, 216803 (2006).

[20] **C. Xu**, **H. Du**, **A. J. Van Der Torren**, **J. Aarts**, **C. L. Jia**, and **R. Dittmann**, *Scientific Reports* **6**, 1 (2016). 1, 8, 11, 74, 76

[21] **R. Moos** and **K. H. Haerdtl**, *Journal of Applied Physics* **80**, 393 (1996). 2, 35

[22] **A. Kalabukhov**, **R. Gunnarsson**, **J. Boerjesson**, **E. Olsson**, **T. Claeson**, and **D. Winkler**, *Physical Review B - Condensed Matter and Materials Physics* **75**, 2 (2007). 2, 13, 34, 35, 45, 50, 56, 62, 63

[23] **H. P. R. Frederikse**, **W. R. Thurber**, and **W. R. Hosler**, *Physical Review* **134**, 2 (1964). 36, 57, 64

[24] **H. Y. Peng**, **L. Pu**, **J. C. Wu**, **D. Cha**, **J. H. Hong**, **W. N. Lin**, **Y. Y. Li**, **J. F. Ding**, **A. David**, **K. Li**, and **T. Wu**, *APL Materials* **1**, 052106 (2013). 2, 35, 50

[25] **A. Ohtomo** and **H. Y. Hwang**, *Nature* **427**, 423 (2004). 2, 12, 13, 56, 62, 63, 66

[26] **C. Woltmann**, **T. Harada**, **H. Boschker**, **V. Srot**, **P. A. Van Aken**, **H. Klauk**, and **J. Mannhart**, *Physical Review Applied* **4**, 1 (2015). 2

[27] **S. Goswami**, **E. Mulazimoglu**, **L. M. Vandersypen**, and **A. D. Caviglia**, *Nano Letters* **15**, 2627 (2015).

[28] **Q. Liu**, **L. Dong**, **Y. Liu**, **R. Gordon**, **P. D. Ye**, **P. Fay**, and **A. Seabaugh**, *Solid-State Electronics* **76**, 1 (2012).

[29] **M. Hosoda**, **Y. Hikita**, **H. Y. Hwang**, and **C. Bell**, *Applied Physics Letters* **103**, 4 (2013).

[30] **P. D. Eerkes**, **W. G. Van Der Wiel**, and **H. Hilgenkamp**, *Applied Physics Letters* **103**, 2 (2013).

[31] **W. Liu**, **S. Gariglio**, **A. Fête**, **D. Li**, **M. Boselli**, **D. Stornaiuolo**, and **J.-M. Triscone**, *APL Materials* **3**, 062805 (2015).

[32] **S. Hurand**, **A. Jouan**, **C. Feuillet-Palma**, **G. Singh**, **J. Biscaras**, **E. Lesne**, **N. Reyren**, **A. Barthélémy**, **M. Bibes**, **J. E. Villegas**, **C. Ulysse**, **X. Lafosse**, **M. Pannetier-Lecoeur**, **S. Caprara**, **M. Grilli**, **J. Lesueur**, and **N. Bergeal**, *Scientific Reports* **5**, 1 (2015).

[33] **L. Bjaalie**, **B. Himmetoglu**, **L. Weston**, **A. Janotti**, and **C. G. Van De Walle**, *New Journal of Physics* **16** (2014). 2

[34] **N. Nakagawa**, **H. Y. Hwang**, and **D. A. Muller**, *Nature Materials* **5**, 204 (2006). 2, 12, 56

[35] **C. Xu**, **C. Bäumer**, **R. A. Heinen**, **S. Hoffmann-Eifert**, **F. Gunkel**, and **R. Dittmann**, *Scientific Reports* **6**, 22410 (2016). 2, 13, 34, 35, 44, 45, 49, 50, 62, 63

[36] **R. Waser** and **M. Aono**, *Nature Materials* **6**, 833 (2007). 2

[37] **A. Sawa**, *Materials Today* **11**, 28 (2008).

[38] **R. Waser**, **R. Dittmann**, **C. Staikov**, and **K. Szot**, *Advanced Materials* **21**, 2632 (2009).

[39] **J. J. Yang**, **M. D. Pickett**, **X. Li**, **D. A. A. Ohlberg**, **D. R. Stewart**, and **R. S. Williams**, *Nature Nanotechnology* **3**, 429 (2008).

[40] **H.-S. P. Wong**, **H.-Y. Lee**, **S. Yu**, **Y.-S. Chen**, **Y. Wu**, **P.-S. Chen**, **B. Lee**, **F. T. Chen**, and **M.-j. Tsai**, *Proceedings of the IEEE* **100**, 1951 (2012).

[41] **E. Linn**, **R. Rosezin**, **C. Kügeler**, and **R. Waser**, *Nature materials* **9**, 403 (2010). 2

[42] **D. S. Jeong**, **R. Thomas**, **R. S. Katiyar**, **J. F. Scott**, **H. Kohlstedt**, **A. Petraru**, and **C. S. Hwang**, *Reports on Progress in Physics* **75**, 076502 (2012). 2

[43] **H. W. Huang**, **C. F. Kang**, **F. I. Lai**, **H. He**, **S. J. Lin**, and **Y. L. Chueh**, *Nanoscale Research Letters* **8**, 1 (2013).

[44] **K. M. Kim**, **D. S. Jeong**, and **C. S. Hwang**, *Nanotechnology* **22** (2011).

[45] **C. Park**, **S. H. Jeon**, **S. C. Chae**, **S. Han**, **B. H. Park**, **S. Seo**, and **D. W. Kim**, *Applied Physics Letters* **93**, 10 (2008).

[46] **B. J. Choi**, **D. S. Jeong**, **S. K. Kim**, **C. Rohde**, **S. Choi**, **J. H. Oh**, **H. J. Kim**, **C. S. Hwang**, **K. Szot**, **R. Waser**, **B. Reichenberg**, and **S. Tiedke**, *Journal of Applied Physics* **98** (2005).

[47] **K. Shibuya**, **R. Dittmann**, **S. Mi**, and **R. Waser**, *Advanced Materials* **22**, 411 (2010). 2

[48] **N. Raab**, **C. Bäumer**, and **R. Dittmann**, *AIP Advances* **5**, 047150 (2015). 3, 77, 78, 80, 84, 99, 101, 133

[49] **S. Piskunov**, **E. Heifets**, **R. I. Eglitis**, and **G. Borstel**, *Computational Materials Science* **29**, 165 (2004). 5, 94, 100

[50] **M. Adachi**, **Y. Akishige**, **T. Asahi**, **K. Deguchi**, **K. Gesi**, **K. Hasebe**, **T. Hikita**, **T. Ikeda**, **Y. Iwata**, **M. Komukae**, **T. Mitsui**, **E. Nakamura**, **N. Nakatani**, **M. Okuyama**, **T. Osaka**, **A. Sakai**, **E. Sawaguchi**, **Y. Shiozaki**, **T. Takenaka**, **K. Toyoda**, **T. Tsukamoto**, and **T. Yagi**, SrTiO3 Survey, 1A-8, in *Oxides*, edited by **Y. Shiozaki**, **E. Nakamura**, and **T. Mitsui**, pp. 1–7, Springer-Verlag, Berlin/Heidelberg. 5

[51] **M. Kawasaki**, **K. Takahashi**, **T. Maeda**, **R. Tsuchiya**, **M. Shinohara**, **O. Ishiyama**, **T. Yonezawa**, **M. Yoshimoto**, and **H. Koinuma**, *Science* **266**, 1540 (1994). 5, 17, 71

[52] **M. Kawai**, **Z. Y. Liu**, **T. Hanada**, **M. Katayama**, **M. Aono**, and **C. F. McConville**, *Applied Surface Science* **82-83**, 487 (1994). 5

[53] **G. Gottstein**, Kristallbaufehler, in *Materialwissenschaften und Werkstofftechnik*, pp. 71–114, Springer Vieweg, Berlin/Heidelberg, 2014. 5, 10, 11

[54] **F. A. Kröger** and **H. J. Vink**, *Solid State Physics* **3**, 310 (1956). 6, 39, 54

[55] **F. Gunkel**, *The role of defects at functional interfaces between polar and non-polar perovskite oxides*, PhD thesis, RWTH Aachen University, 2013. 6, 7, 8, 9

[56] **R. Merkle** and **J. Maier**, *Angewandte Chemie - International Edition* **47**, 3874 (2008). 7, 43, 47, 55, 64, 115, 129

[57] **S. Mochizuki**, **F. Fujishiro**, and **S. Minami**, *Journal of Physics-Condensed Matter* **17**, 923 (2005). 7, 47

[58] **M. C. Tarun**, **F. A. Selim**, and **M. D. McCluskey**, *Physical Review Letters* **111**, 1 (2013). 7, 47, 55

[59] **F. Gunkel**, **S. Hoffmann-Eifert**, **R. Dittmann**, **S. B. Mi**, **C. L. Jia**, **P. Meuffels**, and **R. Waser**, *Applied Physics Letters* **97**, 012103 (2010). 7, 35, 39, 40, 41, 42, 54

[60] **T. Tanaka**, **K. Matsunaga**, **Y. Ikuhara**, and **T. Yamamoto**, *Physical Review B* **68**, 205213 (2003). 8, 75

[61] **Y. F. Nie**, **Y. Zhu**, **C.-H. Lee**, **L. F. Kourkoutis**, **J. a. Mundy**, **J. Junquera**, **P. Ghosez**, **D. J. Baek**, **S. Sung**, **X. X. Xi**, **K. M. Shen**, **D. a. Muller**, and **D. G. Schlom**, *Nature communications* **5**, 4530 (2014). 8, 11, 71, 74, 86, 94, 131

[62] **T. Ohnishi**, **M. Lippmaa**, **T. Yamamoto**, **S. Meguro**, and **H. Koinuma**, *Applied Physics Letters* **87**, 1 (2005). 8, 75

[63] **L. Morresi**, Basics of molecular beam epitaxy (MBE), in *Silicon Based Thin Film Solar Cells*, number January 2013, pp. 81–107, 2013. 9

[64] **A. E. Paladino**, **L. G. Rubin**, and **J. S. Waugh**, *Journal of Physics and Chemistry of Solids* **26**, 391 (1965). 10

[65] **K. Szot**, **W. Speier**, **R. Carius**, **U. Zastrow**, and **W. Beyer**, *Physical Review Letters* **88**, 4 (2002). 10

[66] **F. V. E. Hensling**, *Influence of the Substrate Temperature during Pulsed Laser Deposition on the Switching Characteristics of SrTiO3*, Project thesis, RWTH Aachen University, 2015. 10, 87

[67] **C. Lenser**, *Investigation of Resistive Switching in Fe-doped SrTiO3 by Advanced Spectroscopy*, phd thesis, RWTH Aachen, 2013. 10

[68] **R. Wang**, **Y. Zhu**, and **S. M. Shapiro**, *Physical Review Letters* **80**, 2370 (1998). 10

[69] **J. H. Lee**, **G. Luo**, **I. C. Tung**, **S. H. Chang**, **Z. Luo**, **M. Malshe**, **M. Gadre**, **A. Bhattacharya**, **S. M. Nakhmanson**, **J. A. Eastman**, **H. Hong**, **J. Jellinek**, **D. Morgan**, **D. D. Fong**, and **J. W. Freeland**, *Nature Materials* **13**, 879 (2014). 11

[70] **J. Robertson**, *Journal of Vacuum Science & Technology B: Microelectronics and Nanometer Structures* **18**, 1785 (2000). 11

[71] **F. M. F. de Groot**, **M. Grioni**, **J. C. Fuggle**, **J. Ghijsen**, **G. A. Sawatzky**, and **H. Petersen**, *Physical Review B* **40**, 5715 (1989). 11

[72] **P. Blennow**, **A. Hagen**, **K. Hansen**, **L. Wallenberg**, and **M. Mogensen**, *Solid State Ionics* **179**, 2047 (2008). 12

[73] **X. Guo**, **X. Chen**, **Y. Sun**, **L. Sun**, **X. Zhou**, and **W. Lu**, *Physics Letters A* **317**, 501 (2003). 12

[74] **S.-G. Lim**, **S. Kriventsov**, **T. N. Jackson**, **J. H. Haeni**, **D. G. Schlom**, **A. M. Balbashov**, **R. Uecker**, **P. Reiche**, **J. L. Freeouf**, and **G. Lucovsky**, *Journal of Applied Physics* **91**, 4500 (2002). 12

[75] **H. Lehnert**, **H. Boysen**, **P. Dreier**, and **Y. Yu**, *Zeitschrift für Kristallographie - Crystalline Materials* **215** (2000). 12

[76] **M. Huijben**, **A. Brinkman**, **G. Koster**, **G. Rijnders**, **H. Hilgenkamp**, and **D. H. A. Blank**, *Advanced Materials* **21**, 1665 (2009). 12, 13, 56, 62, 63

[77] **H. Lee**, **N. Campbell**, **J. Lee**, **T. J. Asel**, **T. R. Paudel**, **H. Zhou**, **J. W. Lee**, **B. Noesges**, **J. Seo**, **B. Park**, **L. J. Brillson**, **S. H. Oh**, **E. Y. Tsymbal**, **M. S. Rzchowski**, and **C. B. Eom**, *Nature Materials* **17**, 231 (2018). 12

[78] **J. Nishimura**, **A. Ohtomo**, **A. Ohkubo**, **Y. Murakami**, and **M. Kawasaki**, *Japanese Journal of Applied Physics, Part 2: Letters* **43** (2004). 13, 56, 62

[79] **F. V. E. Hensling**, **C. Xu**, **F. Gunkel**, and **R. Dittmann**, *Scientific Reports* **7**, 39953 (2017). 13, 34, 49, 50, 57, 62, 63, 64

[80] **C. W. Schneider**, **M. Esposito**, **I. Marozau**, **K. Conder**, **M. Doebeli**, **Y. Hu**, **M. Mallepell**, **A. Wokaun**, and **T. Lippert**, *Applied Physics Letters* **97**, 95 (2010). 13, 34, 35, 43, 47

[81] **S. Amoruso**, **C. Aruta**, **R. Bruzzese**, **X. Wang**, and **U. Scotti Di Uccio**, *Applied Physics Letters* **98**, 101501 (2011). 13, 62, 63

[82] **S. Amoruso**, **C. Aruta**, **P. Aurino**, **R. Bruzzese**, **X. Wang**, **F. M. Granozio**, and **U. Scotti di Uccio**, *Applied Surface Science* **258**, 9116 (2012).

[83] **G. Herranz**, **M. Basletić**, **M. Bibes**, **C. Carrétéro**, **E. Tafra**, **E. Jacquet**, **K. Bouzehouane**, **C. Deranlot**, **A. Hamzić**, **J.-M. Broto**, **A. Barthélémy**, and **A. Fert**, *Physical Review Letters* **98**, 216803 (2007). 56, 66

[84] **H. Y. Hwang**, **A. Ohtomo**, **N. Nakagawa**, **D. A. Muller**, and **J. L. Grazul**, *Physica E: Low-Dimensional Systems and Nanostructures* **22**, 712 (2004).

[85] **A. Sambri**, **D. V. Cristensen**, **F. Trier**, **Y. Z. Chen**, **S. Amoruso**, **N. Pryds**, **R. Bruzzese**, and **X. Wang**, *Applied Physics Letters* **100**, 231605 (2012). 14, 34, 35, 43, 62

[86] **C. Cancellieri**, **N. Reyren**, **S. Gariglio**, **a. D. Caviglia**, **A. Fête**, and **J.-M. Triscone**, *EPL (Europhysics Letters)* **91**, 17004 (2010). 13, 34, 56, 62

[87] **F. Trier**, **S. Amoruso**, **D. V. Christensen**, **A. Sambri**, **Y. Z. Chen**, **X. Wang**, **E. Stamate**, **R. Bruzzese**, and **N. Pryds**, *Applied Physics Letters* **103**, 1 (2013). 14, 62

[88] **Y. Chen**, **N. Pryds**, **J. E. Kleibeuker**, **G. Koster**, **J. Sun**, **E. Stamate**, **B. Shen**, **G. Rijnders**, and **S. Linderoth**, *Nano Letters* **11**, 3774 (2011). 14, 34, 35, 47, 51, 56, 62, 64

[89] **R. Waser**, **R. Dittmann**, **M. Salinga**, and **M. Wuttig**, *Solid-State Electronics* **54**, 830 (2010). 14

[90] **K. Szot**, **W. Speier**, **G. Bihlmayer**, and **R. Waser**, *Nature materials* **5**, 312 (2006).

[91] **K. Szot**, **R. Dittmann**, **W. Speier**, and **R. Waser**, *Physica Status Solidi - Rapid Research Letters* **1**, 86 (2007). 14

[92] **E. Mikheev**, **B. D. Hoskins**, **D. B. Strukov**, and **S. Stemmer**, *Nature Communications* **5** (2014). 14, 84, 114

[93] **S. Menzel**, **M. Waters**, **A. Marchewka**, **U. Böttger**, **R. Dittmann**, and **R. Waser**, *Advanced Functional Materials* **21**, 4487 (2011). 14, 92, 116

[94] **D. H. Kwon**, **K. M. Kim**, **J. H. Jang**, **J. M. Jeon**, **M. H. Lee**, **G. H. Kim**, **X. S. Li**, **G. S. Park**, **B. Lee**, **S. Han**, **M. Kim**, and **C. S. Hwang**, *Nature Nanotechnology* **5**, 148 (2010). 14

[95] **R. Muenstermann**, **T. Menke**, **R. Dittmann**, and **R. Waser**, *Advanced Materials* **22**, 4819 (2010). 14, 16, 92, 116

[96] **M. Kubicek**, **R. Schmitt**, **F. Messerschmitt**, and **J. L. Rupp**, *ACS Nano* **9**, 10737 (2015). 14, 16

[97] **R. Waser**, **R. Bruchhaus**, and **S. Menzel**, Redox-based Resistive Switching Memories, in *Nanoelectronics and Information Technology*, edited by **R. Waser**, chapter 30, pp. 685–708, Wiley-VCH, 3 edition, 2012. 15

[98] **D. Cooper**, **C. Baeumer**, **N. Bernier**, **A. Marchewka**, **C. La Torre**, **R. E. Dunin-Borkowski**, **S. Menzel**, **R. Waser**, and **R. Dittmann**, *Advanced Materials* **29** (2017). 15, 16, 77

[99] **H. Zhang**, *Resistive switching phenomena in stacks of binary transition metal oxides grown by atomic layer deposition*, PhD thesis, RWTH Aachen University, 2019. 15

[100] **T. Heisig**, **C. Baeumer**, **U. N. Gries**, **M. P. Mueller**, **C. La Torre**, **M. Luebben**, **N. Raab**, **H. Du**, **S. Menzel**, **D. N. Mueller**, **C.-l. Jia**, **J. Mayer**, **R. Waser**, **I. Valov**, **R. A. De Souza**, and **R. Dittmann**, *Advanced Materials* **30**, 1800957 (2018). 16, 77, 92, 93, 116

[101] **M. Lippmaa**, **N. Nakagawa**, **M. Kawasaki**, **S. Ohashi**, **Y. Inaguma**, **M. Itoh**, and **H. Koinuma**, *Applied Physics Letters* **74**, 3543 (1999). 17, 69

[102] **G. Koster**, **G. Rijnders**, **D. H. A. Blank**, and **H. Rogalla**, *Physica C* **339**, 215 (2000). 17

[103] **H. N. Lee**, **S. S. A. Seo**, **W. S. Choi**, and **C. M. Rouleau**, *Scientific Reports* **6**, 19941 (2016). 20, 21, 34, 35, 43, 45

[104] **S. Wicklein**, **A. Sambri**, **S. Amoruso**, **X. Wang**, **R. Bruzzese**, **A. Koehl**, and **R. Dittmann**, *Applied Physics Letters* **101** (2012). 20, 22, 68

[105] **C. Xu**, **S. Wicklein**, **A. Sambri**, **S. Amoruso**, **M. Moors**, and **R. Dittmann**, *Journal of Physics D: Applied Physics* **47**, 034009 (2014). 74

[106] **D. J. Keeble**, **S. Wicklein**, **L. Jin**, **C. L. Jia**, **W. Egger**, and **R. Dittmann**, *Physical Review B* **87**, 195409 (2013). 20, 22, 54, 68, 100, 133

[107] **H. Schraknepper**, **C. Bäumer**, **F. Gunkel**, **R. Dittmann**, and **R. A. De Souza**, *APL Materials* **4**, 126109 (2016). 20, 21

[108] **R. Groenen**, **J. Smit**, **K. Orsel**, **A. Vailionis**, **B. Bastiaens**, **M. Huijben**, **K. Boller**, **G. Rijnders**, and **G. Koster**, *APL Materials* **3**, 070701 (2015). 20, 21

[109] **B. Dam**, **J. H. Rector**, **J. Johansson**, **S. Kars**, and **R. Griessen**, *Applied Surface Science* **96-98**, 679 (1996). 22

[110] **R. K. Singh**, **O. W. Holland**, and **J. Narayan**, *Journal of Applied Physics* **68**, 233 (1990). 22

[111] **M. Lippmaa**, **M. Kawasaki**, **A. Ohtomo**, **T. Sato**, **M. Iwatsuki**, and **H. Koinuma**, *Applied Surface Science* **130-132**, 582 (1998). 23

[112] **F. J. Himpsel**, **J. E. Ortega**, **G. J. Mankey**, and **R. F. Willis**, *Advances in Physics* **47**, 511 (1998). 23

[113] **S. Hasegawa**, Reflection High-Energy Electron Diffraction, in *Characterization of Materials*, edited by **E. N. Kaufamnn**, pp. 1925–1938, John Wiley & Sons, Inc., 2012. 23

[114] **S. Swann**, *Physics in Technology* **19**, 67 (1988). 25

[115] **G. Bräuer**, **B. Szyszka**, **M. Vergöhl**, and **R. Bandorf**, *Vacuum* **84**, 1354 (2010). 25

[116] **P. D. Davidse**, *Vacuum* **17**, 139 (1967). 26

[117] **K.S. Sree Harsha**, *Principles of Vapor Deposition of Thin Films*, Elsevier, 2006. 26

[118] **B. Voigtländer**, *Scanning probe microscopy*, Springer, 2015. 27

[119] **S. Hofmann**, *Auger-and X-ray photoelectron spectroscopy in materials science: a user-oriented guide*, volume 49, Springer Science & Business Media, 2012. 27

[120] **A. Guinier**, *X-ray diffraction in crystals, imperfect crystals, and amorphous bodies*, Courier Corporation, 1994. 28

[121] **K. von Klitzing**, *Reviews of Modern Physics* **58**, 519 (1986). 31

[122] **E. H. Hall**, *American Journal of Mathematics* **2**, 287 (1879). 31

[123] **L. J. van der Pauw**, *Philips Research Reports* **13**, 1 (1958). 31

[124] **H. Rinne**, *The Weibull Distribution*, Chapman and Hall/CRC, 2008. 32

[125] **R. Dittmann**, **R. Muenstermann**, **I. Krug**, **D. Park**, **T. Menke**, **J. Mayer**, **A. Besmehn**, **F. Kronast**, **C. M. Schneider**, and **R. Waser**, *Proceedings of the IEEE* **100**, 1979 (2012). 33

[126] **F. V. E. Hensling**, **D. J. Keeble**, **J. Zhu**, **S. Brose**, **C. Xu**, **F. Gunkel**, **S. Danylyuk**, **S. S. Nonnenmann**, **W. Egger**, and **R. Dittmann**, *Scientific Reports* **8**, 8846 (2018). 34

[127] **M. L. Scullin**, **J. Ravichandran**, **C. Yu**, **M. Huijben**, **J. Seidel**, **A. Majumdar**, and **R. Ramesh**, *Acta Materialia* **58**, 457 (2010). 34

[128] **F. Chen**, **H. Lu**, **Z. Chen**, **T. Zhao**, **G. Yang**, and **X. D. Zhu**, *Journal of the Optical Society of America B* **19**, 1218 (2002). 34, 47

[129] **F. Hensling**, **C. Xu**, **F. Gunkel**, and **R. Dittmann**, *Scientific Reports* **7** (2017). 34

[130] **E. Breckenfeld**, **N. Bronn**, **J. Karthik**, **A. R. Damodaran**, **S. Lee**, **N. Mason**, and **L. W. Martin**, *Physical Review Letters* **110**, 1 (2013). 34, 44

[131] **G. Herranz**, **M. Basletić**, **M. Bibes**, **C. Carrétéro**, **E. Tafra**, **E. Jacquet**, **K. Bouzehouane**, **C. Deranlot**, **A. Hamzić**, **J.-M. Broto**, **A. Barthélémy**, and **A. Fert**, *Physical Review Letters* **98**, 216803 (2007). 35, 44

[132] **M. L. Scullin**, **J. Ravichandran**, **C. Yu**, **M. Huijben**, **J. Seidel**, **A. Majumdar**, and **R. Ramesh**, *Acta Materialia* **58**, 457 (2010). 35, 43

[133] **A. Ohtomo** and **H. Y. Hwang**, *Nature* **427**, 423 (2004).

[134] **A. Brinkman**, **M. Huijben**, **M. van Zalk**, **J. Huijben**, **U. Zeitler**, **J. C. Maan**, **W. G. van der Wiel**, **G. Rijnders**, **D. H. a. Blank**, and **H. Hilgenkamp**, *Nature materials* **6**, 493 (2007). 34

[135] **F. Chen**, **T. Zhao**, **Y. Y. Fei**, **H. Lu**, **Z. Chen**, **G. Yang**, and **X. D. Zhu**, *Applied Physics Letters* **80**, 2889 (2002). 35, 43

[136] **T. Bieger**, **J. Maier**, and **R. Waser**, *Solid State Ionics* **56**, 578 (1992). 36, 44

[137] **U. Balachandran** and **N. Eror**, *Journal of Solid State Chemistry* **39**, 351 (1981). 39

[138] **P. Scheiderer**, **F. Pfaff**, **J. Gabel**, **M. Kamp**, **M. Sing**, and **R. Claessen**, *Physical Review B - Condensed Matter and Materials Physics* **92**, 1 (2015). 40, 42

[139] **R. Waser**, *Solid State Ionics* **56**, 578 (1992). 41, 42

[140] **W. S. Choi**, **C. M. Rouleau**, **S. S. A. Seo**, **Z. Luo**, **H. Zhou**, **T. T. Fister**, **J. A. Eastman**, **P. H. Fuoss**, **D. D. Fong**, **J. Z. Tischler**, **G. Eres**, **M. F. Chisholm**, and **H. N. Lee**, *Advanced Materials* **24**, 6423 (2012). 45

[141] **A. Kalabukhov**, **Y. A. Boikov**, **I. T. Serenkov**, **V. I. Sakharov**, **J. Börjesson**, **N. Ljustina**, **E. Olsson**, **D. Winkler**, and **T. Claeson**, *EPL (Europhysics Letters)* **93**, 37001 (2011). 45

[142] **R. Merkle**, **R. A. D. Souza**, and **J. Maier**, *Angewandte Chemie (International ed. in English)* **4**, 2126 (2001). 47, 55, 128, 129

[143] **R. Merkle** and **J. Maier**, *Physical Chemistry Chemical Physics* **4**, 4140 (2002). 64, 115

[144] **M. Leonhardt**, **R. A. De Souza**, **J. Claus**, and **J. Maier**, *Journal of the Electrochemical Society* **149**, J19 (2002). 55, 129

[145] **G. Walch**, **B. Rotter**, **G. C. Brunauer**, **E. Esmaeili**, **A. K. Opitz**, **M. Kubicek**, **J. Summhammer**, **K. Ponweiser**, and **J. Fleig**, *Journal of Materials Chemistry A* **5**, 1637 (2017). 47

[146] **A. Kramida**, **Y. Ralchenko**, **J. Reader**, and **N. A. Team**, NIST Atomic Spectra Database, 2018. 48

[147] **G. Schriever**, **S. Mager**, **A. Naweed**, **A. Engel**, **K. Bergmann**, and **R. Lebert**, *Applied optics* **37**, 1243 (1998). 48

[148] **R. M. Gilgenbach**, **C. H. Ching**, **J. S. Lash**, and **R. A. Lindley**, *Physics of Plasmas* **1**, 1619 (1994). 48

[149] **E. R. Dobrovinskaya**, **L. A. Lytvynov**, and **V. Pishchik**, Properties of Sapphire, in *Sapphire: Material, Manufacturing, Applications*, chapter 2, pp. 55–176, Springer Science+Business Media, New York, 2009. 48

[150] **Y. Z. Chen**, **M. Döbeli**, **E. Pomjakushina**, **Y. L. Gan**, **N. Pryds**, and **T. Lippert**, *Physical Review Materials* **1**, 052002 (2017). 51

[151] **C. Maragliano**, **S. Lilliu**, **M. S. Dahlem**, **M. Chiesa**, **T. Souier**, and **M. Stefancich**, *Scientific Reports* **4**, 4203 (2014). 51

[152] **C. Hugenschmidt**, **C. Piochacz**, **M. Reiner**, and **K. Schreckenbach**, *New Journal of Physics* **14**, 055027 (2012). 52

[153] **W. Egger**, Pulsed low-energy positron beams in materials sciences, in *Physics with Many Positrons*, edited by **A. Dupasquier**, **A. P. Mills**, and **R. S. Brusa**, pp. 419–449, IOS Press, Amsterdam, 2010. 52

[154] **D. J. Keeble**, **R. A. MacKie**, **W. Egger**, **B. Löwe**, **P. Pikart**, **C. Hugenschmidt**, and **T. J. Jackson**, *Physical Review B - Condensed Matter and Materials Physics* **81**, 1 (2010). 53

[155] **D. J. Keeble**, **S. Wicklein**, **R. Dittmann**, **L. Ravelli**, **R. A. MacKie**, and **W. Egger**, *Physical Review Letters* **105**, 3 (2010). 53

[156] **R. Gomez-San Roman**, **R. Pérez Casero**, **C. Maréchal**, **J. Enard**, and **J. Perrière**, *Journal of Applied Physics* **80** (1996). 55

[157] **R. Perez-Casero**, **J. Perrière**, **A. Gutierrez-Llorente**, **D. Defourneau**, **E. Millon**, **W. Seiler**, and **L. Soriano**, *Physical Review B - Condensed Matter and Materials Physics* **75**, 1 (2007). 55

[158] **W. Meevasana**, **P. D. C. King**, **R. H. He**, **S.-K. Mo**, **M. Hashimoto**, **A. Tamai**, **P. Songsiriritthigul**, **F. Baumberger**, and **Z.-X. Shen**, *Nature Materials* **10**, 114 (2011). 55

[159] **B. Zheng** and **N. Binggeli**, *Physical Review B* **82**, 245311 (2010). 56

[160] **G. Rijnders**, **S. Currás**, **M. Huijben**, **D. H. Blank**, and **H. Rogalla**, *Applied Physics Letters* **84**, 1150 (2004). 56

[161] **J. J. M. Tascón** and **L. L. G. Tejuca**, *Journal of the Chemical Society, Faraday Transactions* **1**, 591 (1981). 56

[162] **K. Huang**, **X. Chu**, **L. Yuan**, **W. Feng**, **X. Wu**, **X. Wang**, and **S. Feng**, *Chemical Communications* **50**, 9200 (2014).

[163] **D. Maiti**, **Y. A. Daza**, **M. M. Yung**, **J. N. Kuhn**, and **V. R. Bhethanabotla**, *Journal of Materials Chemistry A* **4**, 5137 (2016). 56

[164] **V. E. Alexandrov**, **E. a. Kotomin**, **J. Maier**, and **R. a. Evarestov**, *The European Physical Journal B* **72**, 53 (2009). 56, 64, 129

[165] **T. L. Barr** and **S. Seal**, *Journal of Vacuum Science & Technology A: Vacuum, Surfaces, and Films* **13**, 1239 (1995). 58, 61

[166] **P. Swift**, *Surface and Interface Analysis* **4**, 47 (1982). 58, 61

[167] **A. V. Shchukarev** and **D. V. Korolkov**, *Central European Journal of Chemistry* **2**, 347 (2004). 59, 104

[168] **K. Lam**, **Y. Gao**, **J. Wang**, and **F. Ciucci**, *Electrochimica Acta* **244**, 139 (2017).

[169] **E. J. Crumlin**, **E. Mutoro**, **Z. Liu**, **M. E. Grass**, **M. D. Biegalski**, **Y.-L. Lee**, **D. Morgan**, **H. M. Christen**, **H. Bluhm**, and **Y. Shao-Horn**, *Energy & Environmental Science* **5**, 6081 (2012). 59, 104

[170] **K. Szot**, **W. Speier**, **U. Breuer**, **R. Meyer**, **J. Szade**, and **R. Waser**, *Surface Science* **460**, 112 (2000). 59, 104

[171] **H. Piao** and **N. S. McIntyre**, *Surface and Interface Analysis* **33**, 591 (2002). 61

[172] **D. J. Miller**, **M. C. Biesinger**, and **N. S. McIntyre**, *Surface and Interface Analysis* **33**, 299 (2002). 61

[173] **R. Ropp**, The Alkaline Earths as Metals, in *Encyclopedia of the Alkaline Earth Compounds*, chapter 1, pp. 1–23, Elsevier, Amsterdam, 1 edition, 2013. 61

[174] **C. Baeumer**, **C. Schmitz**, **A. H. H. Ramadan**, **H. Du**, **K. Skaja**, **V. Feyer**, **P. Müller**, **B. Arndt**, **C.-L. Jia**, **J. Mayer**, **R. A. De Souza**, **C. M. Schneider**, **R. Waser**, and **R. Dittmann**, *Nature Communications* **6**, 8610 (2015). 64, 78, 79, 80, 84, 93, 99, 100, 132, 134, 135

[175] **F. Hensling**, **T. Heisig**, **N. Raab**, **C. Baeumer**, and **R. Dittmann**, *Solid State Ionics* **325**, 247 (2018). 64, 65, 74, 78, 80

[176] **Y. Hotta**, **T. Susaki**, and **H. Y. Hwang**, *Physical Review Letters* **99**, 3 (2007). 66

[177] **C. He**, **T. D. Sanders**, **M. T. Gray**, **F. J. Wong**, **V. V. Mehta**, and **Y. Suzuki**, *Physical Review B - Condensed Matter and Materials Physics* **86**, 1 (2012).

[178] **I. Vrejoiu**, **C. Himcinschi**, **L. Jin**, **C. L. Jia**, **N. Raab**, **J. Engelmayer**, **R. Waser**, **R. Dittmann**, and **P. H. M. Van Loosdrecht**, *APL Materials* **4**, 046103 (2016). 66

[179] **A. Shkabko**, **C. Xu**, **P. Meuffels**, **F. Gunkel**, **R. Dittmann**, **A. Weidenkaff**, and **R. Waser**, *APL Materials* **1**, 0 (2013). 66

[180] **A. F. Santander-Syro**, **O. Copie**, **T. Kondo**, **F. Fortuna**, **S. Pailhes**, **R. Weht**, **X. G. Qiu**, **F. Bertran**, **A. Nicolaou**, **A. Taleb-Ibrahimi**, **P. Le Fvre**, **G. Herranz**, **M. Bibes**, **N. Reyren**, **Y. Apertet**, **P. Lecoeur**, **A. Barthelemy**, and **M. J. Rozenberg**, *Nature* **469**, 189 (2011). 66

[181] **W. C. Fan** and **A. Ignatiev**, *Journal of Vacuum Science & Technology A: Vacuum, Surfaces, and Films* **3479** (1990). 68

[182] **A. Ichimiya** and **P. Cohen**, Electron scattering by atoms, in *Reflection High-Energy Electron Diffraction*, pp. 113–129, Cambridge: Cambridge University Press, 2004. 71, 94

[183] **P. Brown**, **A. Fox**, **E. Maslen**, **M. O'Keefe**, and **B. Willis**, Intensity of diffracted intensities, in *International Tables for Crystallography Volume C*, edited by **E. Prince**, pp. 554–595, International Union of Crystallography, 2006. 71, 94

[184] **C. Baeumer**, **C. Xu**, **F. Gunkel**, **N. Raab**, **R. A. Heinen**, **A. Koehl**, and **R. Dittmann**, *Scientific Reports* **5**, 11829 (2015). 73

[185] **C. Xu**, **M. Moors**, and **R. Dittmann**, *Applied Surface Science* **359**, 68 (2015). 74, 75

[186] **H. Scheel**, *Zeitschrift für Kristallographie - Crystalline Materials* **143**, 417 (1976). 75, 76, 130

[187] **C. Baeumer**, **N. Raab**, **T. Menke**, **C. Schmitz**, **R. Rosezin**, **P. Müller**, **M. Andrä**, **V. Feyer**, **R. Bruchhaus**, **F. Gunkel**, **C. M. Schneider**, **R. Waser**, and **R. Dittmann**, *Nanoscale* **8**, 13967 (2016). 77, 93, 134

[188] **C. Baeumer**, **C. Schmitz**, **A. Marchewka**, **D. N. Mueller**, **R. Valenta**, **J. Hackl**, **N. Raab**, **S. P. Rogers**, **M. I. Khan**, **S. Nemsak**, **M. Shim**, **S. Menzel**, **C. M. Schneider**, **R. Waser**, and **R. Dittmann**, *Nature Communications* **7** (2016). 77, 100, 132, 134, 135

[189] **N. Raab**, *Fabrication of SrTiO3 thin films with tailored defect structure for future non-volatile memories*, PhD thesis, RWTH Aachen, 2017. 78, 107, 122

[190] **C. Baeumer**, *Spectroscopic characterization of local valence change processes in resistively switching complex oxides*, PhD thesis, RWTH Aachen, 2016. 78

[191] **T. Fujii**, **M. Kawasaki**, **A. Sawa**, **H. Akoh**, **Y. Kawazoe**, and **Y. Tokura**, *Applied Physics Letters* **86**, 1 (2005). 84

[192] **M. Naito**, **H. Yamamoto**, and **H. Sato**, *Physica C: Superconductivity and its Applications* **305**, 233 (1998). 87

[193] **G. S. Bales** and **A. Zangwill**, *Physical Review B* **41**, 5500 (1990). 87

[194] **R. S. Williams**, *Faraday Discussions* **213**, 579 (2019). 92, 132

[195] **F. Oba**, **M. Choi**, **A. Togo**, **A. Seko**, and **I. Tanaka**, *Journal of Physics Condensed Matter* **22** (2010). 92

[196] **M. M. Rutkowski**, **K. McNicholas**, **Z. Q. Zeng**, **F. Tuomisto**, and **L. J. Brillson**, *Journal of Physics D: Applied Physics* **47**, 255303 (2014). 92

[197] **Z. Zhang**, **W. Sigle**, **R. A. De Souza**, **W. Kurtz**, **J. Maier**, and **M. Rühle**, *Acta Materialia* **53**, 5007 (2005). 92, 93, 133

[198] **R. A. Souza**, **J. Fleig**, **J. Maier**, **O. Kienzle**, **Z. Zhang**, **W. Sigle**, and **M. Rühle**, *Journal of the American Ceramic Society* **86**, 922 (2003). 92

[199] **D. Marrocchelli**, **L. Sun**, and **B. Yildiz**, *Journal of the American Chemical Society* **137**, 4735 (2015). 92, 93, 133

[200] **F. W. Sears**, *American Journal of Physics* **351** (1943). 92

[201] **C. Baeumer**, **R. Valenta**, **C. Schmitz**, **A. Locatelli**, **T. O. Mentes**, **S. P. Rogers**, **A. Sala**, **N. Raab**, **S. Nemsak**, **M. Shim**, **C. M. Schneider**, **S. Menzel**, **R. Waser**, and **R. Dittmann**, *ACS Nano* **11**, 6921 (2017). 93, 100, 120, 132, 134, 135

[202] **F. Z. Aoumeur-Benkabou** and **B. Belgoumène**, *Calphad: Computer Coupling of Phase Diagrams and Thermochemistry* **28**, 65 (2004). 94

[203] **O. Madelung**, **U. Rössler**, and **M. Schulz**, Strontium oxide (SrO) crystal structure, lattice parameters, thermal expansion, in *II-VI and I-VII Compounds; Semimagnetic Compounds*, pp. 1–3, Springer-Verlag, Berlin/Heidelberg, 41b edition, 1999. 94, 100, 117

[204] **W. E. Danforth** and **D. L. Goldwater**, *Journal of Applied Physics* **20**, 163 (1949). 103

[205] **C.-H. Chen**, **E. L. Hu**, **W. V. Schoenfeld**, and **P. M. Petroff**, *Journal of Vacuum Science & Technology B: Microelectronics and Nanometer Structures* **16**, 3354 (1998). 114

[206] **R. Koch**, *Surface and Coatings Technology* **204**, 1973 (2010).

[207] **E. Krikorian** and **R. J. Sneed**, *Journal of Applied Physics* **37**, 3665 (1966).

[208] **E. Lugscheider**, **C. Barimani**, **C. Wolff**, **S. Guerreiro**, and **G. Doepper**, *Surface and Coatings Technology* **86-87**, 177 (1996).

[209] **H. Fornander**, **J. Birch**, **P. Sandström**, and **J.-E. Sundgren**, *Thin Solid Films* **349**, 4 (1999).

[210] **A. E. Ennos**, *British Journal of Applied Physics* **8**, 113 (1957). 114

[211] **E. Auer**, **A. Freund**, **J. Pietsch**, and **T. Tacke**, *Applied Catalysis A: General* **173**, 259 (1998). 115

[212] **F. Rodríguez-reinoso**, *Carbon* **36**, 159 (1998).

[213] **K. Pirkanniemi** and **M. Sillanpää**, *Chemosphere* **48**, 1047 (2002).

[214] **A. L. Dicks**, *Journal of Power Sources* **156**, 128 (2006). 115

[215] **A. Pozio**, **M. De Francesco**, **A. Cemmi**, **F. Cardellini**, and **L. Giorgi**, *Journal of Power Sources* **105**, 13 (2002). 115

[216] **J. Maier**, **G. Schwitzgebel**, and **H. J. Hagemann**, *Journal of Solid State Chemistry* **58**, 1 (1985). 115

[217] **J. S. Yoo** and **S. M. Park**, *Analytical Chemistry* **77**, 3694 (2005). 115

[218] **D. Xu**, CARBON-CONTAINING INTERFACIAL LAYER FOR PHASE-CHANGE MEMORY, 2003. 116

[219] **F. Rao**, **Z. Song**, **Y. Gong**, **L. Wu**, **B. Liu**, **S. Feng**, and **B. Chen**, *Applied Physics Letters* **92**, 4 (2008). 116

[220] **A. A. Balandin**, *Nature Materials* **10**, 569 (2011). 116, 118

[221] **H. Szelagowski**, **I. Arvanitidis**, and **S. Seetharaman**, *Journal of Applied Physics* **85**, 193 (1999). 116

[222] **S. Ni**, **X. Yang**, and **T. Li**, *Materials Letters* **65**, 766 (2011). 117

[223] **P. Kováč** and **I. Hušek**, *Physica C: Superconductivity and its Applications* **383**, 55 (2002). 117, 132, 134

[224] **G. K. White**, Pb - Ta, in *Thermal Conductivity of Pure Metals and Alloys*, edited by **O. Madelung** and **G. K. White**, pp. 38–51, Springer-Verlag, Berlin/Heidelberg, 2005. 118

[225] **G. K. White**, Ac - Fe, in *Thermal Conductivity of Pure Metals and Alloys*, edited by **O. Madelung** and **G. K. White**, pp. 10–23, Springer-Verlag, Berlin/Heidelberg, 2005. 118

[226] **S. Shimada**, **T. Koyama**, **K. Kodaira**, and **T. Mastushita**, *Journal of Materials Science* **18**, 1291 (1983). 119

[227] **I. Valov**, *In Preperation* (2019). 119

[228] **P. Villars**, TaC thermal conductivity, PAULING FILE, in *Inorganic Solid Phases*, edited by **P. Villars** and **F. Hulliger**, p. 048276, SpringerMaterials (online database), Heidelberg, 2016. 119

[229] **K. A. Boahen**, *Communicating Neuronal Ensembles between Neuromorphic Chips*, pp. 229–259, Springer US, Boston, MA, 1998. 120, 134

[230] **K. Boahen**, *IEEE Transactions on Circuits and Systems II: Analog and Digital Signal Processing* **47**, 416 (2000).

[231] **G. S. Snider**, *Nanotechnology* **18** (2007).

[232] **D. Querlioz**, **O. Bichler**, **P. Dollfus**, and **C. Gamrat**, *IEEE Transactions on Nanotechnology* **12**, 288 (2013).

[233] **R. M. Shelby**, **G. W. Burr**, **I. Boybat**, and **C. Di Nolfo**, *IEEE International Reliability Physics Symposium Proceedings* **2015-May**, 6A11 (2015). 120, 134

[234] **P. Genoni**, **F. Genuzio**, **T. O. Mentes**, **B. Santos**, **A. Sala**, **C. Lenardi**, and **A. Locatelli**, *ACS Applied Materials and Interfaces* **10**, 27178 (2018). 120

[235] **Y. N. Loginov**, **A. V. Yermakov**, **L. G. Grohovskaya**, and **G. I. Studenok**, *Platinum Metals Review* **51**, 178 (2007). 124

[236] **R. A. De Souza**, **J. Fleig**, **R. Merkle**, and **J. Maier**, *Zeitschrift für Metallkunde* **94**, 218 (2003). 133

[237] **H. Wang**, **Y. Xu**, **M. Goto**, **Y. Tanaka**, **M. Yamazaki**, **A. Kasahara**, and **M. Tosa**, *Materials Transactions* **47**, 1894 (2006). 134

[238] **M. S. Seehra** and **H. Wijn**, 6.1.5 Oxides of 4d and 5d transition elements, in *Various Other Oxides*, pp. 71–84, Springer-Verlag, Berlin/Heidelberg, 2005. 134

[239] **J. J. Yang**, **D. B. Strukov**, and **D. R. Stewart**, *Nature Nanotechnology* **8**, 13 (2013). 134

Acknowledgments

This doctoral thesis was only possible due to the help of countless people on a professional and non-professional level. Despite the countlessness I will in the following try to thank most of them.

First and foremost I want to thank my supervisor Prof. Regina Dittmann. By agreeing to supervise me, she did make this thesis possible in the first place. Further, she provided me with the necessary insights into the scientific methods and community. She always found the right balance of supervising me and letting me take my own path. Not only did I highly benefit from her supervision on a professional scientific level, but also on a private level, as I always enjoyed our meetings and discussions, and I doubt there was ever one not accompanied by laughter.

I would like to thank Prof. Dr. Joachim Mayer, who agreed to supervise me officially. I always enjoyed my work together with him in my role as the doctoral spokesperson of the SFB917 and very much value his scientific input and advice, and knowledge of the bureaucracy of science.

I started my carrier at the PGI-7 writing my project thesis, for which I have to thank Nicolas Raab, and proceeded with my master thesis, supervised by Chencheng Xu, before becoming a doctoral student.

During my time as a doctoral student Christoph Baeumer and Felix Gunkel have become mentors for me. They helped me refining my scientific writing skills and were always open for lengthy discussions.

In my time at the PGI-7 I have had many office colleagues. Not only has our office always been a fruitful work environment, but also a place of fun. I will following list my office colleagues chronologically: Nicolas Raab, Chencheng Xu, Philipp

Müller, Thorsten Meiners, Benedikt Arndt (kind of), Michael Andrä, Richard Valenta, Thomas Heisig, Jacqueline Börgers, Marc-André Rose and Venkata Raveendra Nallagatla.

I would like to thank Hongchu Du for his patience while finding anti phase boundaries and more than one long night in the ERC. I would like to thank Prof. Roger de Souza, Joe Kler and Michael Müller of the IPC for the productive discussions.

Thomas Heisig has without a doubt been the colleague I cooperated with the most. He was always ready to lend a helping hand, especially doing clean room work on my behalf. I was lucky enough to highly benefit from my predecessor Nico Raab with whom I modified the vacuum system on a nearly daily basis and with whom I spent some long nights in the office. I would once again like to thank Christoph Baeumer, who supplied me with XPS measurements. I would further like to thank Jan Rieck, my master student, who supplied me with the variability data and experiments, which can be quite lengthy and repetitive. I would like to thank Alexander Gutsche, who, at the end of my doctoral studies, shared and took over most of my teaching related responsibilities.

Of course I am also grateful to the technical staff. Georg Pickartz, who kept the laser up and running; Stephan Masberg, who taught me, beside other things, how to repair leak valves and was always willing to assist me with constructional concerns; Jochen Friedrich, who more than once repaired the finer parts of my holder designs; Marcel Gerst, who assisted me with numerous electronical issues; and René Borowski, who processed countless of my samples.

I am thankful to Paul Meuffels with whom I discussed science on a philosophical level. Additionally he was the best company to have, when I still took my smoke breaks.

With that I would like turn to the more personal acknowledgments. Of course I am grateful beyond description to my wife Alina, who is also the mother of the greatest joy in my life, Tristan. I would like to thank her parents, Willi and Tamara, as they often took care of our child, when I was not able to because of being busy with this thesis. I would also like to thank my father Volker, who has always been willing to sacrifice nearly everything for my benefit.

With many of the above mentioned or unmentioned colleagues I have spent significant parts of my leisure time and some of them have grown to be close friends. Once upon a time Christoph Baeumer, Nicolas Raab, Benedikt Arndt and me started the tradition of the 'Feierabendbier'. A tradition that survived until now and has seen many regular participants come and go.

Nicolas Raab was generally always ready to accompany me for a beer in his second home the 'zuhause'. Not only did he teach me the art of foosball, but he also become a good friend, whose company I enjoy each time we manage to reunite.

During the time I lived in Aachen alone the living room of Christoph Baeumer and his wife was figuratively mine, before ultimately becoming literally mine. They (and their dogs) hold a special place in my heart and I will never forget that Christoph was the first person to know that I will become a father (naturally besides my wife).

The time I lived alone in Aachen is tantamount with a time of spending my weekends in Bonn. Not only did Michael Andrä willingly commute there with me, but did also spend a lot of time with me and my wife in this beautiful city.

Benedikt Arndt has been a welcome, enjoyable and frequent guest to our office during his time at the PGI-7. While his talent surely includes to distract me from work, together we most enjoyed to gossip about people, who I would like to characterize by the following Nietzsche quote: '*Mystical explanations are thought to be deep; the truth is, they are not even shallow.*'[1]

Thomas Heisig and Felix Cüppers both moved to become my neighbors, which I am sure was their main motivation. A truly enjoyable side effect of this is that I always had friends living nearby, nearly always willing to spend their time with me. Moritz Weber may well be the only person at work I am able to talk to about music. He must thus have an extraordinary good taste.

The most lucky happenstance in the recent years may well be that Felix Gunkel and me do not only share first names, but did nearly simultaneously experience the joys

---

[1] Frierich Nietzsche, *The Gay Science*, Section 126

of fatherhood. As a result he was the first choice for sharing the escapades of my son.

Jacqueline Börgers joined my office relatively late, yet she quickly became a close friend. Not only do we share a passion for thin film growth, but do also get along so well that I ended up being the best man of her groom.

Last I want to thank René Ebeling. Over the time spent at the PGI-7 he has become a very close friend with whom I did not only celebrate the birth of my son, but who also has become an uncle to him. It is not often in life one meets a person with whom one is in sync on so many levels. I appreciate his role in my life on so many levels, that a detailed description would go beyond the scope of these acknowledgments.

Band / Volume 46
Growth and characterization of crystalline rare-earth based thin oxide fims for the application as gate dielectric in nanotechnology
A. B. Schäfer (2015), xiii, 157 pp
ISBN: 978-3-95806-111-8

Band / Volume 47
TEM/STEM Investigations of Phase Change Materials for Non-volatile Memory Applications
M. Bornhöfft (2017), viii, 135 pp
ISBN: 978-3-95806-221-4

Band / Volume 48
Investigation of ternary nitride semiconductor alloys by scanning tunneling microscopy
V. Portz (2017), 140 pp
ISBN: 978-3-95806-232-0

Band / Volume 49
Redox processes and ionic transport in resistive switching binary metal oxides
K. Skaja (2017), VII, 203 pp
ISBN: 978-3-95806-236-8

Band / Volume 50
Investigation of switching mechanism in Ta_2O_5 -based ReRAM devices
K. Wonjoo (2017), iii, 138 pp
ISBN: 978-3-95806-261-0

Band / Volume 51
Development of ReRAM-based Devices for Logic- and Computation-in-Memory Applications
T. Breuer (2017), x, 179 pp
ISBN: 978-3-95806-270-2

Band / Volume 52
Resistive switching memory devices from atomic layer deposited binary and ternary oxide thin films
N. Aslam (2017), X, 172 pp
ISBN: 978-3-95806-274-0

Band / Volume 53
Operando X-ray photoemission electron microscopy (XPEEM) investigations of resistive switching metal-insulator-metal devices
C. J. Schmitz (2017), IX, 153 pp
ISBN: 978-3-95806-283-2

Band / Volume 54
Optimization of powder and ceramic processing, electrical characterization and defect chemistry in the system $Yb_xCa_{1-x}MnO_3$
M. Rahmani (2018), XIV, 164 pp
ISBN: 978-3-95806-323-5

Band / Volume 55
Organic-Metal Hybrid Interfaces at the Mesoscopic Scale
G. Zamborlini (2018), xi, 133 pp
ISBN: 978-3-95806-328-0

Band / Volume 56
Configurable frequency synthesizer for large scale physics experiments
N. Parkalian (2019), xxi, 114 pp
ISBN: 978-3-95806-393-8

Band / Volume 57
Resistive switching phenomena in stacks of binary transition metal oxides grown by atomic layer deposition
H. Zhang (2019), ix, 196 pp
ISBN: 978-3-95806-399-0

Band / Volume 58
Element-Selective Investigation of Femtosecond Spin Dynamics in Ni_xPd_{1-x} Magnetic Alloys using Extreme Ultraviolet Radiation
S. Gang (2019), 93, xx pp
ISBN: 978-3-95806-411-9

Band / Volume 59
Defect engineering in oxide thin films
F. V. E. Hensling (2019), 10, 164 pp
ISBN: 978-3-95806-424-9

Weitere ***Schriften des Verlags im Forschungszentrum Jülich*** unter
http://wwwzb1.fz-juelich.de/verlagextern1/index.asp

Information
Band / Volume 59
ISBN 978-3-95806-424-9

JÜLICH
Forschungszentrum

Mitglied der Helmholtz-Gemeinschaft